



Multi-dimensional Thermal Response & Permeability Characterization for Porous Ablative Materials

PhD Thesis

Viola Renato

Future Air-Space Transportation Technology Laboratory (FASTTlab)

Department of Mechanical and Aerospace Engineering

University of Strathclyde, Glasgow

September 3, 2018

This thesis is the result of the author's original research. It has been composed by the author and has not been previously submitted for examination which has led to the award of a degree.

The copyright of this thesis belongs to the author under the terms of the United Kingdom Copyright Acts as qualified by University of Strathclyde Regulation 3.50. Due acknowledgement must always be made of the use of any material contained in, or derived from, this thesis.

Signed: Viola Renato

Date: 03/09/2018

To my family and those who have become my family in these three years, I love you and I couldn't have done it without you.

*Considerate la vostra semenza:
fatti non foste a viver come bruti,
ma per seguir virtute e canoscenza.*

*Consider well the seed that gave you birth:
you were not made to live as brutes,
but to follow virtue and knowledge.*

Dante Alighieri's Inferno, canto XXVI

Abstract

In space missions, the atmospheric entries present a critical challenge for the design of spacecraft due to the extreme external environment that they must endure. Thermal protection systems (TPSs) are required to prevent any damage to the spacecraft, its internal components or passengers. A very common and highly reliable TPS type is based on the use of ablative materials.

The improvement of the ablator simulation procedure in its entirety, from the first phases of the design process to the exceptionally accurate modelling of the material behaviour in the final stages, is the focus of the study herein presented. In order to achieve this goal, two activities were completed: the creation of a new simulation tool and the precise characterization of porous material permeability. The simulation tool consists of a novel and low computationally demanding coupled methodology able to simulate the three-dimensional behaviour of ablative TPSs. This tool is composed by the Ablative Response Code (ARC), which was specifically designed for this task, and reduced order aero-thermodynamic models. The property characterization was performed using the DSMC (Direct Simulation Monte Carlo) method. This activity evaluated the changes in permeability, commonly considered constant, caused by the variations in temperature and pressure occurring during a (re-)entry.

The combination of the activities generated for this dissertation can be used for both the design of future mission TPSs and the development of next generation ablative materials. Simulation results produced for several test cases with different planets' atmospheres and examples of possible applications are presented as confirmation of the developed methods relevance for ablative design and development.

Contents

| | |
|---|-------|
| Abstract | iii |
| List of Figures | vii |
| List of Tables | xvi |
| List of Symbols | xviii |
| List of Acronyms | xxii |
| 1 Introduction | 1 |
| 1.1 Historical Overview of ablative TPS Development | 4 |
| 1.1.1 NASA missions | 4 |
| 1.1.2 European missions | 9 |
| 1.1.3 Future needs | 11 |
| 1.2 Literature review | 13 |
| 1.2.1 Thermo-ablative material response programs | 13 |
| 1.2.2 Coupled approaches | 19 |
| 1.3 Contributions to the field | 19 |
| 2 One-dimensional ablative response code | 22 |
| 2.1 Governing Equations | 22 |
| 2.1.1 Degradation | 24 |
| 2.1.2 The in-depth energy equation | 25 |
| 2.1.3 Boundary conditions | 26 |

Contents

| | | |
|----------|--|-----------|
| 2.1.4 | Pyrolysis gas and char production | 27 |
| 2.1.5 | Blowing correction | 29 |
| 2.2 | Computational procedure | 29 |
| 2.3 | Material model | 33 |
| 2.4 | Code verification | 35 |
| 2.4.1 | Simple heat transfer case | 35 |
| 2.4.2 | TACOT | 36 |
| 2.4.3 | PICA | 46 |
| 2.5 | Discussion | 51 |
| 3 | Aero-thermodynamic Models and Code Coupling | 53 |
| 3.1 | Aero-thermodynamic Model: HyFlow | 53 |
| 3.1.1 | Heat Flux | 55 |
| 3.1.2 | Heat Transfer Coefficient | 56 |
| 3.1.3 | Selection of the stagnation area | 56 |
| 3.2 | Aero-thermodynamic Model: FOSTRAD | 58 |
| 3.2.1 | Heat Flux | 59 |
| 3.3 | Coupling | 60 |
| 3.3.1 | Coupled approach shared data between codes | 62 |
| 3.4 | Discussion | 63 |
| 4 | Three-dimensional test cases | 65 |
| 4.1 | Earth re-entry | 65 |
| 4.1.1 | Stardust re-entry with HyFlow | 65 |
| 4.1.2 | Stardust re-entry with FOSTRAD | 75 |
| 4.1.3 | The Atmospheric Re-entry Demonstrator | 82 |
| 4.2 | Planetary entry | 89 |
| 4.3 | The Pathfinder Martian Entry | 90 |
| 4.3.1 | Non axi-symmetrical case | 95 |
| 4.4 | Discussion | 98 |

Contents

| | |
|---|------------|
| 5 Permeability | 100 |
| 5.1 Methodology | 101 |
| 5.1.1 Novelty in the methodology used | 107 |
| 5.2 Results: permeability dependence on external conditions | 108 |
| 5.2.1 Pressure dependency | 108 |
| 5.2.2 Temperature dependency | 115 |
| 5.2.3 Simulation time | 118 |
| 5.3 Discussion | 120 |
| 5.4 Acknowledgements | 121 |
| 6 Conclusions | 122 |
| 6.1 Future work | 126 |
| Bibliography | 128 |

List of Figures

| | | |
|-----|--|----|
| 1.1 | TPS design and flight test environments as presented by Curry [13]. . . | 2 |
| 1.2 | Division of the different TPS classes as a function of stagnation pressure and peak heat flux. Lower density materials are adequate for less demanding environment while missions which environments are more demanding require higher density materials. Credit: NASA. | 5 |
| 1.3 | NASA missions in chronological order from the '60s to the early 2000 as a function of peak heat flux in W/cm^2 . The name of the ablative material employed is indicated for every mission. Credit: NASA. | 6 |
| 1.4 | TPS mass fraction of NASA missions from the '60s to the early 2000 as a function of total heat load expressed in W/cm^2 . There is a clear dependency between this value and the TPS mass fraction. Credit: NASA. | 6 |
| 1.5 | Section of the heat shield used in the Galileo mission before and after the atmosphere crossing. The after image clearly shows how the ablator thickness at the centre of the capsule was overestimated while the protection towards the capsule shoulder was almost not thick enough to produce the right protection. Credit: NASA. | 7 |
| 1.6 | Atmospheric Re-entry Demonstrator (ARD) before and after its passage through Earth's atmosphere. The image on the left shows the virgin material while the image on the right shows the pyrolyzed heat shield. Credit: ESA. | 10 |

List of Figures

| | |
|---|----|
| 1.7 Huygens Descent Module and its heat shield. This image shows the capsule being assembled in the clean room; the ablative tiles forming the TPS are clearly visible. Credit: ESA. | 11 |
| 1.8 Plasma test being performed on a PICA sample in the Aerodynamic Heating Facility (AHF) at NASA's Ames Research Center. The behaviour around the sample shoulder is influenced by significant multi-dimensional phenomena. Credit: NASA. | 17 |
| 2.1 Schematic description of the ablation process. It contains all of the processes occurring in the material thickness during the pyrolysis and all of the thermal energy forms which have to be taken into account when simulating this phenomenon. Credit: NASA. | 23 |
| 2.2 Flow chart describing the one dimensional version of the ARC code. | 32 |
| 2.3 Temperature trends at different times for the one-dimensional heat transfer case. | 35 |
| 2.4 Test case 2_1 comparison between FIAT, PATO and ARC temperature estimates for the two TPS boundary surfaces: the external, T_w , and the internal, TC9, surface. | 38 |
| 2.5 Test case 2_1 comparison between FIAT, PATO and ARC temperature estimates in various points inside the TPS thickness. The point locations are contained in Table 2.2. | 38 |
| 2.6 Test case 2_1 comparison between FIAT, PATO and ARC pyrolysis gas mass flow rate, \dot{m}_g , and char gas mass flow rate, \dot{m}_c | 39 |
| 2.7 Test case 2_2 comparison between FIAT, PATO and ARC temperature estimates for the two TPS boundary surfaces: the external, T_w , and the internal, TC9, surface. | 40 |
| 2.8 Test case 2_2 comparison between FIAT, PATO and ARC temperature estimates in various points inside the TPS thickness. The point locations are contained in Table 2.2. | 40 |

List of Figures

| | |
|---|----|
| 2.9 Test case 2_2 comparison between FIAT, PATO and ARC pyrolysis gas mass flow rate, \dot{m}_g , and char gas mass flow rate, \dot{m}_c | 41 |
| 2.10 Test case 2_2 comparison between CMA/FIAT and ARC evaluation of the recession occurred during the simulation illustrated as a function of time. | 41 |
| 2.11 Test case 2_3 comparison between FIAT, PATO and ARC temperature estimates for the two TPS boundary surfaces: the external, T_w , and the internal, $TC9$, surface. | 44 |
| 2.12 Test case 2_3 comparison between FIAT, PATO and ARC temperature estimates in various points inside the TPS thickness. The point locations are contained in Table 2.2. | 44 |
| 2.13 Test case 2_3 comparison between FIAT, PATO and ARC pyrolysis gas mass ow rate, \dot{m}_g , and char gas mass ow rate, \dot{m}_c | 45 |
| 2.14 Test case 2_3 comparison between CMA/FIAT and ARC evaluation of the recession occurred during the simulation illustrated as a function of time. | 45 |
| 2.15 Comparison between CMA, FIAT and ARC estimation of temperatures in various points inside the TPS thickness for the Mansour <i>et al</i> [35] test case performed using the TACOT material. | 49 |
| 2.16 Comparison between CMA, FIAT and ARC pyrolysis gas mass flux, m_g , and char mass flux, m_c , for the Mansour <i>et al</i> [35] test case performed using the TACOT material. | 50 |
| 2.17 Comparison between CMA, FIAT and ARC estimation of temperatures in various points inside the TPS thickness for the Mansour <i>et al</i> [35] test case performed using the PICA material. | 50 |
| 2.18 Comparison between CMA, FIAT and ARC pyrolysis gas mass flux, m_g , and char mass flux, m_c , for the Mansour <i>et al</i> [35] test case performed using the PICA material. | 51 |

List of Figures

| | | |
|-----|--|----|
| 3.1 | Heat flux trends, as a function of the distance from the stagnation point, for the three stagnation areas simulated; these are compared with the trend reported by Olynick <i>et al</i> [55] produced using a CFD code. All the trends are captured at the same time during the simulation. The spacecraft here simulated is the Stardust sample return capsule. | 57 |
| 3.2 | Description of the exchange of data between ARC and the aero-thermodynamic model. | 60 |
| 4.1 | Initial conditions for the Stardust simulation performed using HyFlow solver. On the left: Illustration of the Stardust Sample Return Capsule geometry and of the mesh utilized in the HyFlow calculation. On the right: Initial TPS thickness on the capsule surface; the 6 cm part is formed by PICA while the 3 cm is made of SLA 561 V. | 67 |
| 4.2 | Comparison of the heat flux at stagnation point as function of time. The dotted line is the heat flux evaluated by Olynick <i>et al</i> [55] using a CFD solver while the solid lines represent the heat flux estimated by HyFlow and the heat flux used to perform the analyses which correspond to 80% of the previous value. | 68 |
| 4.3 | Heat flux trend at the time of peak heat flux (54 s) along a Stardust capsule section passing for the stagnation point, compared with what reported by Olynick <i>et al</i> [55]. Simulated using HyFlow solver. | 69 |
| 4.4 | Heat flux distribution [W/m^2] on the windward surface of the Stardust capsule at the time of peak heat flux (54 s). Simulated using HyFlow solver. | 69 |
| 4.5 | Comparison of the temperature at the stagnation point as function of time evaluated by the current study and by Olynick <i>et al</i> [55] for the Stardust capsule. Simulated using HyFlow solver. | 70 |

List of Figures

| | | |
|------|--|----|
| 4.6 | Temperature trend as a function of time at various thickness locations for the stagnation point; T wall, equivalent to $x=0$ mm, represents the wall temperature while T int, equivalent to $x=60$ mm represents the temperature for the internal TPS surface. Stardust test case simulated using HyFlow solver. | 71 |
| 4.7 | External temperature distribution [K] of windward surface of the Stardust capsule at the time of peak heat flux (54 s). Simulated using HyFlow solver. | 72 |
| 4.8 | External temperature trend at the time of peak heat flux (54 s) along a Stardust capsule section passing for the stagnation point. Simulated using HyFlow solver. | 72 |
| 4.9 | Comparison between a section of the geometry at the beginning of the analysis and a section of the geometry after the analysis was completed (80 s) for the Stardust test case using HyFlow solver. | 73 |
| 4.10 | Recession [m] of the Stardust capsule forebody at the end of the simulation (80 s). Test case performed using HyFlow solver. | 74 |
| 4.11 | Recession of the capsule as a function of the distance from the stagnation point along the the capsule geometry at the end of the simulation (80 s) for the Stardust test case and HyFlow coupled methodology. Compared with the recession reported by Olynick <i>et al</i> [55] | 74 |
| 4.12 | Illustrations of the Stardust Sample Return Capsule geometry and of the mesh utilized in the FOSTRAD calculation. | 75 |
| 4.13 | The heat flux at the stagnation point as a function of time as calculated by FOSTRAD for the Stardust test case. | 76 |
| 4.14 | The external temperature at the stagnation point as a function of time generated by ARC utilizing FOSTRAD heat flux estimates. | 77 |
| 4.15 | Heat flux [W/m^2] distribution on the windward surface of the Stardust capsule at the time of peak heat flux (54 s). Simulation performed utilizing FOSTRAD solver. | 78 |

List of Figures

| | |
|---|----|
| 4.16 Heat flux trend at the time of peak heat flux (54 s) along a Stardust capsule section passing for the stagnation point. Simulation performed utilizing FOSTRAD solver. | 78 |
| 4.17 External temperature distribution [K] on the windward surface of the Stardust capsule at the time of peak heat flux (54 s). Simulation performed utilizing FOSTRAD solver. | 79 |
| 4.18 External temperature trend at the time of peak heat flux (54 s) along a Stardust capsule section passing for the stagnation point. Simulation performed utilizing FOSTRAD solver. | 79 |
| 4.19 Recession [m] of the capsule at 80 s. Stardust test case performed utilizing FOSTRAD solver. | 80 |
| 4.20 Recession of the Stardust capsule as a function of the distance from the stagnation point along the the capsule geometry at 80 s. Simulation performed utilizing FOSTRAD solver. | 80 |
| 4.21 Comparison between a section of the Stardust geometry at the beginning of the analysis and a section of the geometry after 80 s. Simulation performed utilizing FOSTRAD solver. | 81 |
| 4.22 Illustration of the Atmospheric Re-entry Demonstrator Capsule geometry and of the mesh utilized in the HyFlow calculation. | 83 |
| 4.23 Comparison of the heat flux at stagnation point as function of time. The blue line is the heat flux evaluated by Tran <i>et al</i> [64] while the red line represents the heat flux used to perform the analyses which correspond to 80% of the value calculated by HyFlow. Atmospheric Re-entry Demonstrator test case. | 84 |
| 4.24 Temperature trends as a function of time at various thickness locations for the stagnation point; T wall, equivalent to $x=0$ mm, represents the wall temperature while T int, equivalent to $x=10$ mm, represents the temperature for the internal TPS surface. Atmospheric Re-entry Demonstrator test case simulated using HyFlow. | 85 |

List of Figures

| | |
|--|----|
| 4.25 Heat flux distribution [W/m^2] on the windward surface of the capsule at the time of peak heat flux (4939 s). Atmospheric Re-entry Demonstrator test case simulated using HyFlow. | 86 |
| 4.26 Heat flux trend at the time of peak heat flux (4939 s) along a capsule section passing for the stagnation point. Atmospheric Re-entry Demonstrator test case simulated using HyFlow. | 86 |
| 4.27 External temperature distribution [K] of windward surface of the capsule at the time of peak heat flux (4939 s). Atmospheric Re-entry Demonstrator test case simulated using HyFlow. | 87 |
| 4.28 External temperature trend at the time of peak heat flux (4939 s) along a capsule section passing for the stagnation point. Atmospheric Re-entry Demonstrator test case simulated using HyFlow. | 87 |
| 4.29 Recession distribution [m] on the windward surface of the capsule at the end of the simulation. Atmospheric Re-entry Demonstrator test case simulated using HyFlow. | 88 |
| 4.30 Recession of the capsule as a function of the distance from the stagnation point along the the capsule geometry at the end of the simulation. Atmospheric Re-entry Demonstrator test case simulated using HyFlow. | 88 |
| 4.31 Front and side representation of the Pathfinder geometry as it is utilised for the simulations in HyFlow. | 90 |
| 4.32 Comparison of the heat flux as a function of time at the stagnatiuon point between the estimation presented by Milos <i>et al</i> [32] and the values calculated by the code herein presented. | 91 |
| 4.33 Heat flux profiles along the capsule as presented in Milos <i>et al</i> [32] and as evaluated during this study for the time of peak heat flux (66 s). | 91 |
| 4.34 External temperature profiles along the capsule as evaluated during this study for the time of peak heat flux (66 s). | 93 |
| 4.35 Recession profiles along the capsule as evaluated during this study at the end of the simulation. | 94 |

List of Figures

| | |
|--|-----|
| 4.36 Three-dimensional representations of the heat flux [W/m^2] at the time of peak heat flux (66 s) for the geometry surface. The upper half of the image represents the axi-symmetric case while the lower part illustrates the case with an angle of attack equal to 15 degrees. | 95 |
| 4.37 Three-dimensional representations of the external temperature [K] at the time of peak heat flux (66 s). The upper half of the image represents the axi-symmetric case while the lower part illustrates the case with an angle of attack equal to 15 degrees. | 96 |
| 4.38 Three-dimensional representations of the surface recession [m] at end of the trajectory for the geometry surface. The upper half of the image represents the axi-symmetric case while the lower part illustrates the case with an angle of attack equal to 15 degrees. | 96 |
| 5.1 Representation of the governing equations and the numerical methods used to describe and simulate a flow depending on Knudsen number regime. Credit: heattransfer.asmedigitalcollection.asme.org. | 102 |
| 5.2 Image of the micro-computed tomography scans performed at the Austrian Foundry Research Institute on the ASTERM material after the removal of air [67]. The red cubes represent the ablative material while the blue part represents the straw used to contain the material during the scan. | 103 |
| 5.3 Representation of a 100^3 voxel section of the micro-computed tomography scans: the figure on the left shows the pressure contours while the image on the right shows the Mach contours. | 104 |
| 5.4 Permeability Pressure trend for the virgin and charred state of the carbon material. | 109 |
| 5.5 Permeability-Pressure trend for the virgin and charred state of the cork material. | 111 |
| 5.6 Relation between the flow mean free path and pressure. | 113 |

List of Figures

| | | |
|------|--|-----|
| 5.7 | Representation of the mean free path changes due to pressure variations in comparison to the simulations cell size. Pin refers to the inlet pressure, which is the value used in Eq. 5.4. Figure scale 5000:1. | 113 |
| 5.8 | Error introduced by using a cell size larger than the mean free path and the trend line used to extrapolate the error value for different higher pressure value. | 115 |
| 5.9 | Permeability Temperature trend for the virgin and charred state of the carbon material. | 117 |
| 5.10 | Permeability Temperature trend for the virgin and charred state of the cork material. | 118 |

List of Tables

| | | |
|-----|---|-----|
| 1.1 | List of thermal protection system materials utilized by European missions as reported by Bouilly <i>et al</i> [15]. | 12 |
| 1.2 | List of ablative materials simulation tools available as reported by Lachaud <i>et al</i> [26]. | 15 |
| 2.1 | Summary of the environment properties for the TACOT test cases presented at <i>5th Ablation Workshop, Feb. 28th Mar. 1st 2012, Lexington, Kentucky</i> [50]. | 36 |
| 2.2 | Thermocouple positions for the test cases presented at <i>5th Ablation Workshop, Feb. 28th Mar. 1st 2012, Lexington, Kentucky</i> [50]. | 37 |
| 2.3 | Thermocouple positions as described by Mansour <i>et al</i> [35]. | 46 |
| 3.1 | Parameters describing the external gases surrounding the spacecraft in different simulation environments: ratio of specific heats, specific heat at constant pressure [J/kgK], gas constant [J/kgK] and Prandtl number. | 54 |
| 4.1 | Time instances for the Stardust sample return capsule re-entry trajectory. | 66 |
| 4.2 | Time instances of the re-entry trajectory for the Atmospheric Re-entry Demonstrator. | 82 |
| 4.3 | Martian atmosphere properties used in HyFlow. | 90 |
| 4.4 | Time instances for the Pathfinder Martian entry trajectory. | 92 |
| 5.1 | Composition of the fluid utilized during the simulation in mole fraction. | 108 |

List of Tables

| | | |
|------|--|-----|
| 5.2 | Permeability dependence upon pressure for the virgin state of the carbon material | 109 |
| 5.3 | Permeability dependence upon pressure for the charred state of the carbon material | 110 |
| 5.4 | Permeability dependence upon pressure for the virgin state of the cork material | 112 |
| 5.5 | Permeability dependence upon pressure for the charred state of the cork material | 112 |
| 5.6 | Absolute values of the error in the simulation results introduced by using a cell size larger than the mean free path. | 114 |
| 5.7 | Permeability dependence upon temperature for the virgin state of the carbon material. | 116 |
| 5.8 | Permeability dependence upon temperature for the pyrolysed state of the carbon material. | 116 |
| 5.9 | Permeability dependence upon temperature for the virgin state of the cork material. | 116 |
| 5.10 | Permeability dependence upon temperature for the pyrolysed state of the cork material. | 117 |
| 5.11 | Run time for the study of pressure dependency in the virgin carbon material. | 118 |
| 5.12 | Run time for the study of pressure dependency in the pyrolysed carbon material study. | 119 |
| 5.13 | Run time for the study of pressure dependency in the virgin cork material. | 119 |
| 5.14 | Run time for the study of pressure dependency in the pyrolysed cork material. | 119 |
| 5.15 | Run time for the study of temperature dependency in the virgin carbon material. | 119 |
| 5.16 | Run time for the study of temperature dependency in the pyrolysed carbon material. | 119 |

List of Tables

| | |
|---|-----|
| 5.17 Run time for the study of temperature dependency in the virgin cork material. | 119 |
| 5.18 Run time for the study of temperature dependency in the pyrolysed cork material. | 120 |

List of Symbols

| | |
|-------------|---|
| A | : pre-exponential constant, s^{-1} |
| B' | : dimensionless mass blowing rate |
| C_f | : local skin friction coefficient |
| C_H | : Stanton number for heat transfer |
| C_M | : Stanton number for mass transfer |
| c_p | : specific heat, J/kgK |
| E | : activation temperature, K |
| F | : viewfactor |
| F_{RA} | : Reynolds analogy factor |
| H | : recovery enthalpy, J/kg |
| h | : enthalpy, J/kg |
| \bar{h} | : partial heat of charring, J/k |
| K | : permeability, m^2 |
| k | : thermal conductivity, W/mK |
| K_B | : Boltzmann constant, J/K |
| Kn | : Knudsen number |
| \dot{m}_g | : pyrolysis gas mass flux, Kg/m^2s |
| Pr | : Prandtl number |
| q | : heat flux, W/m^2 |
| R | : specific heat at constant pressure, J/kgK |
| Rc | : radii of curvature |
| Re | : Reynolds number |

List of Symbols

| | |
|----------------|---|
| R_f | : temperature recovery factor |
| \dot{s} | : surface recession rate, m/s |
| T | : temperature, K |
| t | : time, s |
| u | : velocity, m/s |
| x | : space coordinate, m |
| α | : thermal diffusivity, m^2/s |
| α_w | : surface absorption |
| γ | : ratio of specific heats |
| Γ | : volume fraction of the resin |
| ϵ | : surface emissivity |
| η | : number of atoms per unit volume, m^{-3} |
| θ | : local inclination |
| ι | : ratio radii of curvature |
| Λ | : reference area, m^2 |
| λ | : blowing reduction parameter |
| μ | : viscosity <i>Pas</i> |
| ρ | : density, kg/m^3 |
| σ | : Stefan-Boltzman constant, $W/m^2 \cdot K^4$ |
| τ | : virgin mass fraction |
| ϕ | : decomposition reaction order |
| $\dot{\Omega}$ | : volumetric flow rate, m^3/s |

List of Symbols

Subscripts

- A : denotes components A
- a : adiabatic
- axi : axisymmetric point
- B : denotes components B
- C : denotes components C
- c : charred
- cond : conductive
- e : boundary layer edge
- g : pyrolysis gas
- i : i component (A,B and C)
- rad : radiative
- s : stagnation point
- v : virgin
- y : local for the y panel
- w : wall
- ∞ : free stream flow

List of Acronyms

| | | |
|----------|---|--|
| ABLAMOD | : | Advanced Ablation Characterization and Modelling |
| ACE | : | Aerotherm Chemical Equilibrium |
| ARC | : | Ablative Response Code |
| ARD | : | Atmospheric Re-entry Demonstrator |
| BLIMP | : | Boundary-Layer Integral-Matrix Procedure |
| CAT | : | Charring Ablator Thermal response model |
| CEA | : | Chemical Equilibrium with Applications |
| CFD | : | Computational Fluid Dynamics |
| CMA | : | Charring Material thermal response and Ablation computer program |
| DSMC | : | Direct Simulation Monte Carlo |
| EDM | : | ExoMars Descent and Landing Demonstrator Module |
| FIAT | : | Fully Implicit Ablation and Thermal Analysis Program |
| FOSTRAD | : | Free Open Source Tool for Re-entry of Asteroids and Debris |
| μ CT | : | micro-Computed Tomography |
| MOPAR | : | MOdelling of Pyrolysis and Ablation Response |
| MSL | : | Mars Science Laboratory |
| PATO | : | Porous material Analysis Toolbox based on OpenFOAM |
| PICA | : | Phenolic Impregnated Carbon Ablator |
| SRC | : | Stardust sample return capsule |
| TACOT | : | Theoretical Ablative Composite for Open Testing |
| TC | : | Thermocouple |
| TPS | : | Thermal protection system |

Chapter 1

Introduction

When an object crosses the atmosphere of a planet at orbital speeds, it is exposed to a particularly hostile environment. In order to reach the planet surface in good conditions while maintaining structural integrity, this body has to be able to withstand the significant heat generated by the atmospheric entry. For this reason, spacecraft that need to perform such a task require Thermal Protection Systems (TPSs). TPSs enable a wide variety of space missions varying from exploration of other planets or bodies in our solar system to bringing back to Earth astronauts from the International Space Station (ISS).

The ability to safely cross a planet's atmosphere allows us to carry out tests and analyses on the surface of that planet which could not be performed by an orbiting spacecraft. Moreover, TPSs enable us to bring samples back to Earth and perform analyses on these samples in our best laboratories. Without an effective TPS, these missions could not be achieved, with a great loss for the scientific community.

Depending on the mission goal, different types of TPSs can be selected. The most common division is between reusable and non-reusable TPSs. Reusable TPSs are called in such a manner because, since the materials performing the protection task should not be damaged by the atmospheric entry, the same TPS can be used for multiple missions without major refurbishment between consecutive uses. This is the concept used for the development of the Space Shuttle. These types of TPS are formed by highly insulating materials which can keep the structure of the spacecraft at a low

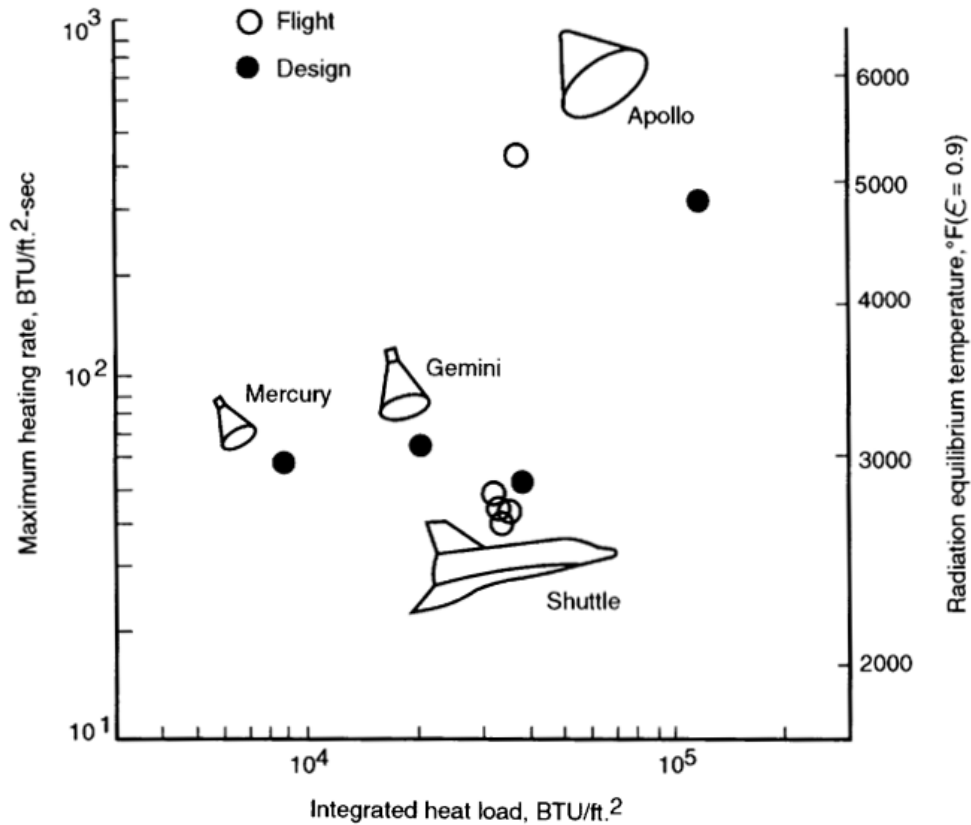


Figure 1.1: TPS design and flight test environments as presented by Curry [13].

enough temperature value as to avoid compromising its structural integrity and to comply with instrumentation temperature requirements. As Fig. 1.1 shows, they can only be used for moderate external heating because their only means of protection from the extreme heat of the external environment are insulation and radiation; they cannot use more efficient ways to dissipate thermal energy such as pyrolysis. Moreover, the experience of the Space Shuttle shows that the TPS may undergo damage after the entry that can be more or less extensive; therefore, the damaged parts of the systems cannot be used for the next mission and must be replaced, defeating one of the main purpose of the system: its re-usability. For these reasons they are not used if they are not strictly required.

Non re-usable TPSs are formed of materials that undergo a phenomenon called pyrolysis, during the atmospheric crossing. This process is endothermic, and it consumes

Chapter 1. Introduction

part of the thermal energy that the body has to be protected from. The pyrolysis also produces a degradation in the material, thus its non re-usability. Materials which undergo pyrolysis are called ablative materials and the work presented in this document focuses on them. Ablative materials are usually characterized by a high porosity, resulting in a low density. This makes them suitable candidates for space applications, where the weight of any component has to be as low as possible. For this reason, for their reliability and their ability to withstand extremely elevated temperatures they are the most common type of TPS.

TPSs represent a one-point failure system, which means that in the case of failure the entire mission can be compromised. The main challenge, as in every space system, is to optimize the material in order to avoid any unnecessary weight for the spacecraft. Furthermore, in ablative materials design, it is important to find the right balance between insulating and ablative properties [1]. An elevated density leads to a higher material strength but also increases the thermal conductivity. Less dense materials tend to have higher insulating properties while denser materials tend to ablate better. Too much ablation can cause an excessive change in the capsule shape while a very good insulator might be inadequate for the mission heat load. Selecting an ablative material used for elevated heat loads and employing it for a moderate heat load could seem a reasonable way to generate a conservative TPS configuration. However, if the thermal energy is not high enough, the ablation does not start which means that the TPS loses its main process for thermal protection. The correct balance between insulation and ablation, along with a precise assessment of the entry environment are fundamental for the design of a reliable and effective TPS. In addition to these prerequisites, ablative materials have to satisfy particular requirements depending on the specific mission (e.g. for Mars entries dust erosion must be considered as well as the high concentration of carbon dioxide in the atmospheric composition). All of the above criteria must be fulfilled by the selected material. Moreover, every mission is unique and small changes regarding the mission characteristics, such as entry velocity and landing location, can lead to non-negligible changes in the external heating.

Ablators are usually divided into categories based on their density, as it is shown

in Fig. 1.2 containing examples of NASA missions. Each of these categories is optimal for different entry conditions and characteristics. Selecting the wrong ablator leads to a non-optimized TPS mass fraction and therefore to a non-minimum weight of the system.

It is clear that designing an ablative TPS is not a trivial job and several analyses must be completed in order to perform this task correctly.

1.1 Historical Overview of ablative TPS Development

The early development of ablative TPSs started after World War II and was carried out by the U.S.A. and U.S.S.R. militaries. New materials able to protect the missiles from the extreme conditions encountered during their hypersonic flight and their descent (in case of intercontinental missiles) were necessary to avoid missile failure. Soon after, non reusable TPSs started being designed and employed in the race to space and the Moon.

A brief overview of past U.S. and European missions using ablative materials is hereafter presented. This section is not intended to be an exhaustive summary of all of the past performed missions, but it focuses on some of the most challenging and interesting ones in terms of atmospheric entries.

1.1.1 NASA missions

During the 60s till the mid 70s, NASA developed several ablative materials used in the space and Moon race. After the 70s the ablative TPS industry became way less active and reusable materials, to be used on the Space Shuttle program, became the focus. In the last couple of decades, NASA has been using already developed materials for its missions, instead of producing new ones optimized for the mission constraints. Lately, there has been a new focus on ablators because, future target missions regarding sample return from different bodies of interest in our solar system and planetary explorations are characterized by more challenging environments than past missions. Furthermore, a lower TPS mass fraction is desired in these new missions in order to maximize the

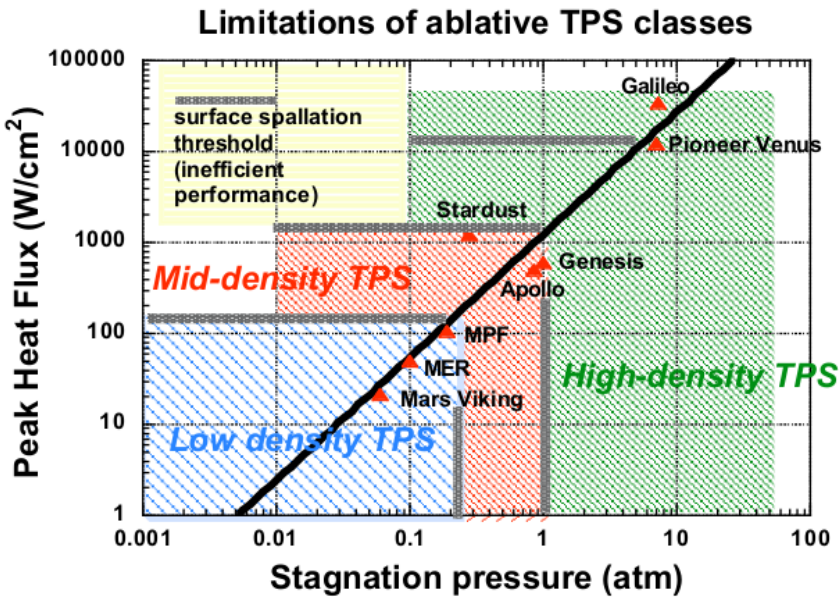


Figure 1.2: Division of the different TPS classes as a function of stagnation pressure and peak heat flux. Lower density materials are adequate for less demanding environment while missions which environments are more demanding require higher density materials. Credit: NASA.

weight that can be utilized for the on-board instruments.

Fig. 1.3 shows NASA missions that have used an ablative TPS since the '60s to the early 2000; it also indicates the peak heat flux value of the missions in order to give a better understanding of the entry environment conditions. This figure illustrates that a great variety of atmospheric conditions have been successfully withstood by U.S. ablative materials. Fig. 1.4 reports the same missions as Fig. 1.3 and it points out how the TPS mass fraction is a function of the total heat load and not the peak heat flux or the stagnation pressure. These figures also reveal the limited number of different ablative materials used in almost five decades of space missions.

The Galileo mission, as illustrated by Fig. 1.2, Fig. 1.3 and Fig. 1.4, was one of the most demanding atmospheric entries NASA had to deal with. The Galileo probe entered Jupiter's atmosphere on the 7th December 1995 with a relative velocity of 47.4 km/s . The peak heat flux was in the order of 30 kW/cm^2 and a heat load of 300 kJ/cm^2 [2], [3]. The forebody TPS thickness varied from a maximum of 14.6 cm to a minimum of 5.1 cm of fully dense carbon phenolic material, $\rho = 1450 \text{ kg/m}^3$, for a total initial weight

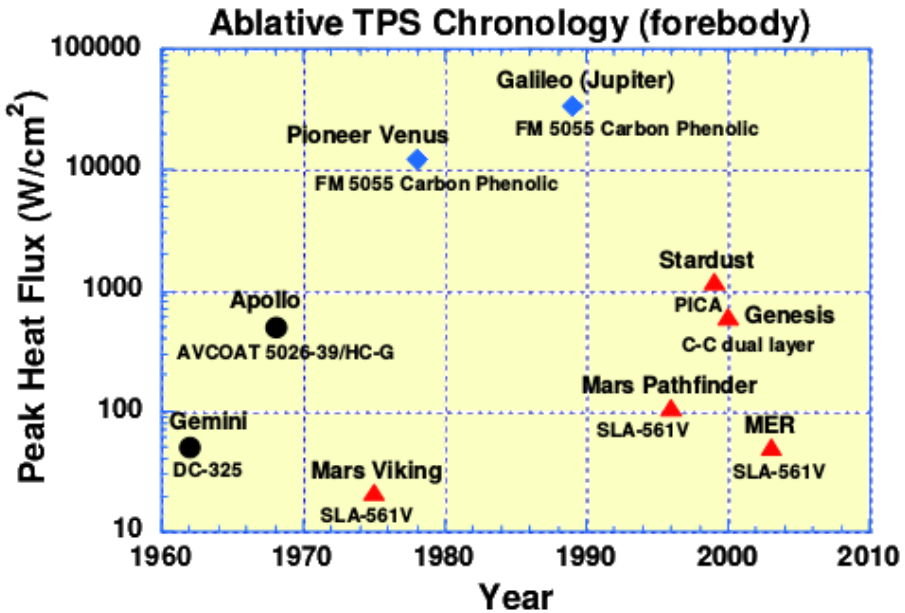


Figure 1.3: NASA missions in chronological order from the '60s to the early 2000 as a function of peak heat flux in W/cm^2 . The name of the ablative material employed is indicated for every mission. Credit: NASA.

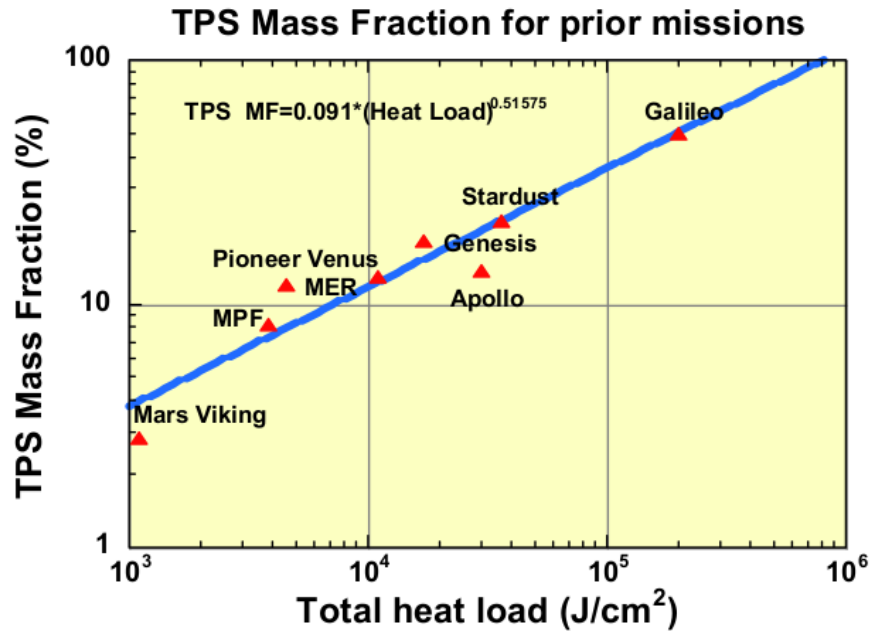


Figure 1.4: TPS mass fraction of NASA missions from the '60s to the early 2000 as a function of total heat load expressed in W/cm^2 . There is a clear dependency between this value and the TPS mass fraction. Credit: NASA.

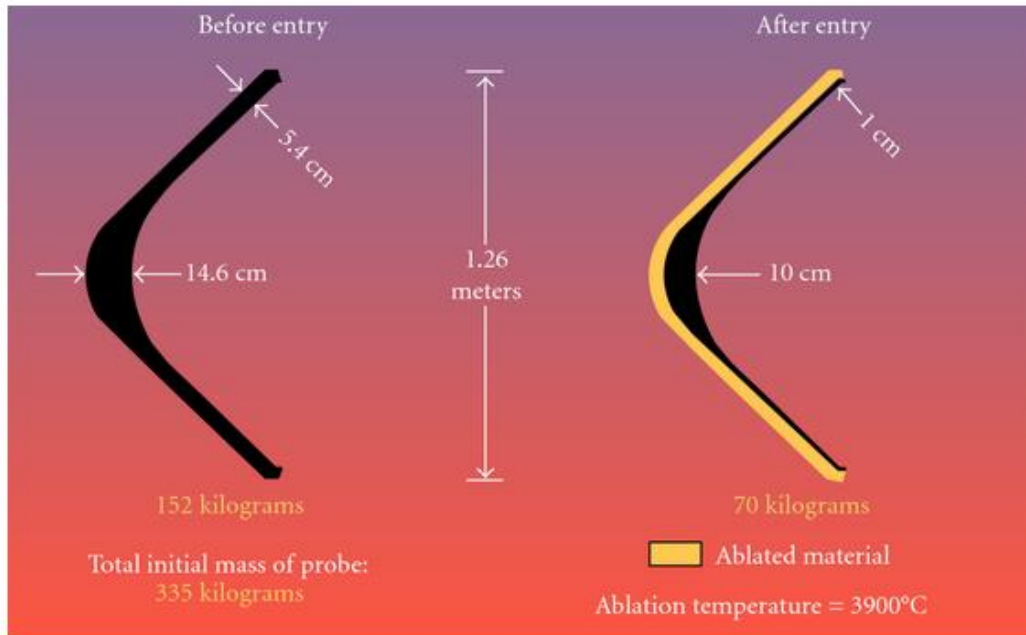


Figure 1.5: Section of the heat shield used in the Galileo mission before and after the atmosphere crossing. The after image clearly shows how the ablator thickness at the centre of the capsule was overestimated while the protection towards the capsule shoulder was almost not thick enough to produce the right protection. Credit: NASA.

of 150 kg and a TPS mass fraction of almost 50% [4]. As shown by Fig. 1.5, the recession of the heat shield was different from the estimated one. In particular the area surrounding the centre of the capsule experienced a smaller recession than expected while the shoulder recession was higher than estimated and almost experienced a burn through. Because of the complexity of the Jovian atmosphere environment, simulation tools are still not able to reproduce these results. In any case, the mission outcomes point out how important it is to precisely evaluate the ablative material behaviour on the entire heat shield geometry.

Mars has been a body of interest for decades. The first soft landing on its surface was achieved with the Mars Viking program in 1976 [5]. The environment experienced during a Martian atmosphere crossing, is less demanding than an Earth re-entry and, indubitably, than a Jupiter entry. Even if the maximum heat flux encountered for Mars is significantly lower than other planet' heating (Fig. 1.2), other challenges have to be

Chapter 1. Introduction

overcome during this type of missions. The Viking capsule used SLA 561V as its ablator; this material is composed of a mixture of cork, silica and phenolic micro-spheres in a silicone binder [6], with a density of 256 kg/m^3 [7], and it was specifically developed for the mission. The same material has been used for the entry of Mars Pathfinder in 1997, even if the entry velocities differ one from another: 4.5 km/s for the Viking entries and 7.5 km/s for the Pathfinder capsule [8]. The main difference between the two heat shields was the use of a spray-able version of the same material, SLA 561S, on the afterbody of the most recent capsule. Mars Exploration Rovers (MER) spacecraft employed Pathfinder heat shield configuration for their Martian entries in 2004. Their entry velocity was 5.6 km/s [8].

Mars Science Laboratory (MSL) was the last big mission which brought a rover on the Martian surface. The capsule landed on the 5th of August 2012. At the beginning of its design, SLA 561V was selected for the heat shield but, after testing and analysing its performances, it was decided to substitute it with PICA, Phenolic Impregnated Carbon Ablator [9]. This material is formed by a low density fibrous substrate impregnated with a phenolic resin; several PICA versions exist, and its density can vary from 225 to 1041 kg/m^3 with the low density version being the most widely used [10]. The thickness of the MSL ablative TPS was constant on the entire forebody and was equal to about 3 cm [11]. The spacecraft entry velocity was not too high, 5.9 km/s , however its size and weight were higher than any other capsule sent to Mars.

Regarding Earth re-entry, the NASA missions which firstly used ablative materials were the missions involved in bringing humans into space and on the Moon; such as the Mercury, Gemini and Apollo programs [12] [13]. The first NASA manned capsule was part of the Mercury program. Mercury re-entries started from 120 km and had an entry velocity of about 8 km/s ; they remained sub-orbital for all of the launches. The heat shield option finally selected, was formed by ablative material consisting of fiberglass phenolic which was utilized in six different launches, four unmanned and two manned.

The Gemini capsule and re-entry characteristics were very similar to the Mercury program. The capsule size was increased to allow an additional crew member. The

Chapter 1. Introduction

entry velocity was comparable to the Mercury one, about 8 km/s , however the ablative material was changed and was formed by a phenolic honeycomb filled with silicone elastomer [14].

The Apollo program brought humans on the Moon. The capsule used in these missions had to withstand a more challenging environment because of the elevated entry velocity, about 11 km/s , the bigger weight of the capsule itself, and the consequential higher thermal energy to be dissipated. A version of the Avcoat material, Avco 5026-39G, was selected for the heat shield. This material is formed by an epoxy-novalac resin reinforced with quartz fibers and phenolic micro-balloons; its density is about 500 kg/m^3 , thus Avcoat is considered a mid-density material. After the conclusion of these programs, the focus shifted from ablators to reusable material to be employed in the Space Shuttle. Currently, the Space Shuttle is no longer in use and the Russian Soyuz vehicle is used to ferry astronauts to and from the ISS. This capsule heat shield is formed two materials: PKT-11K-FL, with an average density of $1200\text{-}1400 \text{ kg/m}^3$, which is laminated plastic based on a silicon dioxide and a phenolic formaldehyde adhesive, and VIM-2, with an average density of $140\text{-}150 \text{ kg/m}^3$, that is a fibrous material based on a super thin silicon dioxide fibers and an organosilicon adhesive. To stop being dependant on Roscosmos (the Russian Space Agency) for astronaut transport, different new options are being studied for NASA. These options need state of the art materials and simulation tools for their design.

1.1.2 European missions

ESA missions requiring a thermal protection system are fewer than NASA's ones, therefore there are less European materials available with respect to the US. Table 1.1 contains the materials currently available as reported by Bouilly *et al* [15].

ExoMars 2016, with the Descent and Landing Demonstrator Module (EDM) Schiaparelli, was the latest ESA mission which employed an ablative TPS. Schiaparelli landed on the Martian surface on the 24th of May 2017 [16], [17]. Even if the descent was unsuccessful, an investigation has declared that the failure was not due to any TPS malfunction [18]. The TPS was formed of NORCOAT-LIEGE for both the

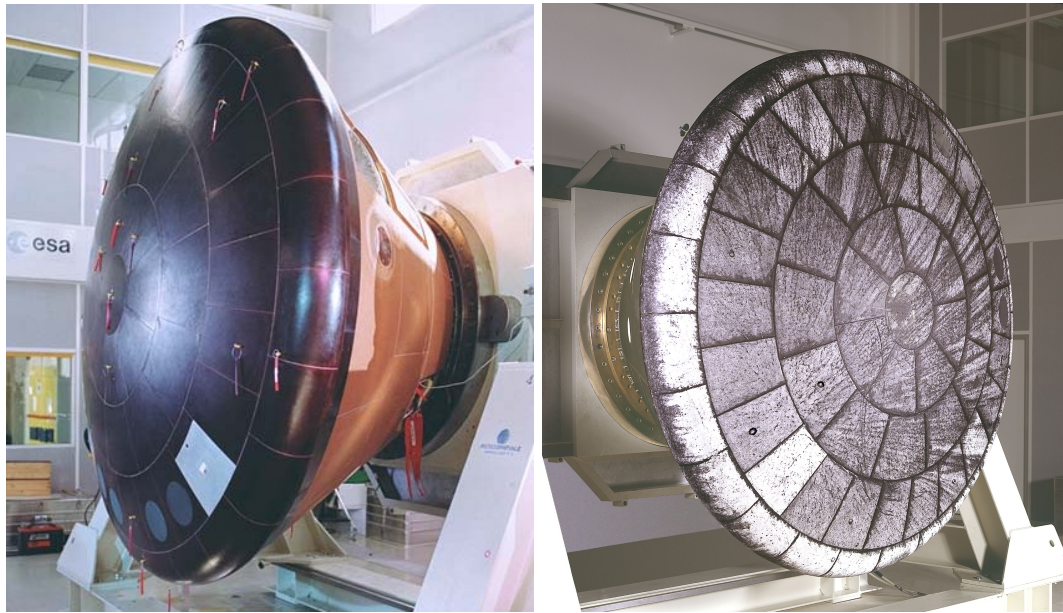


Figure 1.6: Atmospheric Re-entry Demonstrator (ARD) before and after its passage through Earth’s atmosphere. The image on the left shows the virgin material while the image on the right shows the pyrolyzed heat shield. Credit: ESA.

windward and leeward surfaces [19]. This ablator main components are cork particles and phenolic resin and it has a density of 470 kg/m^3 [15], [19]. NORCOAT-LIEGE was also used for the Beagle2 mission, landed in 2003, and on the back shield of the Atmospheric Re-entry Demonstrator (ARD) launched in 1998, Fig. 1.6. Because of the higher heat load that usually characterises Earth re-entry, ARD front shield was formed of ALEASTRASIL tiles, a denser material, 1650 kg/m^3 , whose components are silica fabric and phenolic resin [15].

Huygens is another interesting and challenging mission designed and launched by ESA [20]. The probe, Fig. 1.7, landed on Saturn’s moon, Titan, on January 2005 [21]. AQ 60, a low density material (300 kg/m^3) made of silica fiber in a phenolic resin was used for the front heat shield while the leeward structure was directly sprayed with Prosial, a silica sphere and silicon elastomer mixture with a density of about 560 kg/m^3 [20]. The entry was successful, and the probe safely landed on Titan’s surface.

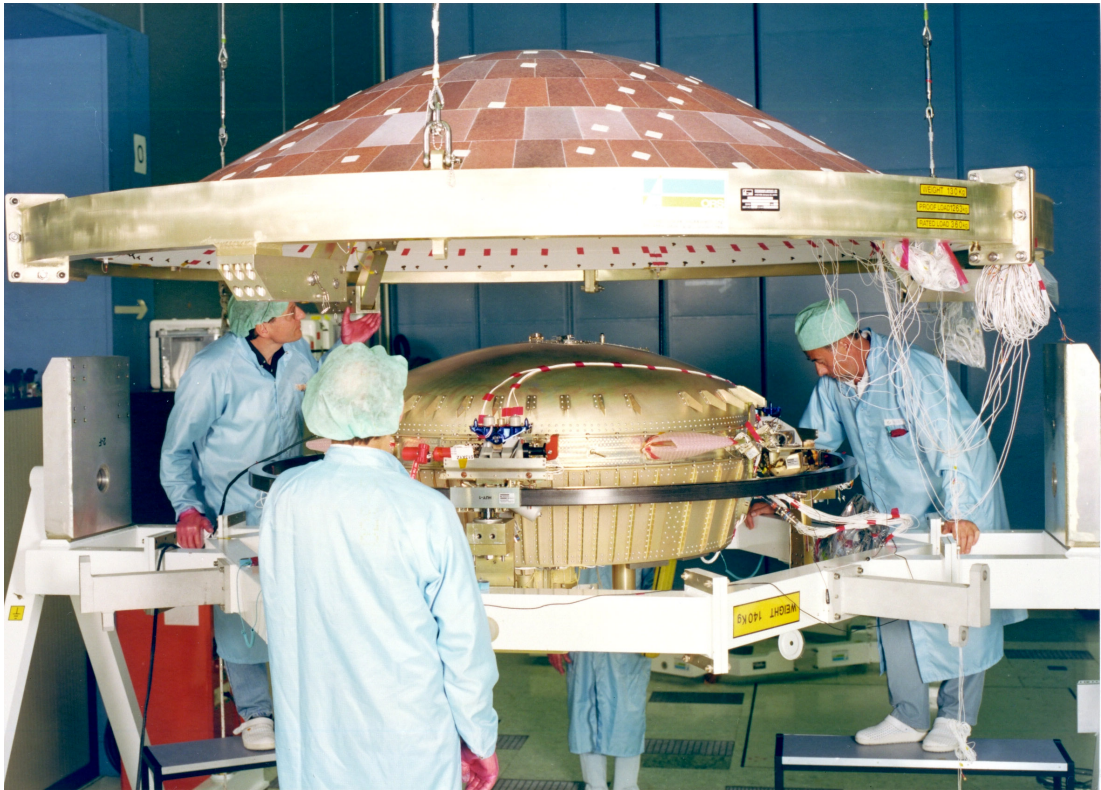


Figure 1.7: Huygens Descent Module and its heat shield. This image shows the capsule being assembled in the clean room; the ablative tiles forming the TPS are clearly visible. Credit: ESA.

1.1.3 Future needs

In their paper, Bouilly *et al* [15] produced an overview of past European missions and needs for future missions. They assess that NORCOAT-LIEGE is a good option for low density materials and can be used for Martian and Titan explorations. They add that some investigations might be useful for long term missions, where mass requirements might be more stringent. Unfortunately, Europe lacks reliable medium density materials for re-entry missions. The option currently available is the ALEASTRASIL material whose density is quite higher than the equivalent NASA material, leading to a great disadvantage in terms of TPS mass fraction. It is also not recommended to rely on NASA materials because of the U.S. export regulations. Materials for giant planets exploration, are also missing from the European portfolio. To fill these gaps and to be able to meet the requirements of future missions, Europe needs the development of new

Chapter 1. Introduction

Table 1.1: List of thermal protection system materials utilized by European missions as reported by Bouilly *et al* [15].

| Material | Development date | Density [kg/m3] | Application for entry vehicles |
|---------------|------------------|-----------------|--------------------------------|
| ALEASTRASIL | 1975 | 1650 | ARD |
| AQ60 | 1980 | 300 | Huygens |
| NORCOAT-LIEGE | 1975 | 470 | ARD, Beagle2, Schiaparelli |
| PICSIL | 1995 | 410 | MSTP-CTV studies |
| PROSIAL | 1980 | 540-600 | Huygens |
| DO31 / SPA | 1988-93 | 660 | Mirka |

materials and further investigations of available materials. In this framework, the development and improvement of simulation tools can only be beneficial and preparatory to meet this goal.

Likewise, NASA has produced multiple studies regarding the needs of future exploratory missions in terms of TPS. Venkatapathy *et al* [22] analysed the most interesting scientific targets for the near future, and the missions which are required to tackle these targets. The paper focuses on the necessity of certification of new and old materials. It explains that the capability to properly simulate the in-flight conditions is very rare even with state of the art plasma and arc jet facilities. For this reason, they recommend the validation of material models, and specifically the models describing the surface interaction with the external environment and the in depth thermal response of the materials. To perform this recommended task it is necessary to have the right ablative simulation tools. For each target mission presented in that paper, a list of currently available suitable materials is presented with proposals for new developments when needed. For Saturn missions, carbon phenolic materials, heritage of the Galileo or Pioneer-Venus missions is suggested. These materials are no longer being produced and new studies and developments must occur in order for the new materials to be mission-ready. In the case of Titan missions, low density SIRCA and super light weight SLA 561 V are proposed. These materials successfully performed their task in multiple missions such as on-board of the Mars Pathfinder probe. However, more investigations regarding their failure modes are recommended in the paper. The TPS material selection for sample return missions, greatly depends on the capsule entry velocity. PICA, a

low density ablator and Avcoat, a mid density material, are advised for different entry velocities. Both of these materials have been successfully used in the past, however, new versions containing changes from the original materials, are being developed and need to be properly characterized. Similar studies were reported by Laub and Venkatapathy [23] and Young *et al* [24]. In these papers missions for Jupiter, Venus and Mars are also discussed. The conclusion is the same as the previous document: even if there are several materials available in different density categories, future missions require new TPS materials and concepts as well as thermal response models.

The analyses just presented confirm the need for new simulation tools and better material modelling if we want to be able to design adequate future missions TPS. The aim of the study presented in this thesis is, therefore, to properly solve both requirements highlighted in these papers. The need for new simulation tools is met thanks to the methodology presented in chapter 4, while an improvement in the material modelling is proposed in chapter 5. Both activity work synergistically to achieve the same goal: be better equipped to produce all of the different kinds of simulations that will be required to successfully meet TPS requirements for future missions.

1.2 Literature review

1.2.1 Thermo-ablative material response programs

As explained in the previous section, TPS requirements are mission-dependant and several analyses and optimization studies must be performed for the material selection. To perform this task, it is necessary to be able to simulate the various materials behaviour; this is the only way to select the optimal one for the mission requirements and the atmospheric environment that the TPS will have to withstand.

The pyrolysis phenomenon is very complex and not trivial to simulate but, for simplicity, it can be divided in two different problems: the evaluation of the material in-depth changes (calculated through in-depth energy balance equations) and the evaluation of the external heat flux (calculated solving the external surface boundary condition) [25]. The two problems affect each other, and they are also influenced by

Chapter 1. Introduction

the external environment, which in turn is affected by the pyrolysis products. A more precise description of the thermo-physics behind this is presented in section 2.1.

Since the late 60s, a considerable number of codes for the simulation of ablative materials behaviour have been developed. Lachaud *et al* [26] produced a list of currently available ablative codes, reported in this document in Table 1.2.

This table shows how the majority of the developed tools are from the U.S.A. and that the tools available in Europe are very limited. Most of these codes are commercial codes or are not openly available. The following section contains information regarding the most widely known and used of these programs.

CMA

The first publication describing an ablative thermal response code is the Aerotherm technical report dated 1968 [25]. This document describes various programs able to perform different types of simulations. The code developed for analyses regarding the in-depth response of charring material is called Charring Material thermal response and Ablation computer program (CMA). This program could operate independently or coupled with a boundary layer solver called BLIMP (Boundary-Layer Integral-Matrix Procedure) or with the Aerotherm Chemical Equilibrium (ACE) program, a surface thermochemistry code. As described in Version 3 User's manual [27]:

CMA is an implicit, finite-difference computational procedure for computing the one-dimensional transient transport of thermal energy in a three-dimensional isotropic material which can ablate from a front surface and which can decompose in-depth.

Decomposition reactions are based on a three component model.

CMA had also implemented three different options for the external surface, which is the ablating surface, boundary conditions depending on the known input, and the type of simulation to perform. Many versions of the CMA code exist, but the main features of the program remain unvaried through the versions.

Table 1.2: List of ablative materials simulation tools available as reported by Lachaud *et al* [26].

| Name | Owner | Applications |
|-------------|---------------------------|--------------|
| Amaryllis | Samtech, Belgium | Design |
| CAMAC | CSIST, Taiwan | Unknown |
| CAT | NASA ARC, USA | Analysis |
| CHALEUR | SNL, USA | Design |
| CHAP | Boeing, USA | Design |
| CMA | Aerotherm, USA | Design |
| CMA/SCMA | Tokyo Univ., Japan | |
| CMA/KCMA | ISA, France | Analysis |
| CODE-JSC | NASA JSC, USA | Analysis |
| CODE-LaRC | NASA LaRC, USA | Analysis |
| FABL | Fluid Grav. Eng. Ltd., UK | Analysis |
| FIAT | NASA ARC, USA | Design |
| 3DFIAT | NASA ARC, USA | Analysis |
| HERO | ATK, USA | Analysis |
| ITARC | ATK, USA | Design |
| libAblation | Univ. of Tex. Aust., USA | Analysis |
| MIG | Univ. of Flo., USA | Analysis |
| MOPAR | Univ. of Mich., USA | Analysis |
| NEQAP | N. Carol. St. Univ., USA | Analysis |
| NIDA | Univ. Alab. Birm., USA | Analysis |
| PATO | NASA ARC, USA | Analysis |
| STAB | NASA JSC, USA | Design |
| TITAN | NASA ARC, USA | Analysis |
| TMU | T. Modares Univ., Iran | Analysis |
| US3D | Univ. of Minn., USA | Analysis |

FIAT

The Fully Implicit Ablation and Thermal Analysis Program (FIAT) was developed at NASA Ames Research Center to solve some of the problems of the CMA code; specifically, the instability linked to the explicit scheme implemented in it [28]. FIAT is described by Milos *et al* [29] as:

FIAT simulates one-dimensional transient thermal energy transport in a multilayer stack of thermal protection system (TPS) materials and structure that can ablate from the top surface and decompose in-depth.

FIAT is a one-dimensional code which uses a finite volume method for the discretisation of the energy equations, and an implicit scheme to couple them to the heat flux equation. This code can be coupled with external flow solvers such as GIANTS [30] and GASP [31] and with thermo-chemistry programs such as MAT and ACE [25]. FIAT has been used to perform analysis of several missions such as Mars Pathfinder [32] and Stardust [28]; an improved version of the code called FIATv2 has been released in 2006 [29]. A three-dimensional version of the code, called 3-dimensional Finite-volume alternatively directional Implicit Ablation and Thermal response code (3dFIAT) [33], exists and it is used for three-dimensional test cases.

TITAN

The TITAN program was developed at NASA Ames Research Center to simulate cases which present two-dimensional behaviour and cannot be solved by codes such as CMA or FIAT. As FIAT, it is based on an implicit scheme and the finite volume method. To perform fully coupled studies, TITAN is integrated with the Navier-Stokes solver GIANTS and with the aero-thermal flow-field engineering correlation program MEIT [34]. The typical geometry studied with TITAN is a section of a three-dimensional object like arcjet or plasma test sample, as shown in Fig. 1.8. In this case the behaviour of the external edge of the sample, where the maximum curvature is, cannot be predicted using a one-dimensional program but requires a two-dimensional code to fully characterise the behaviour of the sample shoulder.

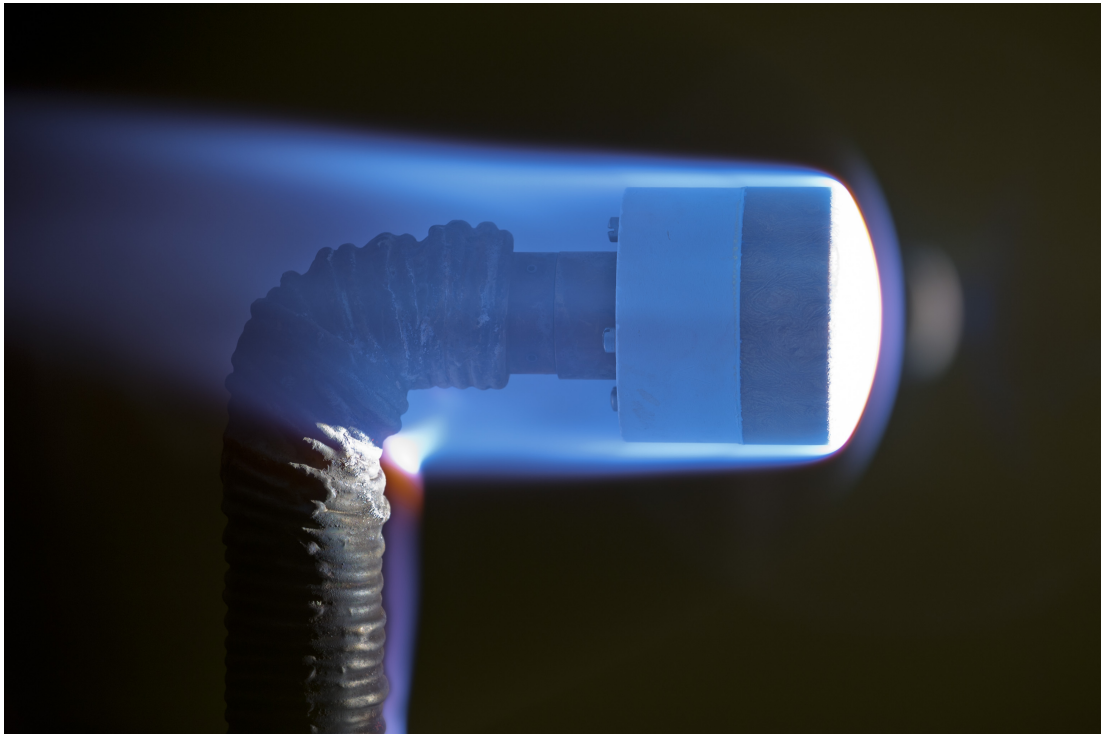


Figure 1.8: Plasma test being performed on a PICA sample in the Aerodynamic Heating Facility (AHF) at NASA’s Ames Research Center. The behaviour around the sample shoulder is influenced by significant multi-dimensional phenomena. Credit: NASA.

CAT

The Charring Ablator Thermal response model (CAT) is another tool developed at the NASA Ames Research Center [35]. The focus of this code is to better simulate the chemistry involved in the ablation process, and in particular in the pyrolysis gas in order to produce a more efficient coupling with CFD programs. This code has the ability to generate more precise results than the other codes previously presented for high speed atmospheric entry, where the interactions between the external fluid and the pyrolysis gas have an higher impact in the overall TPS behaviour.

PATO

The Porous material Analysis Toolbox based on OpenFOAM (PATO) [36], is a recent code implemented in the OpenFOAM open source framework. Because of the framework selected it uses the finite volume method with an implicit scheme. The governing

Chapter 1. Introduction

equations at the microscopic scale are volume-averaged into their macroscopic versions to increase the efficiency of the solver. This code can be used for the study of any porous material, but it was specifically developed for ablative materials. PATO's peculiarity is its modularity: the basic level, referred by Lachad and Mansour [37] as type 1, is an ablation solver based on the CMA code. This is the base layer for all of the code models. Type 2 adds momentum conservation, while type 3 include the species conservation equation and, in general, all of the phenomena that characterise the physics occurring inside a porous carbon-phenolic material. Type 2 and type 3 models are available for three-dimensional simulations. This code is coupled with the MULTicomponent Transport And Thermodynamic properties/chemistry for IONized gases (Mutation++) [38] library to solve the equilibrium chemistry equations.

MOPAR

MOPAR, MOdelling of Pyrolysis and Ablation Response, is an ablative response tool developed by the University of Michigan [39]. It uses the control volume finite element method and it replaces Darcy's law, the equation used to calculate the gas velocity to be used in the momentum equation, with Forchheimers law. MOPAR is strongly coupled with LeMANS, a finite volume Navier-Stokes CFD solver [40], [41].

Amaryllis

Amaryllis is a module of the software Samcef, which is a general purpose multi-physics software based on the finite element methodology [42]. Samcef-Amaryllis can simulate two-dimensional geometry thus it is commonly used for axis-symmetrical objects such as arc-jet or plasma wind tunnel test samples. Due to the different modules available in the Samcef software, Amaryllis can be easily coupled with aero-thermodynamic tools [43]. The code was developed by SAMTECH s.a., a Belgian subsidiary of Siemens PLM Software, which makes this one of the few European ablative response codes. This tool is used by ESA and its partners, such as Thales Alenia.

1.2.2 Coupled approaches

As illustrated in the previous section of this document, all of the ablative response programs can be coupled with an aero-thermodynamic model. The coupling of the two programs is performed to increase the precision of the results, taking into account the effects that the ablation products have on the external environment and how this influences the entire process.

To the author's knowledge, all of the aero-thermodynamic models used for the coupling with ablative simulation tool are CFD codes. This is also confirmed by Lachaud *et al* [26]: this paper reports "CFD coupling" as one of the features of the various codes and does not describe any different type of aero-thermodynamic model.

For the approach developed in this study, it was decided to use a different type of model for the coupling, and in particular, to use reduced order models. This decision was taken to reach the aim of a low computationally demanding methodology. Further details regarding the decision taken are described in next section while a more exhaustive description of the aero-thermodynamic models selected for this method is presented in chapter 3.

1.3 Contributions to the field

Ablative simulation tools vary from the most complex codes, which consider all of the phenomena occurring in the pyrolysis, to the simpler programs, which neglect part of the physics. Naturally, the most complex codes are the most time and resource consuming. During the various phases of a space mission design, different accuracies are required. Extremely precise codes could be a waste of resources in the early phases of a TPS design, when the right material is being selected; while a low precision in the final phases could lead to a non-optimized TPS mass fraction with a higher cost at launch or, even worse, to a lower than necessary TPS thickness which could be fatal for the mission. For these reasons, the research herein presented was divided in two major activities: the development of a low computationally demanding (fast) tool able to produce three-dimensional simulations of ablative material behaviour, to be used

Chapter 1. Introduction

in the preliminary phases of a mission project and the study of changes introduced in the permeability values by the external environment. Both activities are essential to reach one single goal: the improvement of the ablative material design and simulation in its entirety. Each of the activities targets a specific range of phases of the design and focuses on meeting that phase requirements and needs. Preliminary phases need fast tools to perform as many simulations as possible in order to select the best possible TPS architecture. The tool presented in this thesis is able of completing an entire three-dimensional atmospheric entry simulation in minutes. Naturally, the simulation duration varies depending on the spatial and time accuracy, but it remains faster than any CFD coupled methodology. The final phases of the design require a very high accuracy to produce results as close as possible to reality. The second activity herein presented studies a physical phenomenon which is usually neglected while simulating ablative material phenomena. Introducing this phenomenon in the TPS simulation can only increase the simulating tools accuracy and produce a better understanding of the ablator behaviour.

The first activity novelty does not lie in the development of the code, which is based on a CMA model [25], but on the application of this code. In particular the application of a one-dimensional code to produce three-dimensional results. The methodology used is based on the application of a one-dimensional problem on several points on the surface of a three-dimensional object. A more detailed description of this concept is given in section 3.3. This method can be applied because the one-dimensional effects, especially the external heating, are more significant than the two and three-dimensional effects such as adjacent points thermal conduction. This assumption is valid when the material is actively heated and, therefore, in those phases of the atmospheric entry which are studied for the design of the TPS and the sizing of the material. The methodology has, of course, some limitations as it is explained in Chapter 4 however, as it is illustrated in the same chapter, it produces reliable results for atmospheric entry of different planets. Avoiding the complexity of two and three-dimensional physics gives the advantage of a lighter and faster code. Moreover, the ablative response code is coupled with reduced order aero-thermodynamic models instead of being coupled with a CFD tool, as for all

Chapter 1. Introduction

of the codes presented in the literature review section. This produces a fast coupled solving tool able to generate three-dimensional evaluations of the TPS behaviour. To the author's knowledge, this is the only program of its kind both for the application of a one-dimensional ablative response solver to generate three-dimensional estimates and for the coupling with reduced order aero-thermodynamic models.

The second activity studies the changes that temperature and pressure variations cause on the material permeability. These results are to be used in conjunction with very precise simulation tools in order to increase their accuracy. In this case the novelty consists in the study of a property that is commonly considered temperature and pressure constant, and in the methodology utilized to calculate the results. In particular, the use of the DSMC method outside of its boundaries as explained in section 5.1.1.

The two studies target different phases of the missions design. Therefore, the intention of this work is to increase the simulation capabilities for ablative materials for a great variety of the mission design phases and in the development of new materials.

Chapter 2

One-dimensional ablative response code

This chapter introduces the one-dimensional version of Ablative Response Code (ARC). The first part provides a detailed explanation of the ablation phenomenon and the equations used to numerically simulate the ablative material behaviour. Particular attention is devoted in this section to explain the role of the governing equations and which terms of these equations were neglected during the implementation of the ARC code. The second part focuses on the computational procedure; it describes the methodology used to implement the governing equations in the code, and the approach employed to perform a simulation. The last section presents a verification of the one-dimensional code and illustrates several comparisons between ARC simulations and commercial code results.

2.1 Governing Equations

The pyrolysis phenomenon is relatively complex to simulate, due to the numerous physical changes happening in the material and the different energy forms which are active during a spacecraft atmospheric entry. Fig. 2.1 provides a summary of the phenomena occurring during ablation; in particular it contains the forms of thermal energy which must be considered when simulating this process. The thermal energy balance is one of the most important features in ablative material simulations because the amount of

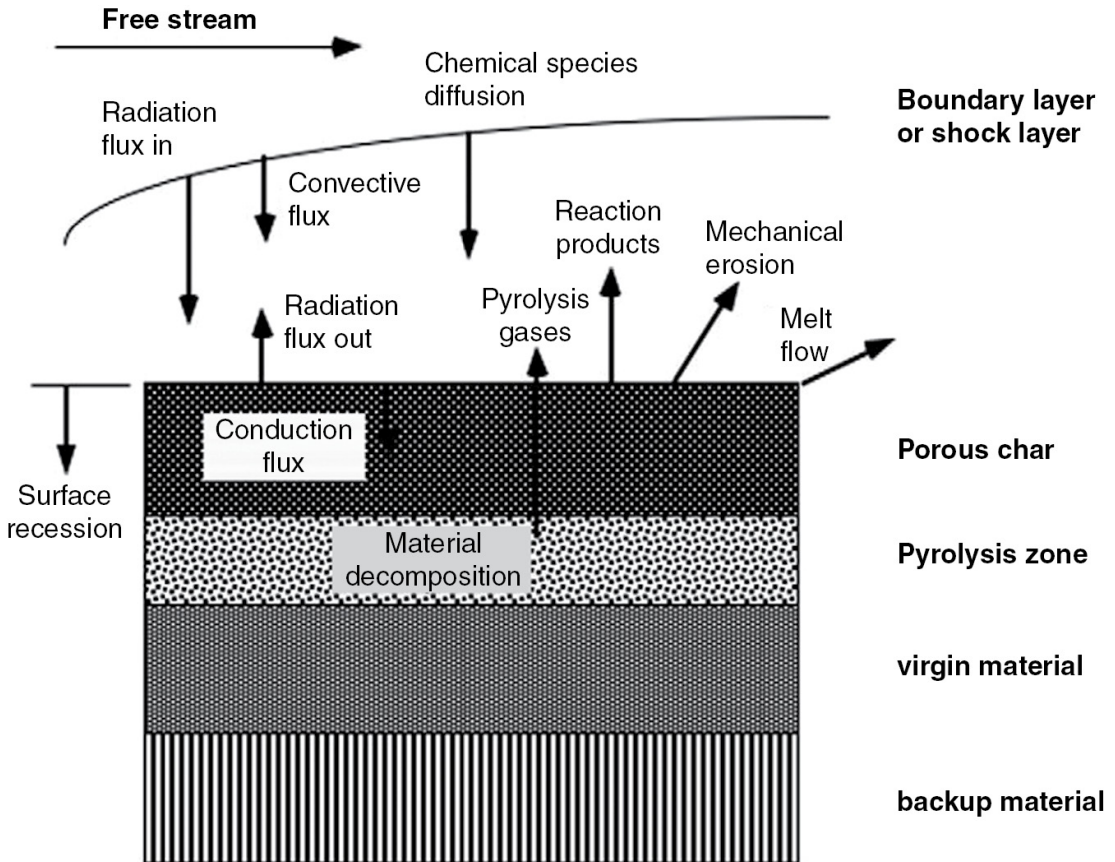


Figure 2.1: Schematic description of the ablation process. It contains all of the processes occurring in the material thickness during the pyrolysis and all of the thermal energy forms which have to be taken into account when simulating this phenomenon. Credit: NASA.

energy consumed during the pyrolysis, which is an endothermic process, is the major mechanism employed by these materials to perform their thermal protection task. Pyrolysis starts when the ablator is exposed to an external heat flux which increases the temperature of the material to the reaction threshold. If this temperature value is not reached, the material does not start to ablate and it is not able to perform the thermal protection task. Consequently, it is essential to conduct meticulous simulations of a mission atmospheric entry in order to select the best material for that specific mission.

The pyrolysis process consists of a change in the physical and thermal characteristics of the material; more precisely, its density decreases leading to a consumption of material; that is the reason why this change of state is referred to as degradation.

During this process the ablator produces pyrolysis gases, which emerge from the surface and create a second important effect in the spacecraft protection: the blocking effect. The blocking mechanism is produced by those pyrolysis gases which, while exiting from the ablator external surface, partially shield the TPS from the external heat flux.

Additionally, Fig. 2.1 illustrates the internal composition of the ablative material during the ablation; before the atmospheric entry, the TPS is fully formed by the virgin state of the material. While the pyrolysis proceeds, the material starts the transformation to the charred/pyrolyzed state; it is not an immediate transformation, therefore the material can exist in an intermediate state between virgin and charred. After some time, the material is as illustrated in Fig. 2.1: an external surface formed by fully charred material, a more internal layer characterized by the intermediate state and a fully virgin layer which has not yet reached the temperature required for pyrolysis. The thermo-physical characteristics of the virgin and fully charred layer are not constant but they are function of the temperature. In the intermediate layer these properties also depend on the temperature but, additionally, are a function of the charred level of the particular point of the material in the analysis.

All of the processes that take part in the pyrolysis and all of the changes happening in the material that were just illustrated, are essential to properly simulate the behaviour of any ablative material. This is the reason why the simulations of ablative TPS are not trivial to perform.

2.1.1 Degradation

The material change of state occurring during the pyrolysis phenomenon produces a degradation in the ablator and its components. Since the majority of charring materials behaves as three different ablative components independent from each other, as reported by Aerotherm technical report [25], a three component degradation was implemented in ARC. In case the material is described in literature as a single or dual component ablator, it is possible to consider one or two of these component degradations null or to impose the same degradation for two or three components. In the CMA approach, which is the one used for ARC, the material is supposed to be composed by three components:

a reinforced material and two resin fillers. The material density is calculated using Eq. 2.1, where the subscripts A , B and C refer to the different components and in particular A and B refer to the resin fillers, while the letter C refers to the reinforcing material; Γ is the volume fraction of the resin.

$$\rho = \Gamma(\rho_A + \rho_B) + (1 - \Gamma)\rho_C. \quad (2.1)$$

The pyrolysis process is described by an Arrhenius equation for each component:

$$\frac{\partial \rho_i}{\partial t} = A_i \left(\frac{\rho_i - \rho_{ic}}{\rho_{iv} - \rho_{ic}} \right)^{\phi_i} e^{-E_i/T}. \quad (2.2)$$

where A_i , E_i , ϕ_i , ρ_{iv} , ρ_{ic} are respectively the pre-exponential factor, activation energy, decomposition reaction order, virgin and charred density for the component $i=A,B,C$. The necessary terms for Eq. 2.2 are empirically evaluated through thermal gravimetric analysis (TGA) [7].

2.1.2 The in-depth energy equation

The following equation describes the internal exchanges of energy in the TPS thickness.

$$\rho c_p \frac{\partial T}{\partial t} = \frac{\partial}{\partial x} \left(k \frac{\partial T}{\partial x} \right) + (h_g - \bar{h}) \frac{\partial \rho}{\partial t} + \dot{s} \rho c_p \frac{\partial T}{\partial x} + \dot{m}_g \frac{\partial h_g}{\partial x}, \quad (2.3)$$

The individual terms which form Eq. 2.3 can be interpreted as: rate of storage of sensible energy, net rate of thermal conduction, pyrolysis energy rate, convection rate of sensible energy due to coordinate system movement, and net rate of energy convected with pyrolysis gas passing a point. The thermal conduction and the pyrolysis energy rate are the only terms which are implemented in the approach used for ARC, the other two terms in Eq. 2.3 are neglected. The last section of this chapter contains several comparisons between internal temperatures simulated by ARC and the same temperatures evaluated by commercial codes; these comparisons show that the decision to neglect the convection rate of sensible energy due to coordinate system movement and the net rate of energy convected with pyrolysis gas passing a point does not lead

to significant discrepancies between ARC simulations and the expected results. That is because the effects of the neglected physical phenomena have a lower influence on the material behaviour than the processes ARC accounts for. A more in-depth explanation of Eq. 2.3 terms influence on the internal temperatures is presented in paragraph 2.4.2 where ARC results are compared to results generated using Eq. 2.3 in its entirety. The local specific heat is a function of both virgin and charred specific heat values and the local charring state; it is formulated as shown in Eq. 2.4.

$$c_p = \tau c_{pv} + (1 - \tau)c_{pc}. \quad (2.4)$$

$$\tau = \frac{\rho_v}{\rho_v - \rho_c} \left(1 - \frac{\rho_c}{\rho_i} \right) \quad (2.5)$$

where τ represents the virgin mass fraction. The thermal conductivity k is evaluated using an equivalent equation.

2.1.3 Boundary conditions

The energy balance for the ablative surface or external surface (which is indicated as T_w in the following equations and the figures) is formed by several processes as illustrated in Fig. 2.1. The equation representing this energy balance is:

$$\begin{aligned} & \rho_e u_e C_H (H_r - h_{ew}) + \rho_e u_e C_M [\Sigma(z_{ie}^* - z_{iw}^*) h_i^{T_w} - B' h_w] \\ & + \dot{m}_c h_c + \dot{m}_g h_g + \alpha_w q_{rad} - F \sigma \epsilon_w T_w^4 - q_{cond} = 0. \end{aligned} \quad (2.6)$$

Eq. 2.6 individual terms represent in order: convective flux, chemical energy rate, rate of radiant energy input to the ablating in surface, rate of radiant energy emission from the ablating out surface and rate of energy conduction into the ablating material. In the proposed approach, the chemical energy rate terms are neglected transforming Eq. 2.6 in:

$$\rho_e u_e C_h (H_r - h_{ew}) + \alpha_w q_{rad} - F \sigma \epsilon_w T_w^4 - q_{cond} = 0. \quad (2.7)$$

Neglecting the chemical energy introduces some errors in the ARC simulations; the magnitude of these errors can be appreciated in the graphs representing the comparison

between ARC evaluated T_w (external surface temperature) and the T_w calculated by commercial codes like FIAT or PATO (Fig. 2.4, Fig. 2.7, Fig. 2.11,) because both of these codes do not neglect the chemical terms in Eq. 2.6. The external surface boundary condition is:

$$\left(k \frac{\partial T}{\partial x} \right)_{x=x_w} = q_{cond}. \quad (2.8)$$

Where q_{cond} is calculated through Eq. 2.7. The internal surface is characterized by an adiabatic condition, therefore without any exchange of heat with the rest of the spacecraft. This condition is considered conservative for the applications the code was implemented for, *i.e.* ablative TPSs simulations, because the rest of the spacecraft structure is in contact with the TPS and can absorb part of the thermal energy, thus decreasing the TPS temperature. If the code was to be used for a different purposes (*e.g.* demisability analyses), this condition might not remain conservative. Eq. 2.9 illustrates the internal surface boundary condition.

$$\left(\frac{\partial T}{\partial x} \right)_{x=0} = 0. \quad (2.9)$$

2.1.4 Pyrolysis gas and char production

During the degradation, the material decreases its density and it produces pyrolysis gases. In the ARC approach, the pyrolysis gas production is treated as a succession of steady state problems; for every time step it is assumed that the entire mass loss due to degradation is transformed into gas, and that the full gas production is able to exit the material surface. Following these assumptions, the mass flow rate of the pyrolysis gas can be evaluated as follows [34]:

$$\dot{m}_g = \frac{1}{\Lambda} \int_{x_0}^{x_w} \left(\frac{\partial \rho}{\partial t} \right) \Lambda \partial x. \quad (2.10)$$

Finally, the charred material mass flux and the material recession rate are evaluated using the material B' table or table of dimensionless mass blowing rates. The B' table of a particular material contains the thermo-chemical parameters required to calculate

the material surface recession for different pyrolysis conditions. These tables present the value of the dimensionless char mass using as input the dimensionless pyrolysis gas mass, the temperature and the pressure of the material. In simpler terms, they are used to calculate the material recession from the values of temperature, pressure and pyrolysis gas mass flow rate. At first, the value of dimensionless pyrolysis gas mass blowing rate is calculated using the following equation:

$$B_g = \frac{\dot{m}_g}{\rho_e u_e C_M} \quad (2.11)$$

Then, the dimensionless char mass blowing rate is selected from the table, utilizing the dimensionless pyrolysis gas blowing rate, the temperature and the pressure as input data; afterwards, the char mass flux is determined using:

$$\dot{m}_c = B_c \rho_e u_e C_M \quad (2.12)$$

and finally the recession rate is estimated using Eq. 2.13.

$$\dot{s} = \dot{m}_c / \rho_c \quad (2.13)$$

C_M represents the Stanton number for the mass transfer. In the presented approach, it is assumed that this coefficient is equivalent to the Stanton number for the heat transfer C_H , an assumption which is often found in litteraure [29], within the boundary layer that is where Eq. 2.12 and Eq. 2.13 are applied. Tables of B' can be computationally generated using the ACE or MAT methods [34]; the B' table utilized in this work for the TACOT material was generated using Mutation [44] and the thermophysical database of CEA (Chemical Equilibrium with Applications) [45]. All of the B' tables used in this document are present in the literature and were not generated during the study herein presented.

2.1.5 Blowing correction

A blowing rate correction is introduced to take into account the blocking effect produced by the flow of the pyrolysis gases exiting the external surface [46]. The ARC program calculates a reduction of the transfer coefficient C_H according to the equations:

$$\frac{C_H}{C_{H0}} = \frac{\zeta}{e^\zeta - 1} \quad (2.14)$$

$$\zeta = \frac{2\lambda(m_g + m_c)}{\rho u_e C_{H0}} \quad (2.15)$$

where ζ is equal to 0.5 in the classical blowing correction formula [46].

2.2 Computational procedure

This section describes how the governing equations were implemented in the code, and illustrates the procedure utilized to perform a simulation. A schematic visualization of ARC's patterns and procedures is presented through Algorithm 1 and Fig. 2.2.

The governing equations were implemented using the finite difference method; this method was selected for its simplicity and speed of implementation. The equations are integrated using the `scipy` python library [47]; the integration method selected is called `vode` and it is a Real-valued Variable-coefficient Ordinary Differential Equation solver [48], with fixed-leading-coefficient implementation. Eq. 2.3 is transformed, using finite differences in:

$$\begin{aligned} \rho c_p \frac{\partial T}{\partial t} &= \frac{k_{i-1}^n - k_{i+1}^n}{2\Delta x} \frac{T_{i-1}^n - T_{i+1}^n}{2\Delta x} \\ &+ k_i \frac{T_{i-1}^n - 2T_i^n + T_{i+1}^n}{\Delta x^2} + A_i \left(\frac{\rho_i - \rho_{ic}}{\rho_{iv} - \rho_{ic}} \right)^{\phi_i} e^{-E_i/T_i^n} \end{aligned} \quad (2.16)$$

Then,

$$\begin{aligned} \frac{\partial T}{\partial t} = & \frac{1}{\rho_i c_{Pi}} \left(\frac{k_{i-1}^n + 4k_i^n - k_{i+1}^n}{4\Delta x^2} T_{i-1}^n - 2 \frac{k_i^n}{\Delta x^2} T_i^n \right. \\ & \left. + \frac{-k_{i-1}^n + 4k_i^n + k_{i+1}^n}{4\Delta x^2} T_{i-1}^n + A_i \left(\frac{\rho_i - \rho_{ic}}{\rho_{iv} - \rho_{ic}} \right)^{\phi_i} e^{-E_i/T_i^n} \right) \end{aligned} \quad (2.17)$$

In the first time step of the simulation, all the nodes of the grid are characterized by the same initial temperature and material density equivalent to the virgin state one. The thermal conductivity and the specific heat for the virgin material are calculated for the initial temperature and assigned to every node (line 1 to 4 in Algorithm 1); after this procedure is complete, the simulation can begin. At the start of every time step, the program retrieves the nodal density and temperature values calculated in the previous time step. Once these characteristics are known, the code calculates the new values of thermal conductivity and specific heat using as inputs the density and the temperature of the specific node (Eq. 2.4); then, using Eq. 2.2, it assesses the changes in density for the current time step (line 5 to 15 in the Algorithm 1). Later, the code determines the conductive heat flux using Eq. 2.3 and evaluates the changes of temperature introduced along the material depth by the heat flux values using Eq. 2.7 (line 16 to 19 in Algorithm 1). If the material B' table is available, the code also calculates the char mass flux and the recession rate (line 20), otherwise this operation is skipped; the recession rate calculated at the end of one time step is implemented in the successive time step. Introducing the recession in the simulation is important because it has a non-negligible impact on the simulations; this is shown in the following section of this chapter, however, it has to be handled with care because it introduces a change in the geometry and in the node positions. At the end of every time step, the new values of temperature and density are calculated and stored for the following time step (line 22 to 27 in Algorithm 1).

Different programs use different methods to simulate the recession of the material; in the CMA code [46] the internal nodal points are kept fixed in space while the external point is moved towards the internal surface, decreasing the last node length until the

```

input: N: number of nodes, L: thickness, deltat: time step, tf: final time,
        ablator characteristics, heat flux trend
1 initialization;
2 /* initialize the density and temperature vectors */)
3 density vector: size=N, each node= virgin  $\rho$ 
4 temperature vector: size=N, initial temperatures
5 Main Body;
6 while time <= tf do
7   new L
8   /* implement the recession calculated at previous deltat */
9   for i=0 to N do
10    /* updates the thermal characteristics values */
11    specific heat value for node i
12    thermal conductivity value for node i
13    /* density derivative */
14    total density derivative of node i [Eq. 2.1]
15  end
16  for i=0 to N do
17    /* temperature derivative */
18    temperature derivative of node i [Eq. 2.3]
19  end
20  derivative of recession
21  return derivatives of total density and temperature for each node
22 integrate equation system (using calculated derivatives)
23 for i=0 to N do
24  /* density and temperature values for successive time step */
25  /* */
26  density value of node i for time+deltat
27  temperature value of node i for time+deltat
28 end
end

```

Algorithm 1: Algorithmic form of the one dimensional version of ARC.

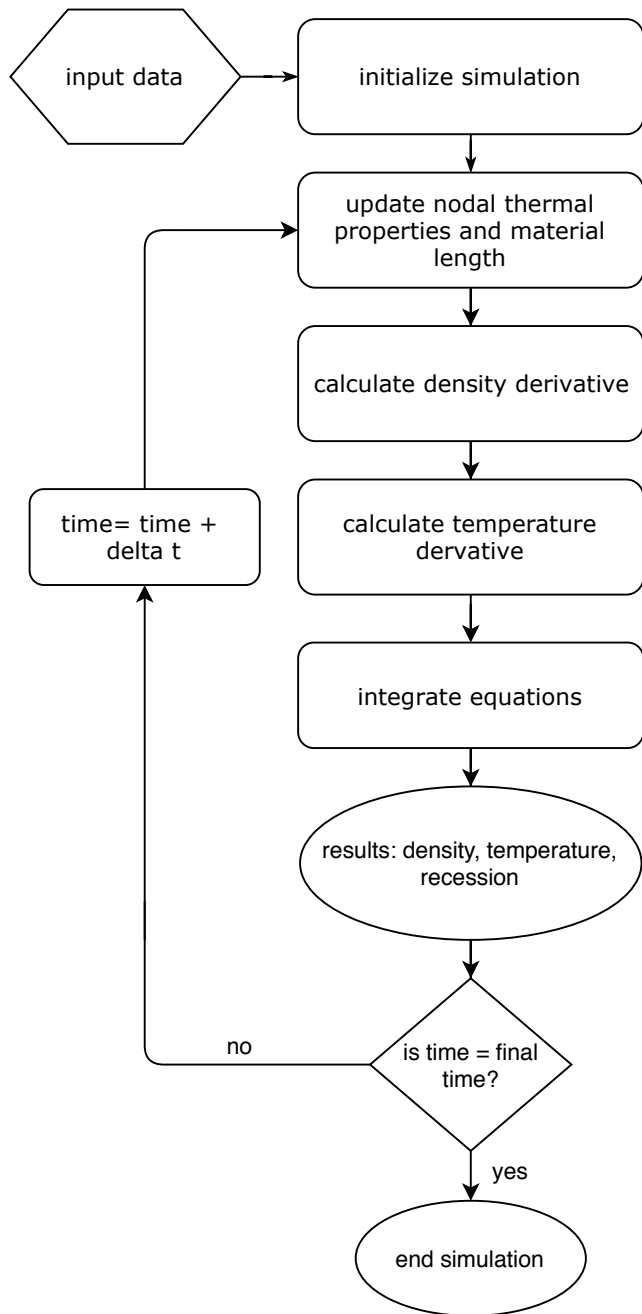


Figure 2.2: Flow chart describing the one dimensional version of the ARC code.

external point corresponds to the previous point. When the two points have the same coordinates, the last one is discarded, and the number of nodes is reduced by one. In the ARC code the number of points is kept fixed while their position in space changes. At the end of every time step the new material thickness is determined, it is divided by the fixed number of points and the new grid is created. Before the beginning of the new time step the temperatures and densities for the new nodal points are calculated by interpolating the values of these characteristics in the previous nodal points. This procedure might appear to be overcomplicated and unnecessary, however it has the advantage of keeping constant the distance between adjacent nodal points in the same time step and of avoiding the creation of very small nodal distances which would affect the calculations. This side effect could also be avoided introducing a minimum distance between the last and the second to last point; when this distance is reached the last point is eliminated. This methodology is valid and used in other codes, but it introduces higher than necessary jumps in the ablator thickness between consecutive time steps and small deviations from the actual recession happening. For these reasons, it was decided to use a fixed number of points for the grid. It is important to say that the two methodologies seem to be equivalent, and that the choice of which one to use is based on the coder's preference.

2.3 Material model

One very influential input required by ARC, is the model of the material containing the physical, chemical and thermal properties of the ablator to be analysed. This model is generated empirically through extensive testing of the material by the company which produces the ablator or the agency which wants to use it. Different experimental procedures are used to perform the material characterization such as Thermo-Gravimetric Analyses (TGA) and Differential Scanning Calorimetry (DSC) or a simultaneous combination of the two for a larger data collection [49]. Furthermore, some of these models are validated through the comparison between simulations of the TPS behaviour performed using the material model and plasma tests results. Consequently, accurate

models are quite expensive; for this reason, in some cases, the characterization is only partially performed or, when completed, it is not released in literature. ARC needs the following characteristics in order to perform all the estimates it is capable of calculating:

- Arrhenius equation terms: pre-exponential factor, activation energy, decomposition reaction order, which are used in the decomposition model;
- Virgin and charred state density, which are utilized to evaluate the char mass fraction during the pyrolysis and influence the heat conduction;
- Virgin and charred state thermal conductivity as a function of temperature, which influence the heat transfer in the material;
- Virgin and charred state specific heat as a function of temperature, which influence the temperature gradient in the material;
- Enthalpy of formation and pyrolysis, which describe the energy necessary to complete these processes.

For some of the materials used in the following simulations, it was possible to find a complete model in literature, for others it was not. In the latter case, the model was generated using available data from similar materials. The accuracy of the thermo-physical properties of the ablator greatly influences the precision of the results produced by simulations. The study of the errors introduced in the ARC simulations by the uncertainty in the material characterization could be interesting to better understand ARC results. Unfortunately, it was not possible to find in literature any information regarding the models accuracy nor precision, therefore this type of analyses was not performed. During the collection of the data for the various material models, it became clear that some properties are usually better analysed than others. For this reason, it was decided to produce a more detailed study on one of these properties, the permeability. The activities performed to complete this task are presented in chapter 5.

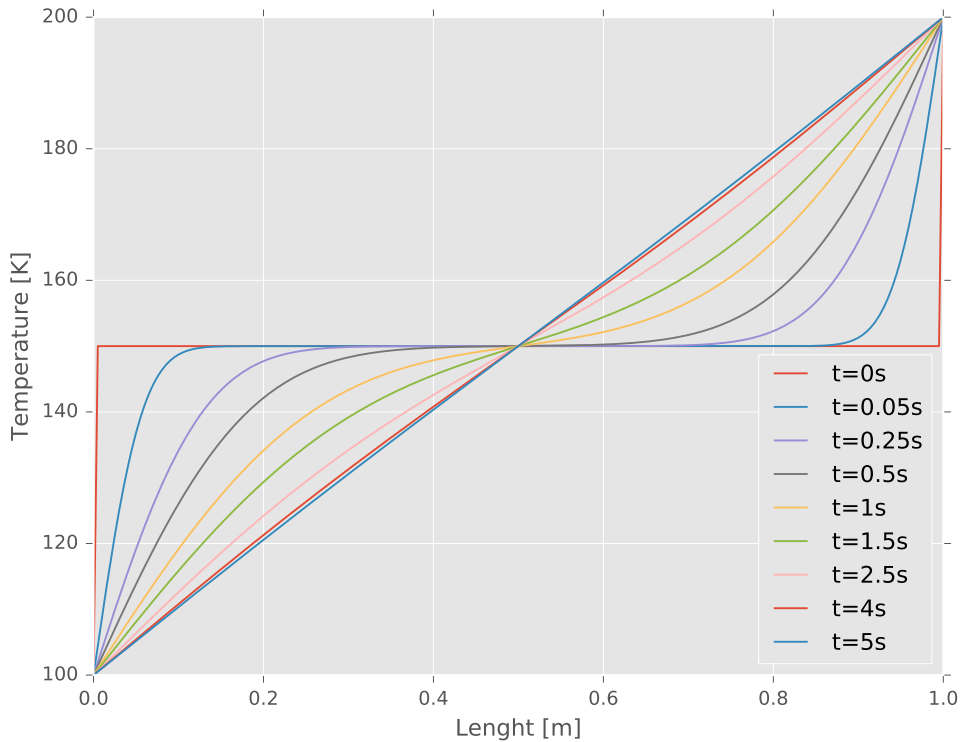


Figure 2.3: Temperature trends at different times for the one-dimensional heat transfer case.

2.4 Code verification

This section of the thesis describes the verifications performed on the one-dimensional code. The first paragraph illustrates the ability of the code to solve simple conduction cases. The following subsections describe the results obtained using ARC in a number of distinct test cases and their comparison to other one-dimensional code evaluations.

2.4.1 Simple heat transfer case

Computing such a simple case can appear meaningless since there is no ablation involved; nevertheless, the code has to be able to solve a trivial thermal conduction case to be able to fully simulate the ablation process. Moreover, this example was herein presented to ensure that the errors contained in the following cases are not caused by

any problems in the implementation of the thermal conduction. The equation for heat transfer is:

$$\frac{\partial T}{\partial t} = k \frac{\partial^2 T}{\partial x^2} \quad (2.18)$$

where:

$$\alpha = \frac{k}{\rho c_P} \quad (2.19)$$

This simulation studies the transient behaviour of a rod at constant temperature of 150 K which extremities are kept at different temperatures, equal to 100 K and 200 K. The rod length is assumed to be equal to 1 m. The thermal diffusivity α is assumed to have a constant value of 0.02 m²/s therefore, the material model for this simulation has constant density, thermal conductivity and specific heat respectively equal to 10 kg/m³, 2 W/mK and 10 J/KgK. To avoid the degradation of the material, the pre-exponential factor for all of material components is fixed to a null value.

ARC's ability to simulate the heat transfer in a one-dimensional case is shown by the trends reported in Fig. 2.3 which perfectly correspond to the analytical solutions of the heat equation for the selected time instances.

2.4.2 TACOT

Theoretical Ablative Composite for Open Testing (TACOT) is, as the name suggests, not a real material but a theoretical one. Its characteristics are known and are not subjected to empirical test uncertainties; it was created to be used as a benchmark for ablative simulation tools. In the 5th *Ablation Workshop, Feb. 28th Mar. 1st 2012, Lexington, Kentucky* [50], three test cases based on the TACOT material behaviour in different conditions were presented. In all of the cases a one-dimensional geometry is

Table 2.1: Summary of the environment properties for the TACOT test cases presented at 5th *Ablation Workshop, Feb. 28th Mar. 1st 2012, Lexington, Kentucky* [50].

| Test case [s] | $\rho_e u_e C_H$ [kgm ⁻² s ⁻¹] | h_e [Jkg ⁻¹] | p_w [Pa] |
|---------------|---|----------------------------|------------|
| 2_1 | 0.3 | 1.5x10 ⁶ | 101325 |
| 2_2 | 0.3 | 1.5x10 ⁶ | 101325 |
| 2_3 | 0.3 | 2.5x10 ⁷ | 101325 |

Table 2.2: Thermocouple positions for the test cases presented at *5th Ablation Workshop, Feb. 28th Mar. 1st 2012, Lexington, Kentucky* [50].

| TC number | position from initial external surface,m |
|-----------|--|
| Tw | current external surface |
| TC2 | 0.001 |
| TC3 | 0.002 |
| TC4 | 0.004 |
| TC5 | 0.008 |
| TC6 | 0.012 |
| TC7 | 0.016 |
| TC8 | 0.024 |
| TC9 | 0.05 |

heated on one side for one minute and then left to cool for the following minute; at the beginning of the simulation, the total thickness of the geometry is 5 cm. The external surface, the one on which the heat flux is applied, is characterized by a convective boundary condition while the internal one is characterized by an adiabatic boundary condition. The external pressure is assumed to be 1 atm for the entire time of the tests. The material thickness contains 9 different thermocouples which are used as control points for the temperature comparisons. The ARC simulations are compared with the simulation presented during the workshop by ASTRIUM [51], performed with the Amaryllis [52] and the PATO [36] codes, and by NASA Dryden Flight Research Center [53], performed with the CMA [46] and the FIAT [54] codes.

Test Case 2_1

The first test case is characterized by a low heating and a fixed recession equal to zero. This test was designed to investigate the reliability of the code in simulating the ablation processes which are not linked to the material recession. Fig. 2.4 shows the temperature trend for the internal, TC9, and the external surface, T_w . There is a good agreement with the PATO code for both faces while the FIAT code produces higher results. Fig. 2.5 contains the temperature trends for the internal thermocouples positions. The temperatures trends illustrated in Fig. 2.5 are plotted as if the data was collected by real thermocouples; this means that the TC position is fixed in the material

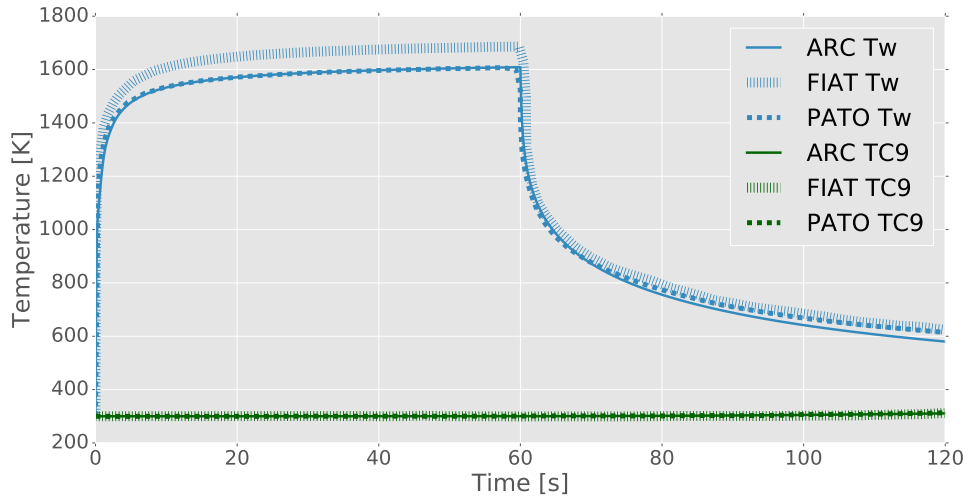


Figure 2.4: Test case 2_1 comparison between FIAT, PATO and ARC temperature estimates for the two TPS boundary surfaces: the external, Tw, and the internal, TC9, surface.

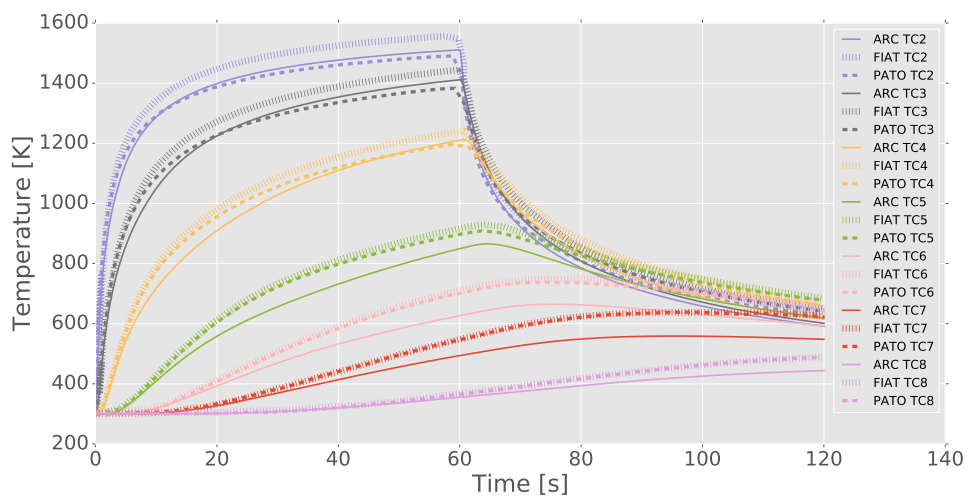


Figure 2.5: Test case 2_1 comparison between FIAT, PATO and ARC temperature estimates in various points inside the TPS thickness. The point locations are contained in Table 2.2.

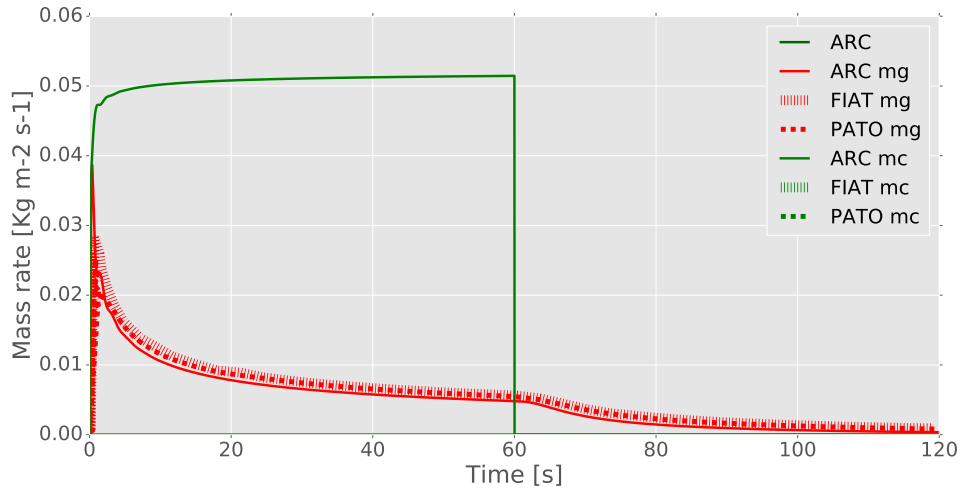


Figure 2.6: Test case 2_1 comparison between FIAT, PATO and ARC pyrolysis gas mass ow rate, \dot{m}_g , and char gas mass flow rate, \dot{m}_c .

thickness, therefore the TC distance from the internal surface remains constant while its distance from the external wall changes due to the recession. This same method is used for every graph representing internal temperature trends included in this thesis. The ARC tool produces results which do not perfectly correspond to the FIAT nor the PATO simulations but they have very similar trends in comparison to both codes; moreover, the differences between the ARC generated temperature and the PATO/ FIAT ones are comparable to the difference between the PATO and FIAT results. The pyrolysis gas mass rate is illustrated in Fig. 2.6; it shows a very good agreement among the three codes. The ARC results are slightly lower than those of the other two, this discrepancy is due to the neglected terms in both Eq. 2.3 and Eq. 2.6 because both of them influence the parameters used for the pyrolysis gas production evaluation.

Test Case 2_2

Test case 2_2 has the same heat flux and external pressure as the previous case, however it has a positive recession rate. This case was designed to evaluate if the code is able to reproduce the ablation processes which are a function or a consequence of the material recession. These processes have a non-negligible role in the energy balance

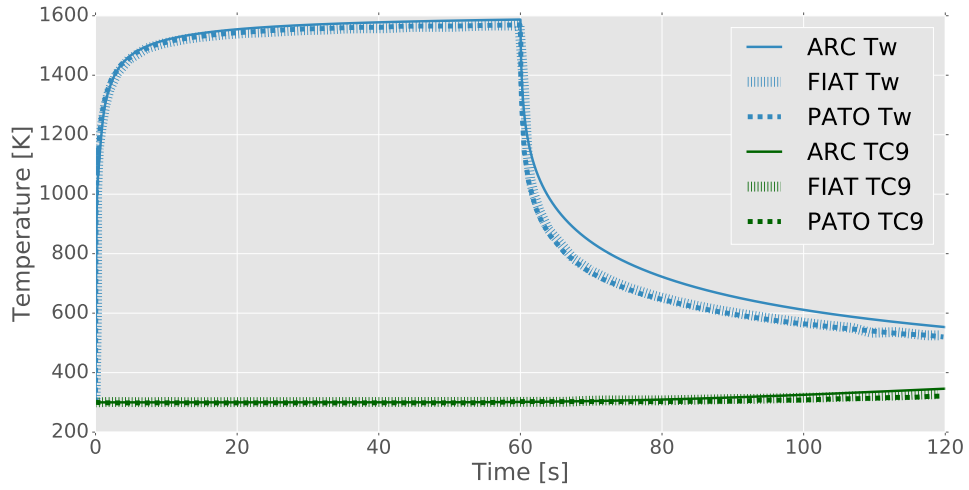


Figure 2.7: Test case 2_2 comparison between FIAT, PATO and ARC temperature estimates for the two TPS boundary surfaces: the external, Tw, and the internal, TC9, surface.

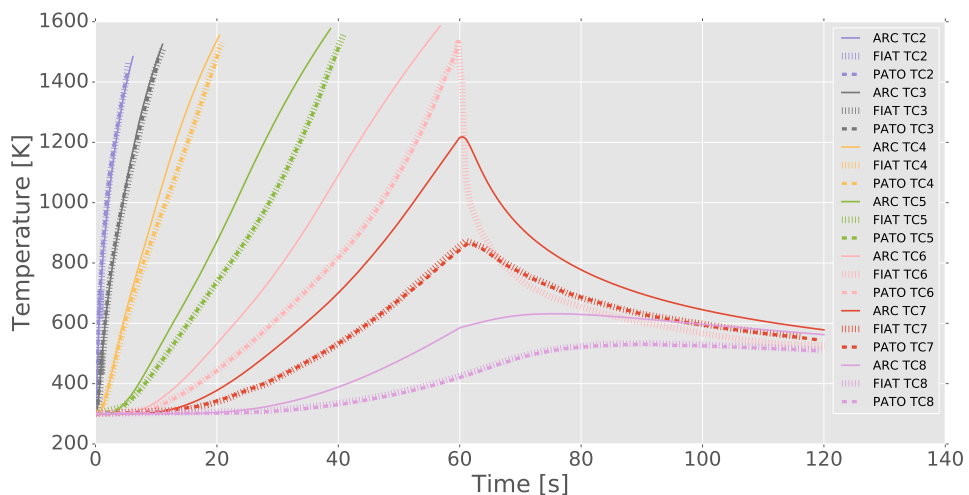


Figure 2.8: Test case 2_2 comparison between FIAT, PATO and ARC temperature estimates in various points inside the TPS thickness. The point locations are contained in Table 2.2.

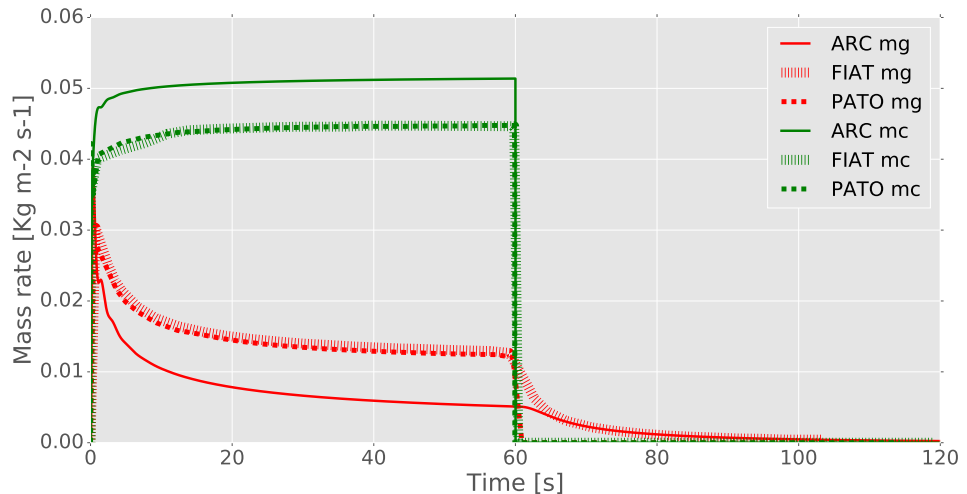


Figure 2.9: Test case 2_2 comparison between FIAT, PATO and ARC pyrolysis gas mass flow rate, \dot{m}_g , and char gas mass flow rate, \dot{m}_c .

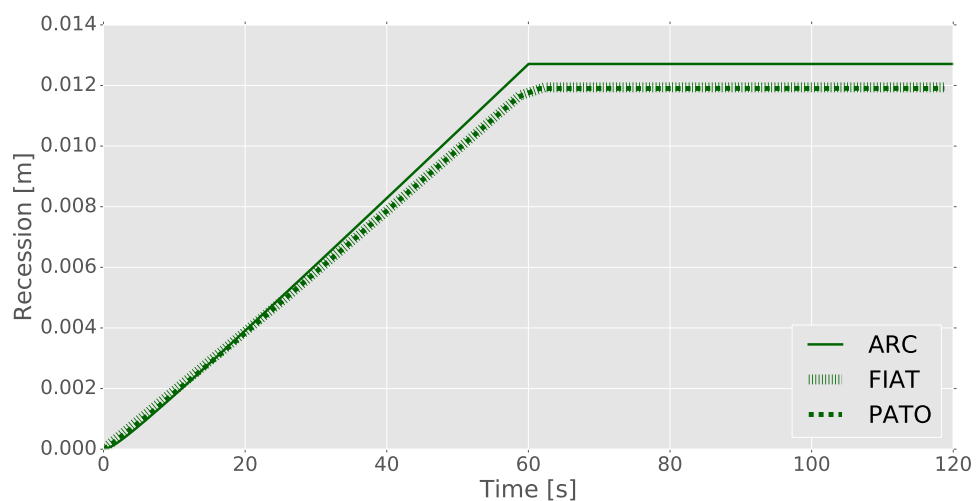


Figure 2.10: Test case 2_2 comparison between CMA/FIAT and ARC evaluation of the recession occurred during the simulation illustrated as a function of time.

inside the material, as it is indicated by the differences in wall temperature trend and pyrolysis gas flux between this test case and the previous one. These changes can be appreciated comparing Fig. 2.4 with Fig. 2.7 and Fig. 2.5 with Fig. 2.8. Fig. 2.7 shows a good agreement between the ARC temperatures and the PATO and FIAT results; the ARC temperatures show a slower decrease during the cooling phase but a very good agreement during the heating part of the simulation for the external temperature. This difference is explained by the fact that the ARC code neglects the chemical terms in Eq. 2.6 while both commercial codes implement Eq. 2.6 in its entirety. During the heating phase these terms have a smaller role in the energy balance because the heating flux is very high; during the cooling phase the external heat flux is equal to zero and small terms have higher effects. This was not considered to be a problem because the maximum error generated by ARC happens during the cooling phase, which is less demanding for the ablator. The heating portion is the most critical in the TPS design because it is the section in which the TPS must perform its protective task. Therefore, it is the part studied when designing the TPS. In this phase the difference between ARC and the two commercial codes are comparable to the differences between the two commercial programs. In addition, the ARC simulated external and internal temperatures are above the FIAT and PATO values therefore they are considered conservative when simulating TPSs. Conservative results are preferred in TPSs design because they provide an additional margin of error and a lower probability of failure of the system. In addition, it is important to point out that the three-dimensional cases, which are presented in a following chapter and represent the type of simulations ARC was implemented for, are actively heated for the their entire duration, therefore they are performed, as it can be seen from the Fig. 2.4, 2.5, 2.7, 2.8, where the code has its maximum precision.

Fig. 2.8 shows the internal temperature trends and their comparisons to the other two codes. The ARC generated temperatures are in small disagreement with the FIAT or PATO trends especially for the thermocouples which are located near the middle of the ablative material thickness. The overestimations of these temperatures are caused by different effects. The material recesses slightly more in the ARC simulation than

in the FIAT or PATO ones as shown in Fig. 2.10; in the second part of the heating phase, when this difference becomes notable on the graphs, the internal thermocouples, in the ARC simulation, are closer to the external surfaces and more influenced by its elevated temperature. Moreover, the internal surface temperature is calculated using Eq. 2.3 in which some terms have been neglected. These terms are more relevant when the temperature gradient is less steep, and the thermal conduction is characterized by smaller values. At temperatures lower than the temperature of pyrolysis reaction, those terms are actually equal to zero because the pyrolysis phenomenon is not active yet; for this reason, the thermocouples close to the internal surface present lower discrepancies. The ARC values of pyrolysis and char mass fluxes, Fig. 2.9, show higher discrepancies, when compared with commercial codes results, than the values calculated for the previous test case and illustrated in Fig. 2.6. The differences in the results are due to two cause: the assumption used in Eq. 2.10 and the different methods implemented for the use of the B' tables. Given the B' tables input and output, there are a great variety of methodologies which can be used to produce the required results. Unfortunately, it was not possible to find in literature the exact method implemented by either of the commercial codes, therefore a more precise comparison is not possible. Additionally, pyrolysis and char mass flows are not directly used for the TPS sizing, but they are employed for the evaluation of the material recession whose trend is shown in Fig. 2.10. The maximum difference between ARC and FIAT/PATO values is of 0.8mm for a total recession of 12mm for the codes used for this validation. This means that the ARC evaluated final ablator thickness is equal to 37.2 mm instead of the 38 mm calculated by both commercial programs. This discrepancy can be neglected because such a small difference (around 2%) cannot introduce any consequential change in the structural behaviour of the TPS.

Test Case 2_3

As shown in Table 2.1, test case 2_3 is characterized by a high heating rate and a non-zero recession. This case is used to study the code response to higher heat fluxes and its behaviour in comparison to the lower flux cases. The material temperatures,

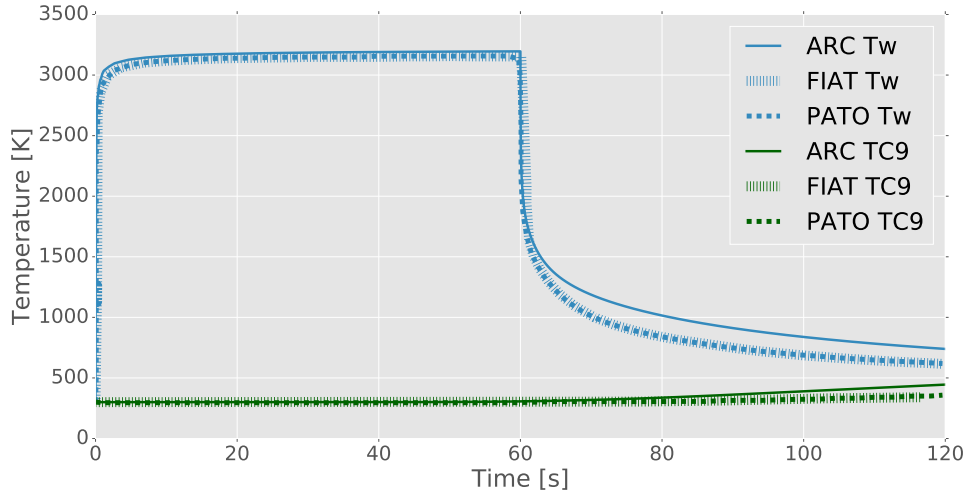


Figure 2.11: Test case 2_3 comparison between FIAT, PATO and ARC temperature estimates for the two TPS boundary surfaces: the external, Tw, and the internal, TC9, surface.

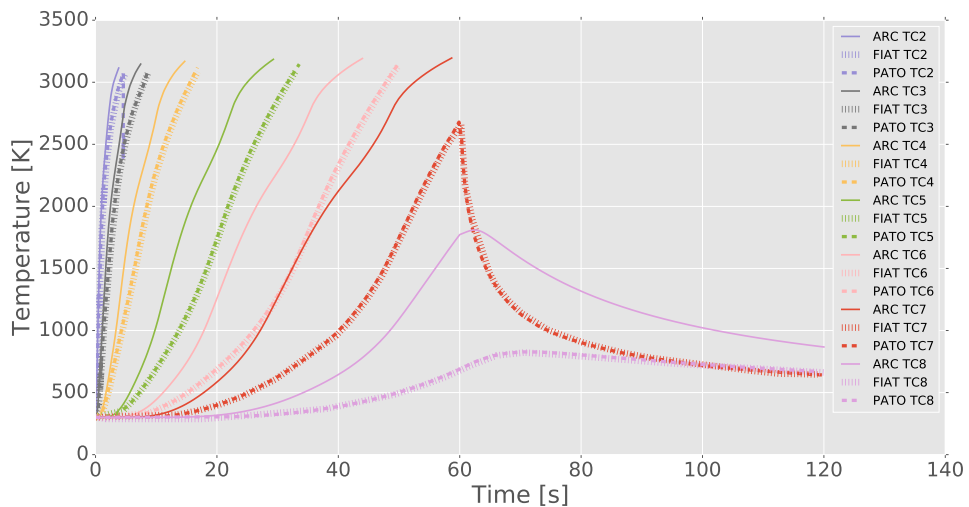


Figure 2.12: Test case 2_3 comparison between FIAT, PATO and ARC temperature estimates in various points inside the TPS thickness. The point locations are contained in Table 2.2.

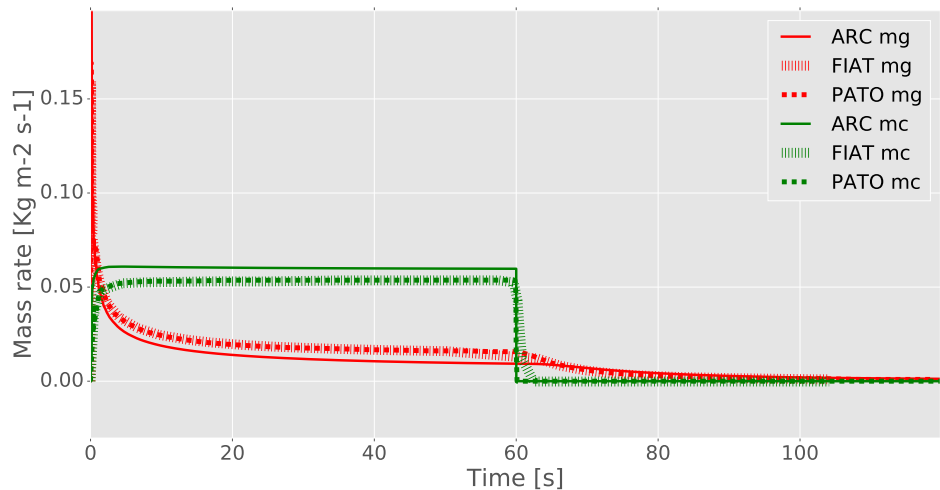


Figure 2.13: Test case 2_3 comparison between FIAT, PATO and ARC pyrolysis gas mass ow rate, \dot{m}_g , and char gas mass ow rate, \dot{m}_c .

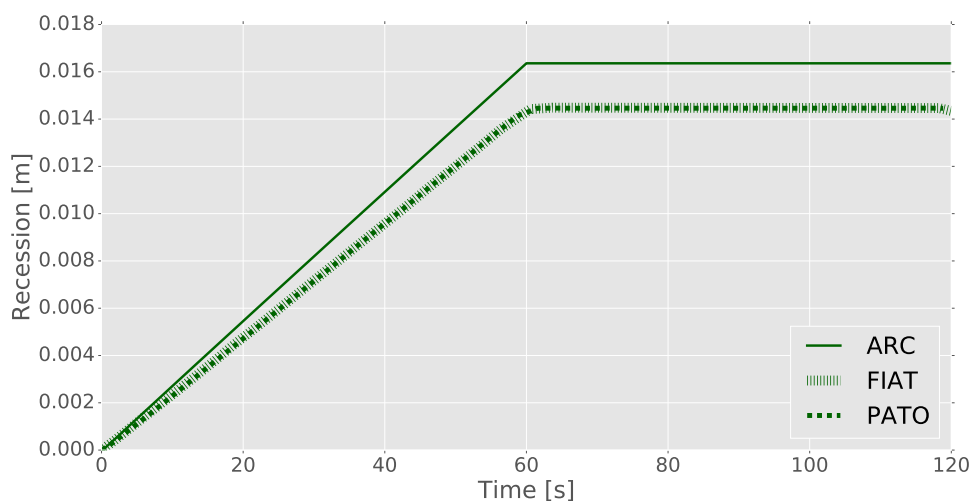


Figure 2.14: Test case 2_3 comparison between CMA/FIAT and ARC evaluation of the recession occurred during the simulation illustrated as a function of time.

Fig. 2.11 and Fig. 2.12, present similar discrepancies than the one encountered in the former case. As explained in the previous paragraph, this error is due to the terms which were neglected during the implementation of the governing equations (Eq. 2.6 for the values illustrated in Fig. 2.11 and Eq. 2.3 for the temperature trends in Fig. 2.12) and the more elevated recession simulated by ARC, which has a higher influence for the internal temperature trends in Fig. 2.12. In this case the absolute errors have a slight increase in comparison to the previous cases as a result of a higher importance of the neglected terms in the high heating circumstances. However, the maximum error is also encountered in the cooling phase which is not used for the TPS design nor for the simulations of real case entries proposed in chapter 4. Moreover, both the temperature and the recession values present conservative trends which are preferred for the type of analyses ARC was implemented for. Fig. 2.13 shows good agreement for the values of gas and char production while Fig. 2.14 illustrates the discrepancy among the simulated recessions; for this test case the ARC recession is equal to 16.35mm while it is 14.45mm for FIAT and 14.34mm for PATO.

2.4.3 PICA

Phenolic Impregnated Carbon Ablator (PICA) [10] is one of the best known ablative materials and it has been successfully used for decades. Since its development, it has withstood a multitude of re-formulations to improve its properties or make it more effective for a specific mission. Unfortunately, the thermal characteristics of PICA, which have to be empirically evaluated through tests because it is an actual material, are less precise and more inclined to uncertainties due to the tests utilized to measure them. The PICA material exists in a great variety of different versions which have different

Table 2.3: Thermocouple positions as described by Mansour *et al* [35].

| TC number | position from the internal surface,m |
|-----------|--------------------------------------|
| Tw | current external surface |
| TC2 | 0.02246 |
| TC3 | 0.01992 |
| TC4 | 0.01484 |
| TC5 | 0.0 |

thermal characteristics. The existence of different types of PICA and the difficulty to encounter detailed lists of any commercial material properties are the reasons why, slightly higher discrepancies are to be expected when performing simulations with PICA or with any other real material. In addition, to the author's knowledge, a dedicated B' table for the desired version of PICA material is not present in literature therefore it was decided to use the TACOT B' table for all the PICA simulations. The error introduced by this decision is expected to be negligible due to the similarities between the TACOT and PICA materials.

The simulation selected for this verification is the same as that performed by Mansour *et al* [35] using both the CAT and the FIAT code; this test case is similar to the previous TACOT cases. It is characterized by a constant heat flux for a fixed time duration and a following cooling phase with external heat flux set to zero and, the constant heat flux is equal to 300 W/cm^2 . The total thickness of the geometry at the beginning of the simulation is 2.5cm ; Table 2.3 indicates where temperature checking points (referred as thermocouples for simplicity) are located. Unfortunately, the paper reporting this taste case does not contain the heat transfer coefficient used to perform the simulation; the heat transfer coefficient is used in Eq. 2.11 and in Eq. 2.12 to determine the char mass flux from the pyrolysis mass flux. Initially, the same value of the TACOT test cases presented in the previous section of this chapter was selected. To ensure that the chosen value for this coefficient was appropriate, Eq. 2.11 and Eq. 2.12 were used to calculate the char mass fraction using the paper results for temperature and pyrolysis gas, and the selected heat transfer coefficient to ensure that all of the inputs for the simulations were consistent with the ones used in the paper. The results show a good agreement between the char mass flux presented in the paper and the values of the same flux calculated with the selected heat transfer coefficient; the agreement was especially good with the FIAT code: the char mass flux calculated with the selected heat transfer coefficient, and the one evaluated with FIAT presented close to no discrepancies for the entire duration of the simulation. When the discrepancies were not equal to zero, they were lower than the differences between FIAT and CAT, the two commercial codes. Furthermore, the paper does not specify

the thermal properties that were utilized to perform the simulation, nor the version of the PICA material used. As previously stated, the publicly available data regarding the PICA properties is limited, therefore it was decided to firstly perform this simulation using the TACOT material. PICA and TACOT have very similar characteristics, the theoretical material was heavily based on this particular existing ablator, thus, it was expected to have a good agreement with the paper results using the latter instead of the former. Afterwards, the same simulation was performed using a PICA model generated especially for this study. The model was obtained combining a number of incomplete different models present in literature, in addition with the TACOT B' table; the simulation performed with the TACOT material was fundamental for the selection of the PICA thermal characteristics.

Fig. 2.15 represents the temperature trends for the various points in the material thickness as calculated by ARC, CMA and FIAT. The temperatures at the boundary surfaces and for the internal thermocouples show a very good agreement with the ARC and FIAT results for the TACOT material simulation. The discrepancies between ARC results and the commercial codes values are comparable to the difference between the two commercial codes for the more external temperatures. A similar trend characterizes the more internal temperatures. This is excellent because T_w is very important when simulating an ablative TPS, since it usually represents the maximum temperature the ablator will encounter. At the same time, the internal temperature is also essential because it is the parameter used to decide the TPS thickness. Fig. 2.16 illustrates the estimated mass flux of pyrolysis gas and char; they also are in agreement with the other codes simulations. The paper used for this comparison does not report the recession trend, but only the final recession value; this value is equal to 8.24mm for the FIAT code and 7.56mm for the CAT code while the ARC estimated recession using the TACOT material is 7.02mm . The difference between CAT and ARC recession is lower than the difference between the two commercial codes results. ARC recession is the lowest of the three programs and it could be non-conservative. This was not considered a problem because this simulation was performed with TACOT instead of the real material. The recession calculated with the PICA model is 7.85 mm , higher

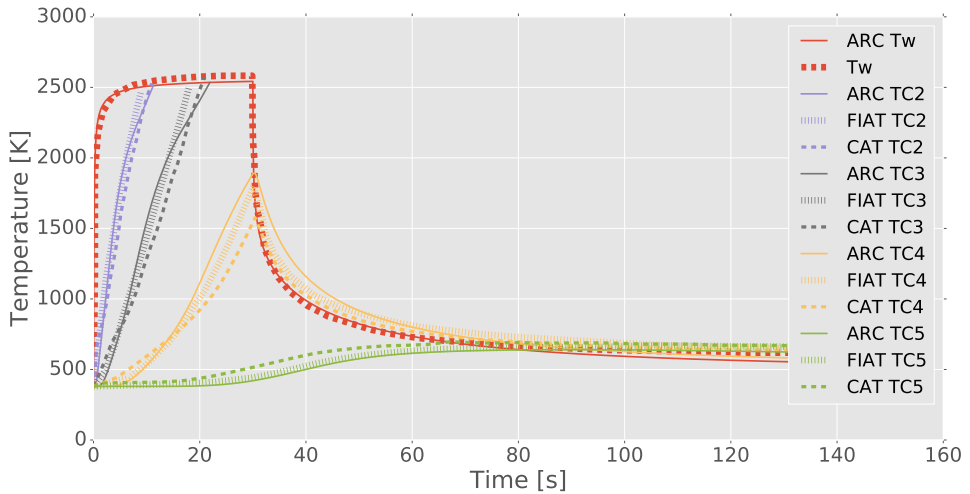


Figure 2.15: Comparison between CMA, FIAT and ARC estimation of temperatures in various points inside the TPS thickness for the Mansour *et al* [35] test case performed using the TACOT material.

than the CAT value. If both commercial codes values are considered accurate enough for this simulation, a result which sits between those values must also be regarded as correct enough.

Fig. 2.16 and Fig. 2.17 illustrate the same temperatures and mass flux results but generated with the PICA model instead of the TACOT one. As expected, the results performed with the PICA material have greater discrepancies in comparison with the paper results. The internal temperatures have higher values; in particular TC5 shows a large increase in the temperature trend. This can be caused by a higher recession than before, in this simulation the total recession is equal to 7.85mm , this means that for part of the simulation TC5 position is closer to the external surface therefore more influenced by its high temperature. Another important factor could be a higher thermal conduction for the PICA model compared with the TACOT model, this difference would mean that the PICA has lower insulating power than the TACOT material causing a more elevated increase in the internal temperatures for the PICA simulation.

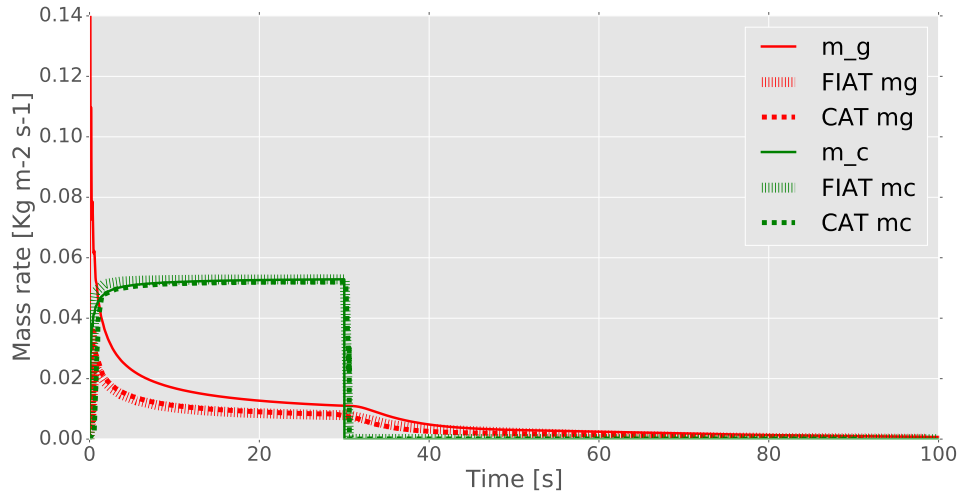


Figure 2.16: Comparison between CMA, FIAT and ARC pyrolysis gas mass flux, m_g , and char mass flux, m_c , for the Mansour *et al* [35] test case performed using the TACOT material.

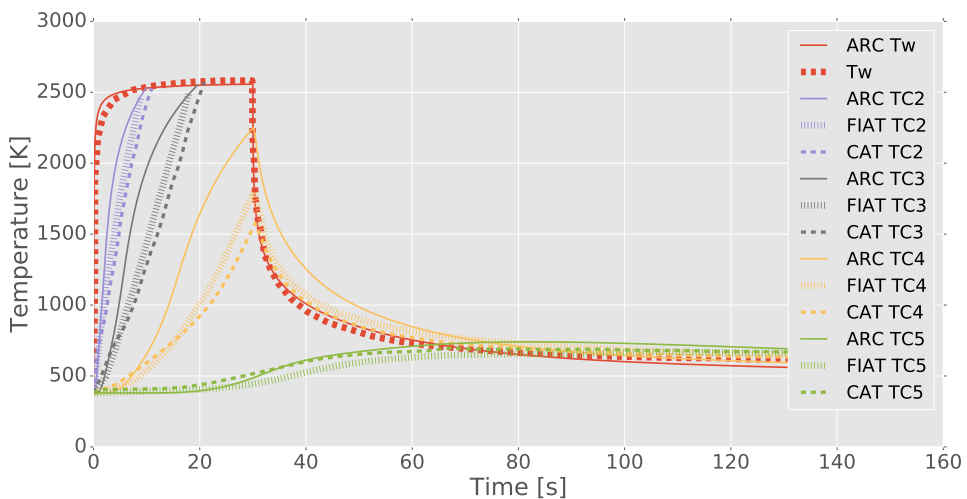


Figure 2.17: Comparison between CMA, FIAT and ARC estimation of temperatures in various points inside the TPS thickness for the Mansour *et al* [35] test case performed using the PICA material.

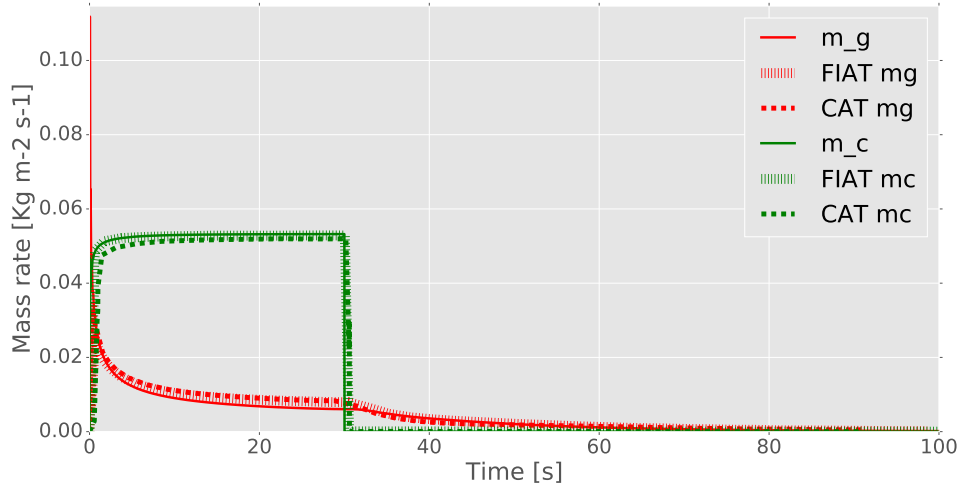


Figure 2.18: Comparison between CMA, FIAT and ARC pyrolysis gas mass flux, m_g , and char mass flux, m_c , for the Mansour *et al* [35] test case performed using the PICA material.

2.5 Discussion

This chapter shows that the results produced by the one-dimensional version of the ARC code are comparable to the results obtained with commercial program such as FIAT, PATO and CAT. These commercial codes are considered accurate enough to be used in final phases of the TPS design (e.g. FIAT has been the tool of choice for a great variety of NASAs missions such as Stardust [55] or Mars pathfinder [32]). The figures proposed in this chapter show that the differences between the ARC calculated values and the values estimated by the commercial codes are comparable to the discrepancies between the two commercial codes during the actively heated phases of the simulation. If all of the commercial programs used for the comparisons are considered accurate enough for the final phases of the TPS design, ARC, which produces results characterised by a similar accuracy, can be considered to produce good enough results for the preliminary phases of design activity. ARC results are not all characterized by the same accuracy, but an increased error is generated when the simulation characteristics violate the assumptions used while implementing the code. Specifically, ARC results are not considered accurate enough during the cooling phases of the simulation.

Chapter 2. One-dimensional ablative response code

This must be taken into account when using the code. However, ARC results have always been conservative for those values which are actively used for the TPS design such as the temperature of the internal surface and the recession. In conclusion, it can be said that the one-dimensional ARC code can be applied in the three-dimensional cases expecting reasonable results because these simulations are performed in situation which do not violate the assumptions used for the implementation.

Chapter 3

Aero-thermodynamic Models and Code Coupling

This chapter describes how the ARC program is coupled with an aerodynamic code to produce three-dimensional evaluations of a spacecraft atmospheric entry. The first part of the chapter focuses on the description of the two aerodynamic codes used to produce the results presented in the following chapter. The second part analyses how the coupling is performed, which data is passed from one code to another, and how it is possible to generate three-dimensional evaluations using a one-dimensional program such as ARC.

3.1 Aero-thermodynamic Model: HyFlow

In heat shield analyses, it is common for the material response codes to be used in combination with an aero-thermodynamic program to fully capture the chemical, thermal and physical interactions between the TPS and the external air surrounding the spacecraft, and how those influence each other. CFD solvers are the most commonly used tools to perform this task [26]. The aim of this work is to develop engineering type calculations for the preliminary phases of the mission design. These phases do not require the very high level of precision that could be generated by high fidelity codes such as CFD solvers. For this reason, HyFlow [56], an in-house reduced order code,

Table 3.1: Parameters describing the external gases surrounding the spacecraft in different simulation environments: ratio of specific heats, specific heat at constant pressure [J/kgK], gas constant [J/kgK] and Prandtl number.

| Parameter | Earth | Mars |
|-----------|-------|------|
| γ | 1.4 | 1.33 |
| c_{pv} | 1009 | 730 |
| R | 287 | 192 |
| Pr | 0.7 | 1 |

was the first code selected for the coupling. This program uses simplified equations and analogies to perform aero-thermal predictions of the flux surrounding a spacecraft during hypersonic flight. Both high altitudes, with free-molecular flow conditions, and lower altitudes, characterized by a continuum flow, can be estimated by this solver. All of the simulations are performed under the assumption of thermally and calorically perfect gas.

HyFlow was initially developed to perform generic aerodynamic studies of spacecraft flying inside the Earth's atmosphere; the program was not focused on thermal analyses and this capability was introduced at a later time. Nevertheless, the code can produce realistic evaluations of the external heat flux for a multitude of entry cases. The input data needed to run the simulations are: the Mach number, the air pressure and the air temperature values for a number of points during the entry trajectory; a meshed spacecraft geometry is also required. HyFlow was implemented for Earth hypersonic simulations. However, with the adjustment of some parameters, it can perform studies on any atmosphere or on particular ground test conditions. The characteristics that describe the planetary atmosphere, which must be changed, in accordance with the planet to be simulated, are illustrated in Table 3.1. HyFlow is employed to compute two values on each of the geometry panels: the heat flux and the heat transfer coefficient. The next sections describe the methodologies applied by this code to compute these values.

3.1.1 Heat Flux

The flat plate reference temperature method for evaluating the skin friction is used to generate the heat flux predictions. It adopts the Reynolds analogy which is based on the similarity between friction and heating mechanisms [57]. The heating rate can be written as:

$$q_{conv,y} = \rho_e u_e C_H (H_{aw,y} - H_w) \quad (3.1)$$

where $H_{aw,y}$ is the adiabatic wall enthalpy and H_w is the fluid enthalpy at the wall. The Stanton Number, C_H , is calculated through the Reynolds analogy:

$$C_H = \frac{1}{2} C_{f,y} F_{RA} \quad (3.2)$$

where F_{RA} is the Reynolds analogy factor estimated as a function of Pr^* , the local Prandtl number; while the adiabatic wall enthalpy and the wall enthalpy are evaluated respectively:

$$H_{aw,y} = C_{p\infty} T_{e_y} + \frac{1}{2} R_f V_{e_y}^2 \quad (3.3)$$

$$H_w = C_{p\infty} T_w \quad (3.4)$$

At the stagnation point this method is not valid thus a different procedure is implemented. The Fay-Riddell [58] formula to calculate the convective heating rate for three-dimensional stagnation points is used. The method consists of evaluating the convective heating rate starting from the velocity gradients in both the streamwise and crosswise directions. The ratio of these two gradients is equivalent to the ratio of the two principal radii of curvature for the stagnation point:

$$q_{stag} = \sqrt{\frac{1+\iota}{2} \dot{q}_{axi}} \quad (3.5)$$

where ι is the ratio of the principal surface radii of curvature for the location of the stagnation point and q_{axi} is given by the Fay-Riddell formula:

$$\dot{q}_{axi} = 0.76 Pr^{*-0.6} (\rho_{e_y} \mu_{e_y}) (\rho_w \mu_w) \sqrt{\left(\frac{dV_e}{dx} \right)_y} (H_{aw,y} - H_w) \quad (3.6)$$

where the velocity gradient is calculated using:

$$\sqrt{\frac{dV_e}{dx}}_y = \frac{1}{Rc_{y_{min}}} \sqrt{\frac{2(p_{e_y} - p_\infty)}{\rho_{e_y}}} \quad (3.7)$$

A more detailed description of the equations utilized in the HyFlow program with a complete list of references can be found in the Wuilbercq dissertation [56]. This document also contains the extensive validation performed on this program.

3.1.2 Heat Transfer Coefficient

The heat transfer coefficient is employed, other than in the heat flux calculation, for the estimation of the surface recession using the table of dimensionless mass blowing, as illustrated by Eq. 2.11. This coefficient is calculated by HyFlow using the Reynolds analogy where this methodology is applicable. In the section of the geometry surrounding the stagnation point, where the Reynolds analogy is not applicable, the coefficient is calculated reversing Eq. 3.1:

$$\rho_e u_e C_H = \frac{q_{conv,y}}{(H_{aw,y} - H_w)} \quad (3.8)$$

3.1.3 Selection of the stagnation area

In HyFlow, the area surrounding the stagnation point, in which the Fay-Riddell formula is employed for the heat flux, is arbitrarily selected: all the points characterised by a running length inferior than a certain fixed value are to be considered part of the stagnation area. This value was selected to be equal to 0.1 m for simulations of space planes and tapered spacecraft, which were the objects HyFlow was implemented for. When this program started to be used to simulate capsules and probes, it was

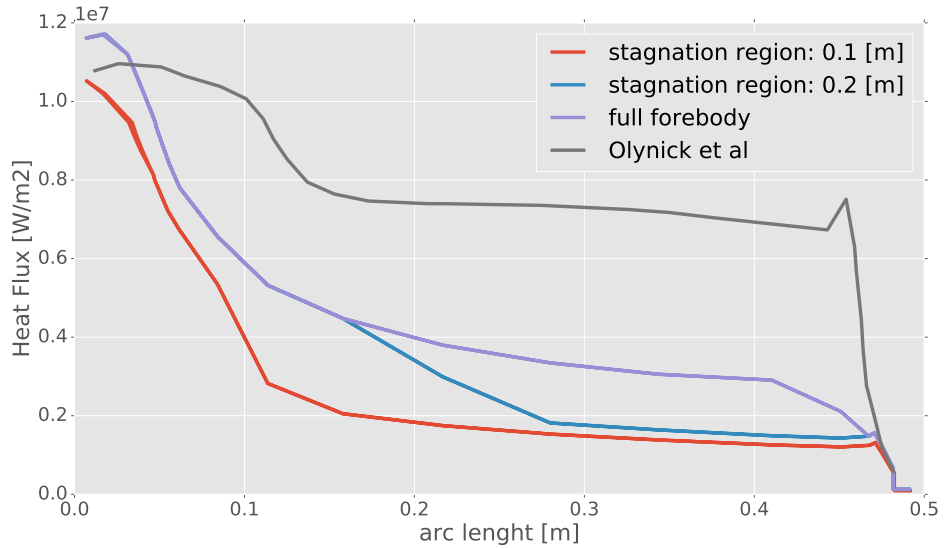


Figure 3.1: Heat flux trends, as a function of the distance from the stagnation point, for the three stagnation areas simulated; these are compared with the trend reported by Olynick *et al* [55] produced using a CFD code. All the trends are captured at the same time during the simulation. The spacecraft here simulated is the Stardust sample return capsule.

immediately clear that a fixed value for all types of spacecraft could not be utilized in these cases. Fig. 3.1, illustrates the process that was utilized to choose the right value for the stagnation area extension. At first the usual 0.1 m value was used. As it can be seen in Fig. 3.1, this produces an abrupt change in the heat flux value on the line dividing the stagnation area from the rest of the geometry. Secondly, it was decided to double the value and set it to be equal to 0.2 m. As Fig. 3.1 shows, the problem is not solved but it is just moved on a different portion of the geometry. Lastly, it was decided to use the entire forebody of the capsule as stagnation area. This makes sense physically because of the usual shape of entry capsules; the windward portion of this kind of spacecraft is quite blunt and, in case of a zero to small angle of attack, most of the forebody surface remains close to perpendicular to the flow velocity. This last test gave results without any sudden change in heat flux values and the closest comparison with CFD codes. For all of the zero angle of attack entry trajectories analysed, the same analysis was performed but it is not reported in this document. For the complete

set of this type of entries, the selection of the stagnation area equal to the capsule fore-body gave the optimum results and the best comparison with empirical or other codes results. Therefore, it is the approach that is utilized for the studies contained in this document. In the case of entry trajectories with a constant angle of attack greater than 10 degrees, a more in-depth study of the proper stagnation area has to be carried out before starting the real simulation. In this case, another option is to use a different aerodynamic code which doesn't contain this HyFlow disadvantage. For this reason and to prove that ARC is a versatile program that can be used with different aerodynamic solvers, another aerodynamic tool was selected to perform some of the analyses presented in this thesis.

3.2 Aero-thermodynamic Model: FOSTRAD

The Free Open Source Tool for Re-entry of Asteroids and Debris (FOSTRAD) [59] is another tool which was developed at Strathclyde University. It was originally created to evaluate the aero-thermodynamic characteristics of simple objects re-entering the atmosphere, such as asteroids or debris. In its current state, FOSTRAD is able to handle complex geometries making it an ideal candidate for the coupling with ARC. In contrast to HyFlow, FOSTRAD does not require a pre-defined trajectory but it can calculate it using a trajectory propagator and using an atmospheric model for the evaluation of the external air characteristics such as temperature, density or Mach number. It is able to calculate the local distribution of heat flux on the spacecraft geometry, which is one of the main inputs needed by ARC. This program can perform evaluation in free molecular and continuum flows which is an important prerequisite for any (re-)entry simulation. Additionally, three different semi-empirical models were implemented for the thermodynamic evaluations. The inputs required for the simulation are: the geometry of the object (re-)entering the atmosphere, it can be a simple model of an asteroid or a complex probe geometry, and the parameters characterizing the object energy and mass at the beginning of the entry trajectory. FOSTRAD is utilized to produce the heat flux distribution on the geometry that are used as an input by ARC.

3.2.1 Heat Flux

FOSTRAD is equipped with several aero-thermodynamic models that can calculate the heat flux values during the re-entry for continuum flows for the stagnation point.

- The Detra-Kemp-Riddell model, used in the SCARAB program, represents a super-catalytic wall condition and it uses a Reynolds number formulation:

$$C_H = \frac{2.1}{\sqrt{Re_{\infty,s}}} \quad (3.9)$$

where the Reynolds number is calculated as follow:

$$Re_{\infty,s} = \frac{\rho_{\infty} V_{\infty} R_c}{\mu(T_s)} \quad (3.10)$$

- The Fay Riddel model, which represents a fully catalytic wall condition, is the same that is used by Hyflow and which equations are reported in the previous section.
- Van Driest model is a simplification of the Fay Riddel model to avoid calculating wall properties which can be quite arduous to evaluate. In this model the heat flux is given by:

$$\dot{q}_{axi} = 0.76 Pr^{*-0.6} (\rho_{e_y} \mu_{e_y})^{0.5} \sqrt{\left(\frac{dV_e}{dx} \right)_y} (H_{aw,y} - H_w) \quad (3.11)$$

The SCARAB model is the one which has been used for the simulations presented in this work. For all the models the heat flux on panels is evaluated starting from the stagnation point heat flux value as follow:

$$Q(\theta) = Q_s (0.1 + 0.9 \cos(\theta)) \quad (3.12)$$

where θ is the local inclination of the panel referred to the local flow. More detailed information regarding the implementation of these models and the full set of equations utilised can be found in the publications by Mehta *et al* [59], [60] regarding the first

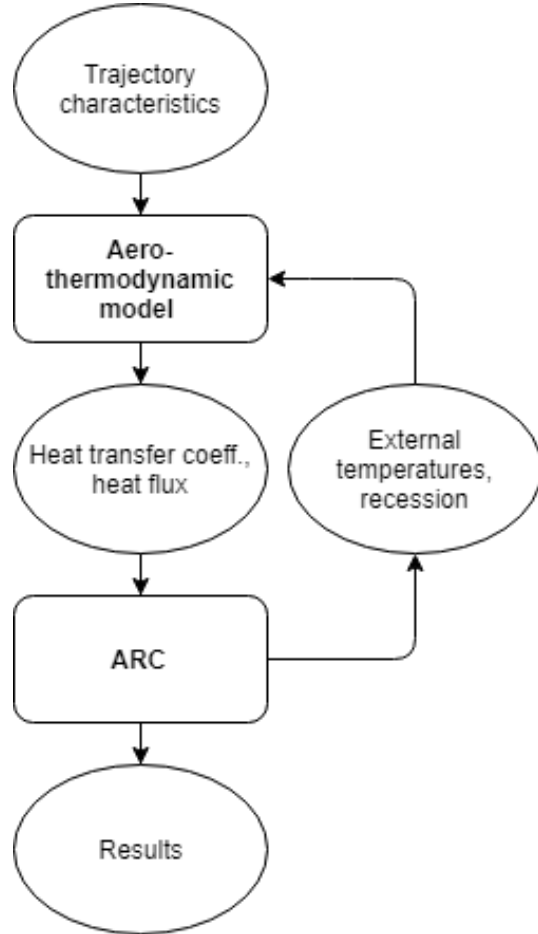


Figure 3.2: Description of the exchange of data between ARC and the aero-thermodynamic model.

code implementation and from Falchi *et al* [61], [62] for the latest code developments. The publications afore mentioned also contain the validation campaign performed on the program comparing against higher order tools like CFD and DSMC codes.

3.3 Coupling

This section describes the methodology used to couple ARC with the selected aero thermodynamic model. The coupling is fairly similar for both programs used in this thesis therefore it is only illustrated once; particular attention is devoted to highlight the differences between HyFlow and FOSTRAD coupling when discrepancies are present.

Moreover, the same coupling procedure can be used with any tool able to calculate the heat flux for atmospheric entering trajectories.

HyFlow generates steady state simulations. When it is coupled with ARC, which describes the transient thermal behaviour of the TPS, HyFlow calculates the heat flux distribution on the geometry for a number of points in which the trajectory is divided in. ARC is then integrated between two consecutive temporal points and it calculates the changes happening between those two times. For that duration the heat flux value is considered to remain constant or to vary linearly depending on the user preference. FOSTRAD is able to generate the trajectory through its trajectory propagator model, therefore, in theory, it could generate the heat flux distribution for every ARC time step. In reality, the time step required for ARC is smaller than the one needed by FOSTRAD; thus, a similar approach to the one described for the HyFlow coupling is implemented with constant or linearly variant heat flux values between two consecutive FOSTRAD time steps.

The heat flux value is the input data that the ARC program requires in order to run its simulation, once the material models and the TPS thickness are known. ARC is a one-dimensional program but it is used to produce three-dimensional evaluations. To do so, it is applied on each single vertex of the geometry. This method does not produce a real three-dimensional computation of the various characteristics because it neglects the thermal exchanges which happen between adjacent vertices, and, more generally, any point in the TPS can be influenced only by the points that sit on a line perpendicular to the material surface. Neglecting the thermal conduction between panels introduces errors, but it still describe the main thermal effects in the majority of the geometry: the effects due to the heat flux generated by the atmospheric entry. This assumption is closer to reality on the forebody, where the intensity of the heat flux is more elevated and thus, has a greater influence than in the leeward surface. The intensity of the error introduced by this assumption can be appreciated in the following chapter, thanks to the comparison of the results generated by the methodology herein presented and results calculated by codes which do not neglect the thermal conduction between adjacent points.

At the beginning of a simulation, the entire geometry is initialized to be formed by the virgin state of the ablative material, the initial thickness is also initialized to the starting value. Then, the aerodynamic model computes the heat flux value on every geometry vertex, HyFlow actually performs the evaluation on the panels and interpolates on the vertices while FOSTRAD immediately evaluates on the vertices. The ablative response code is then applied on every single vertex of the geometry. It was decided to apply the thermal response code on the vertices instead of the panels for the reason that the recession is easier to be assigned on the vertices instead of the panels without introducing errors in the geometry. The ARC code is applied for a duration equal to the difference between two consecutive trajectory points for HyFlow coupling and a FOSTRAD time step for this second type of coupling; this duration can vary from two to fifteen seconds. During the integration, ARC calculates the changes in temperature, state and thickness that occur in the selected delta time for the selected portion of geometry identified by a particular vertex. At the end of every run, these values are stored and are used as initial value for the simulation of the following trajectory point or FOSTRAD time step. The computed recession is inserted in the simulation at the end of every ARC run, the geometry is changed on the vertex normals. Fig. 3.2 and Algorithm 2 illustrate how the coupling works.

3.3.1 Coupled approach shared data between codes

In the case of the HyFlow simulations, the shared data between the two codes consist of the heat flux values, the heat transfer coefficient, from HyFlow to ARC, and the recession values, from ARC to HyFlow. In the second coupling, FOSTRAD calculates and passes to ARC the heat flux distributions, while ARC gives back the temperature distribution at the external surface (T_w) and the recession values. In both approaches, the aerodynamic code is influenced only by the change of geometry but not by other phenomena caused by the material ablation (e.g. blocking, pyrolysis gas flux). These ablation characteristics do influence the aerodynamics but their effect is neglected in the current study. This is not because these phenomena effects are inconsequential but because their influence is smaller than the influence of the phenomena that are

input: Entry table, material characteristics, spacecraft geometry

```

1 while time <= final time do
2   call aerodynamic model
3   implement recession on geometry
4   calculate input data for ARC (heat flux and heat transfer coefficient)
5   for i=0 to total number of panels do
6     /* ARC simulate behaviour on single panel */(*)
7     call ARC
8     calculate input data for aerodynamic model (external temperature,
9       recession)
10    calculate TPS behaviour (internal temperatures, degradation, etc)
11  end
12  store recession on geometry
13  store material data for following time step
14 end
```

Algorithm 2: Algorithmic form of the coupled methodology with ARC and a aerodynamic model.

taken into account and also because of the code simplicity and low running time. Introducing the chemistry of the flux would greatly increase both the code complexity and its computational requirements which is against the aim of the study and would change completely the code applications. Unfortunately, it was not possible to find the running times of the simulations performed by high-fidelity coupled methodologies, used in the next chapter. Thus, a real quantitative comparison between the two types of methodologies computational requirements cannot be herein presented. However, it can be said the the ARC-HyFlow methodology is able to conclude the full re-entry simulation in about twenty minutes. It is very unrealistic to imagine that an ordinary CFD program would be able to generate the results required for a single trajectory point in less time.

3.4 Discussion

The main aim of this chapter is the description of the three-dimensional coupled methodology that will be used in the following chapter. Other than that, the chapter is

Chapter 3. Aero-thermodynamic Models and Code Coupling

used to give a better understanding of the type of aero-thermodynamic programs that can be used in combination with ARC. Any code able to generate heat flux values on a grid of point, can take the place of the aero-thermodynamic tools used in this thesis. HyFlow and FOSTRAD were selected because they are both low computationally demanding and fitted perfectly with the study aim. Depending on the goal of the analyses to perform, this methodology can be used with more precise and more computationally demanding tools like CFD codes. Moreover, the same methodology can be applied for two-dimensional geometries instead of three-dimensional ones. This shows that the ARC coupled method is very versatile and it can be used in a variety of different ways for a number of distinct purposes. Considering to the explanation contained in this chapter, it should be easy to couple any available aerodynamic model with ARC.

Chapter 4

Three-dimensional test cases

This chapter contains the simulations performed by the coupled version of the ARC program and the selected aero-thermodynamic program for real mission cases. The first section of the chapter contains Earth re-entries while the second part focuses on entries in other planets atmospheres. Comparative results to real re-entry data or validated codes are presented whenever possible; unfortunately, the majority of the cases found in literature are two-dimensional analyses of a section of the capsule forebody in an axi-symmetric case. For this reason, the calculations performed on the leeward surface do no present any comparison with real data nor high order codes in the following sections. Moreover, the recession values are rarely illustrated in literature and only some of the cases studied contain a comparison for this parameter.

4.1 Earth re-entry

Both HyFlow and FOSTRAD were created to perform Earth atmosphere analyses; therefore, no changes had to be implemented in the aerodynamic models to run Earth re-entry simulations.

4.1.1 Stardust re-entry with HyFlow

The test case proposed here is the re-entry of the Stardust sample return capsule (SRC) while the aero-thermodynamic program utilized in this simulation is HyFlow. The TPS

Table 4.1: Time instances for the Stardust sample return capsule re-entry trajectory.

| Time [s] | Mach | Temperature [K] | Pressure [Pa] |
|----------|------|-----------------|---------------|
| 34 | 42.7 | 0.60 | 216.93 |
| 42 | 41.6 | 2.64 | 221.42 |
| 48 | 39.6 | 6.96 | 229.00 |
| 54 | 36.0 | 16.01 | 238.47 |
| 58 | 32.6 | 25.48 | 245.37 |
| 60 | 30.8 | 31.3 | 248.48 |
| 64 | 26.9 | 44.81 | 252.71 |
| 66 | 24.9 | 52.45 | 253.55 |
| 70 | 21.2 | 69.37 | 255.05 |
| 76 | 16.1 | 99.5 | 256.9 |
| 80 | 13.4 | 121.18 | 255.99 |

of the capsule was formed by two different materials, PICA and SLA-561 V [55], and its thickness varied depending on its position on the capsule: the fore-body was covered by a thicker ablative layer than the aft-body. In order to represent this inhomogeneity, the simulation was performed considering the PICA material of thickness 6.0 cm for the forebody and a 3.0 cm of SLA 561 V for the rest of the geometry. Fig. 4.1a shows the Stardust SRC geometry and mesh used by the flow solver, while Fig. 4.1b illustrates the initial TPS thickness. The simulation flow conditions for eleven time instances during the re-entry phase are shown in Table 4.1.

The evaluated flow is compared with the results obtained using high-fidelity codes such as CFD tools, in which the chemistry of the external air and the internal gases is included while it is neglected both internally and externally, in the proposed approach. Therefore, some differences in the calculated results are to be expected. Fig. 4.2 illustrates the comparison between the heat flux at the stagnation point evaluated by Olynick *et al* [55], generated assuming a fully catalytic radiative equilibrium wall boundary condition, and the heat flux evaluated by HyFlow as a function of time. HyFlow overestimates the heat flux due to the fact that it neglects the chemistry taking place in the external flux. To mitigate this overestimation, it was determined to apply a corrective factor of 0.8 to the heat flux values, before providing those to ARC for the simulations. In Cassineli thesis [63], the heat flux generated by the re-entry of a capsule is studied with high-fidelity tools. It presents the same simulation with and without

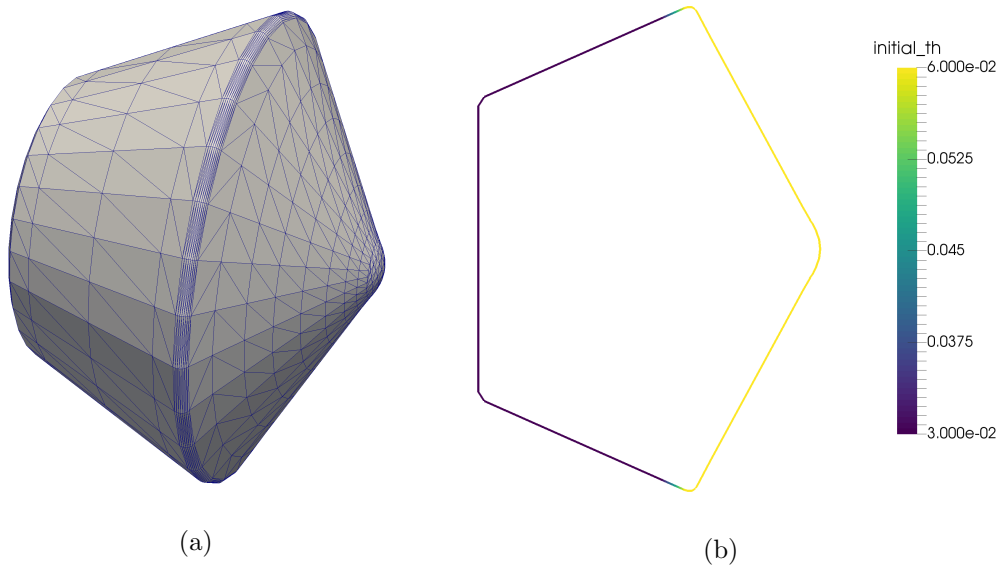


Figure 4.1: Initial conditions for the Stardust simulation performed using HyFlow solver. On the left: Illustration of the Stardust Sample Return Capsule geometry and of the mesh utilized in the HyFlow calculation. On the right: Initial TPS thickness on the capsule surface; the 6 cm part is formed by PICA while the 3 cm is made of SLA 561 V.

chemistry for two different altitudes. In both cases the decrease of the heat flux for the simulation with chemistry is about 20%. Because of the similarity of the Stardust case with the case presented by Cassineli, it was decided that the assumption of 20% losses caused by the flow chemistry was considered to produce conservative results. In particular, Fig. 4.2 shows that, in the current case study, the heat flux at the stagnation point by Olynic *et al* [55] is still lower than 80% of the heat flux calculated by HyFlow. Unfortunately, the assumption of conservative results might not be true for the leeward part of the geometry that sees a lower external temperature. This was not considered problematic because those regions of the geometry are less demanding in terms of TPS requirements. If conservative conditions on the entire capsule are preferred, the current approach gives the possibility to apply the corrective factor only on the forebody and use 100% of the heat flux calculated by HyFlow on the back-shield.

Fig. 4.4 illustrates the heat flux distribution on the windward side of the capsule for the instance of peak heat flux (54 s). As expected, the stagnation point is the

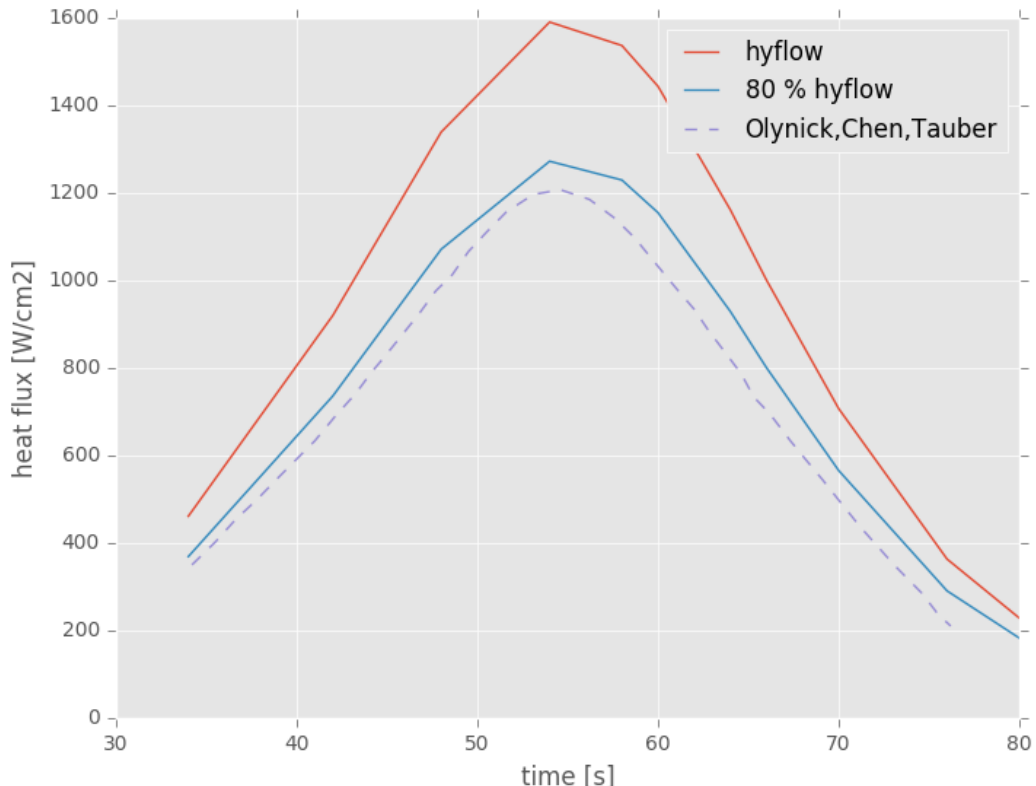


Figure 4.2: Comparison of the heat flux at stagnation point as function of time. The dotted line is the heat flux evaluated by Olynick *et al* [55] using a CFD solver while the solid lines represent the heat flux estimated by HyFlow and the heat flux used to perform the analyses which correspond to 80% of the previous value.

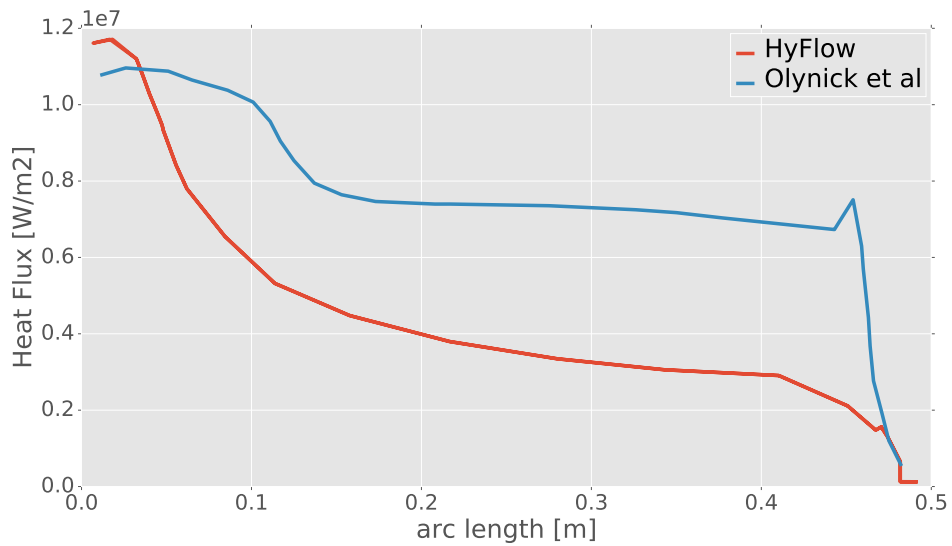


Figure 4.3: Heat flux trend at the time of peak heat flux (54 s) along a Stardust capsule section passing for the stagnation point, compared with what reported by Olynick *et al* [55]. Simulated using HyFlow solver.

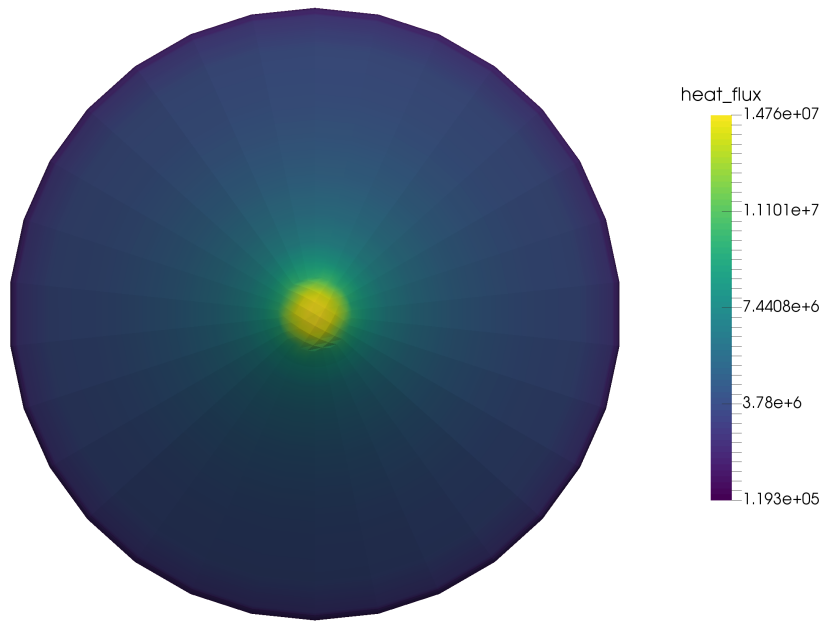


Figure 4.4: Heat flux distribution [W/m²] on the windward surface of the Stardust capsule at the time of peak heat flux (54 s). Simulated using HyFlow solver.

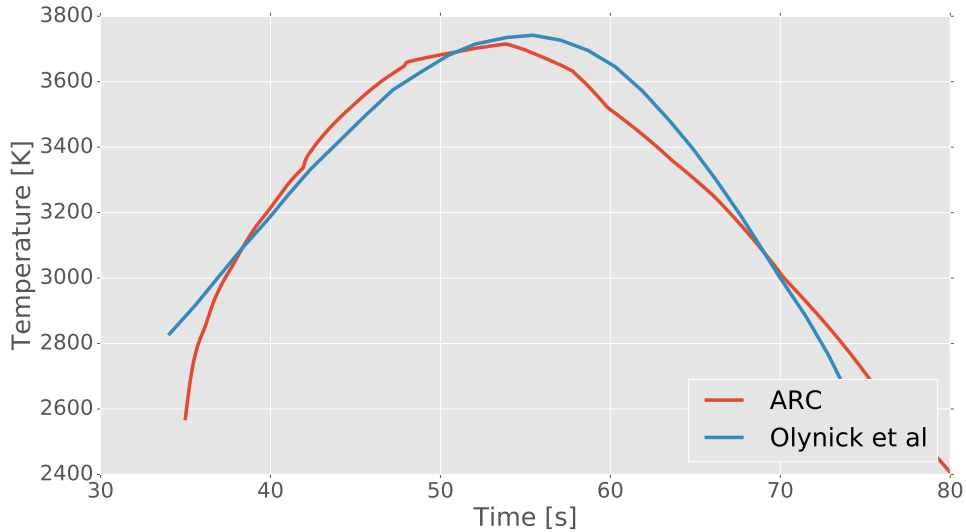


Figure 4.5: Comparison of the temperature at the stagnation point as function of time evaluated by the current study and by Olynick *et al* [55] for the Stardust capsule. Simulated using HyFlow solver.

location of maximum heat flux on the geometry. The heat flux values along a section of the forebody passing through the stagnation point, equal to the yellow part of the section illustrated in Fig. 4.1b, is shown in Fig. 4.3; this graph highlights the significant difference between the value at the stagnation location and the rest of the front surface. In reality, the difference between the stagnation location and the shoulder is lower than the one estimated by HyFlow [28], [55]. These discrepancies introduce errors in the properties calculated by ARC such as temperatures and recession. This means that HyFlow only overestimates the heat flux value in an area close to the stagnation point, and the assumption of 20% of heat flux decrease due to chemistry is only valid there. Since the papers used for comparison present more information regarding this area than the rest of the geometry, it was decided to keep the corrective factor of 0.8 for the heat flux. Doing so, the stagnation area is well represented in terms on heat flux values and it was possible to present a fairer representation of ARC capabilities in that area, where the final results are not so influenced by the aerodynamic program inaccuracy.

The small scatter of the trend visible on this type of figures (Fig. 4.3 and similar) is due to the coarse mesh used for the simulation. A finer mesh would give a smoother

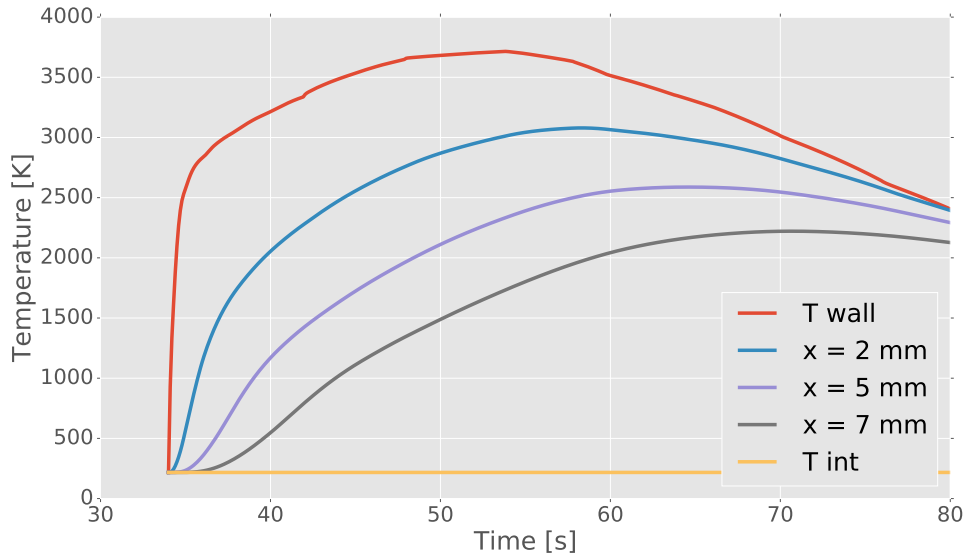


Figure 4.6: Temperature trend as a function of time at various thickness locations for the stagnation point; T_{wall} , equivalent to $x=0\text{ mm}$, represents the wall temperature while T_{int} , equivalent to $x=60\text{ mm}$ represents the temperature for the internal TPS surface. Stardust test case simulated using HyFlow solver.

trend (see FOSTRAD simulations) but, it was decided to use the coarse mesh because a smoother trend was not considered worth the increased computational demand due to a finer mesh. Fig. 4.5 shows a comparison of the external temperature of the stagnation point as a function of time calculated with the current approach and the one generated by Olynick *et al* [55]. The maximum discrepancy between the two trends is lower than 10%. There is a small difference regarding the time of maximum temperature, this discrepancy is probably caused by the method used to determine the heat flux value between two trajectory points. The ARC coupled methodology uses a simple linear interpolation while the approach presented in the paper might use a different method. Unfortunately, the paper does not report this piece of information. Fig. 4.6 illustrates how the temperature at the stagnation point for various TPS thickness locations, evolves during the re-entry. The x values in the figure caption refers to the initial distance of the selected points from the external surface; these points are considered to behave as fixed thermocouples therefore, the x values decrease during the simulation due to the material recession.

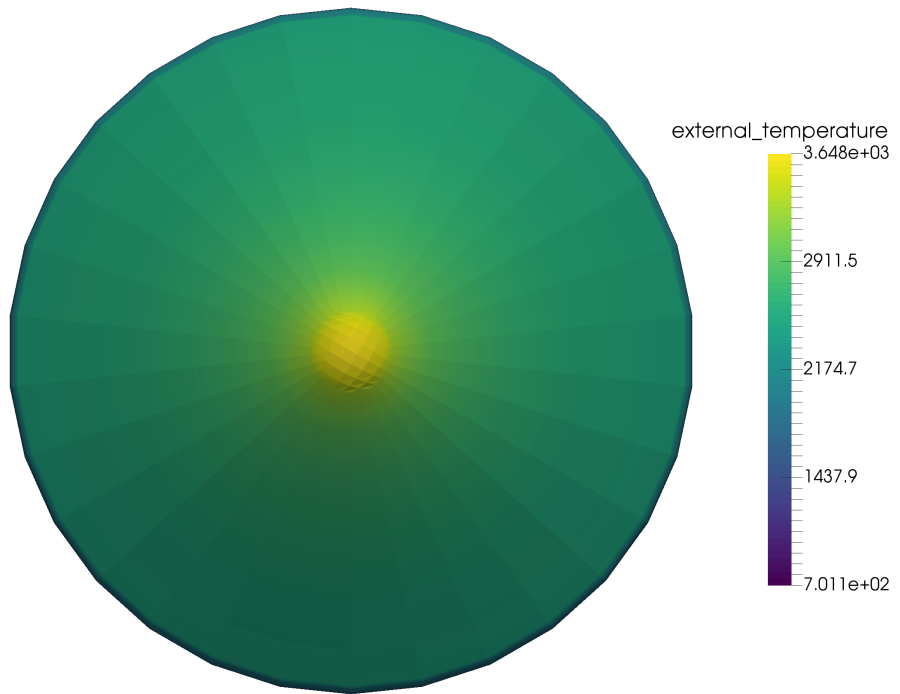


Figure 4.7: External temperature distribution [K] of windward surface of the Stardust capsule at the time of peak heat flux (54 s). Simulated using HyFlow solver.

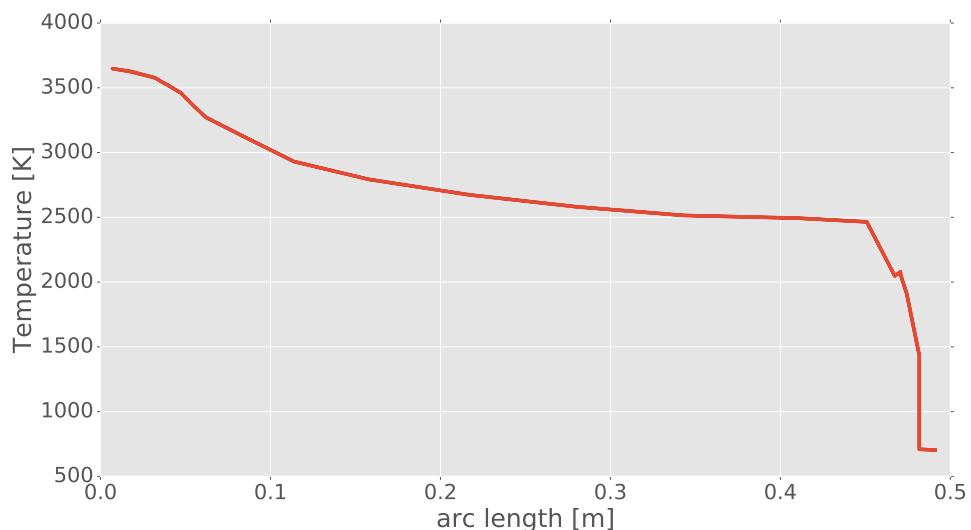


Figure 4.8: External temperature trend at the time of peak heat flux (54 s) along a Stardust capsule section passing for the stagnation point. Simulated using HyFlow solver.

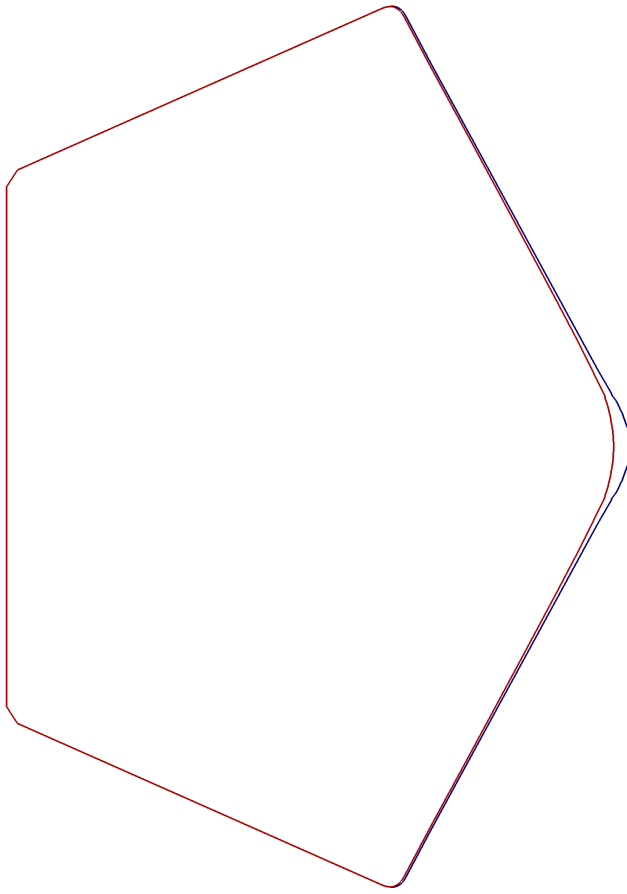


Figure 4.9: Comparison between a section of the geometry at the beginning of the analysis and a section of the geometry after the analysis was completed (80 s) for the Stardust test case using HyFlow solver.

The external temperature distribution of the capsule fore-body for the instance of peak heat flux (54 s) is displayed in Fig. 4.7. The stagnation point corresponds to the maximum temperature as it is directly dependent on the heat flux. The external temperature along the capsule side is shown in Fig. 4.8. Unfortunately, the papers used for comparison do not report this temperature distribution thus, no comparison is illustrated in Fig. 4.8.

Fig. 4.9 illustrates the comparison between a section of the capsule at the beginning at the end of the simulation. The internal section corresponds to the recessed geometry while the external one corresponds to the initial geometry. The distance between the two sections is higher in the region surrounding the stagnation point and it decreases

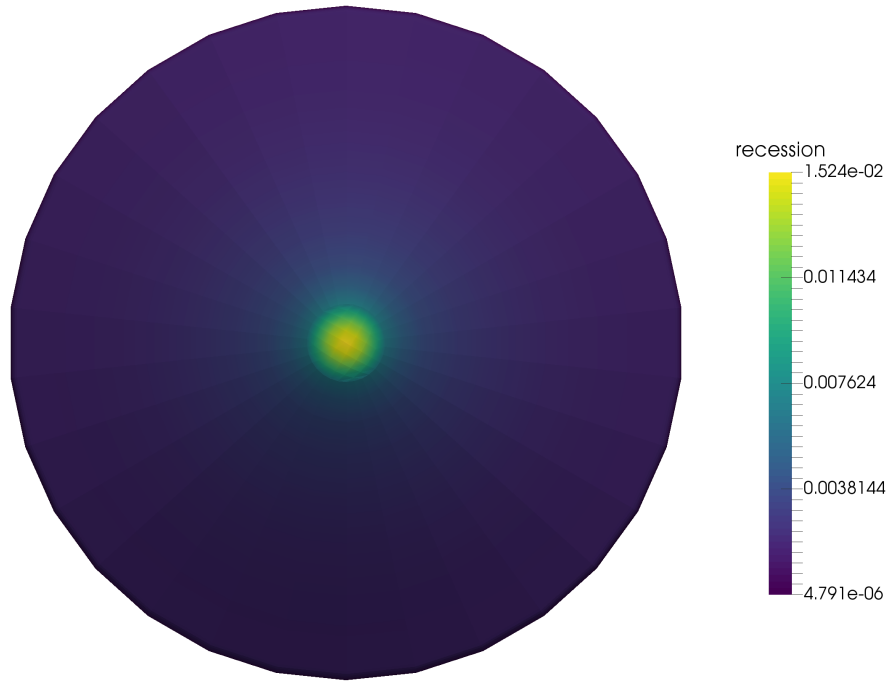


Figure 4.10: Recession [m] of the Stardust capsule forebody at the end of the simulation (80 s). Test case performed using HyFlow solver.

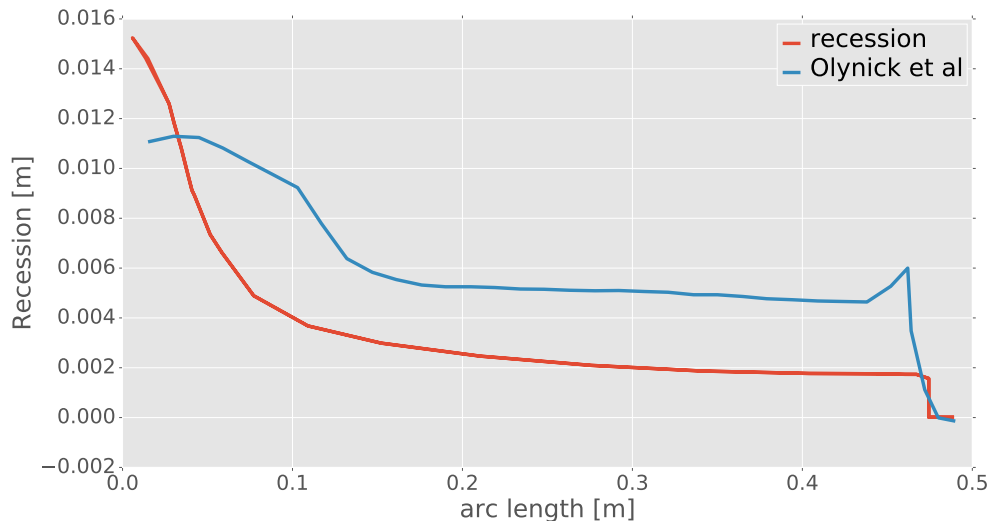
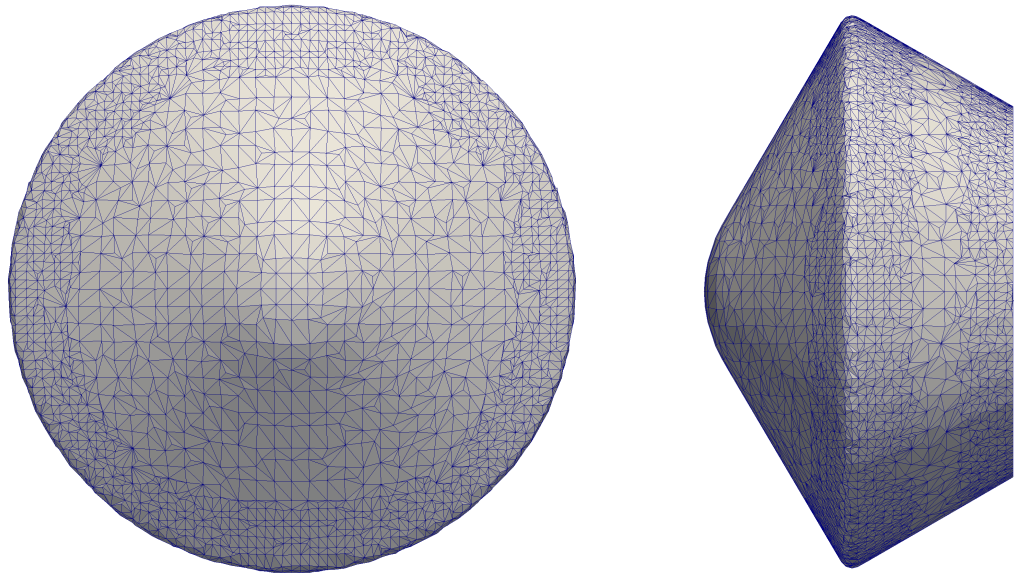


Figure 4.11: Recession of the capsule as a function of the distance from the stagnation point along the the capsule geometry at the end of the simulation (80 s) for the Stardust test case and HyFlow coupled methodology. Compared with the recession reported by Olynick *et al* [55]



(a) Illustration of the capsule forebody. (b) Illustration of the capsule side.

Figure 4.12: Illustrations of the Stardust Sample Return Capsule geometry and of the mesh utilized in the FOSTRAD calculation.

farther away from that point. Moreover, the change of shape on the leeward side of the capsule is less evident than the one on the windward side. Fig. 4.10 represents the recession along the fore-body of the capsule. The maximum recession is located at the stagnation point and it is equal to 15 mm; Olynick *et al* [55] found a recession of 12 mm for the stagnation point. Fig. 4.11 shows how the recession is underestimated for the part of the forbody close to the capsule shoulder. This error is caused by aerodynamic code underestimation of the heat flux value in the same area.

4.1.2 Stardust re-entry with FOSTRAD

To evaluate the capabilities of the coupled approach performed with the FOSTRAD model, the Stardust sample return capsule case was also simulated using this second model.

Fig. 4.12 shows the capsule geometry utilised by FOSTRAD for its simulations; the number of panels constituting the geometry is almost an order of magnitude higher than the one utilised by HyFlow because of the model requirements. Consequently,

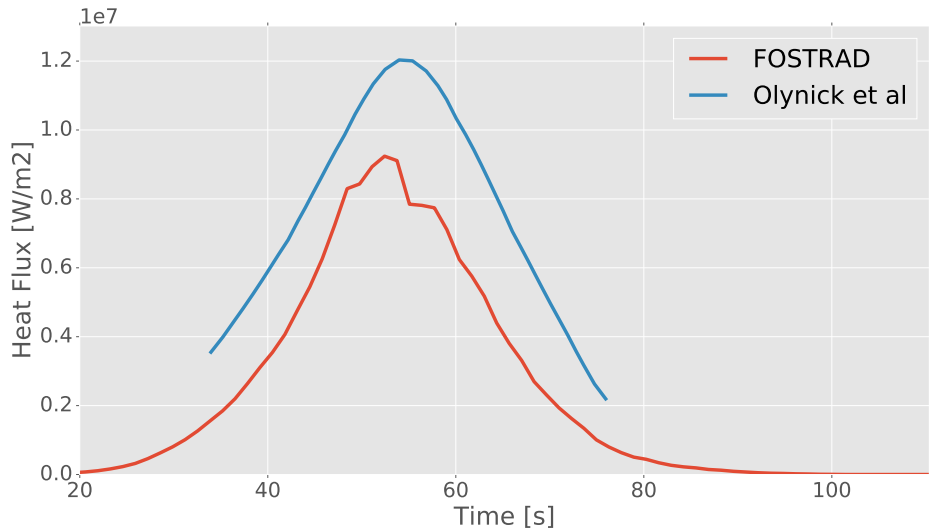


Figure 4.13: The heat flux at the stagnation point as a function of time as calculated by FOSTRAD for the Stardust test case.

this second simulation is more time demanding than the previous one, it takes about an order of magnitude more time to complete the same re-entry, but a higher accuracy for the heat flux variation on the forebody is expected. The longer running time is solely caused by the increased number of ARC calculations required for the finer mesh, and it does not mean that FOSTRAD is slower than HyFlow for similar operations. However, the finer mesh is a FOSTRAD requirement therefore, the faster simulation performed with FOSTRAD will always be significantly slower than the fasted simulation performed using HyFlow for the same re-entry. Nevertheless, a finer mesh should lead to a more accurate heat flux distribution. Fig. 4.13 represents the heat flux value for the stagnation point as a function of time; this figure shows that the simulation accounts for a longer portion of the re-entry in this case, from 0 s to 130 s, with respect to the previous case, from 30 s to 80 s. The scattering in the trend is due to the change in external characteristics between two consecutive time instances in Table 4.1 and the method used by FOSTRAD to calculate the heat flux value between those instances. In order to compare results in the fairest fashion possible, the recession estimates are illustrated at 80 s, which is the end time of the previous simulation, instead of 130 s. However, some differences in the results are to be expected because

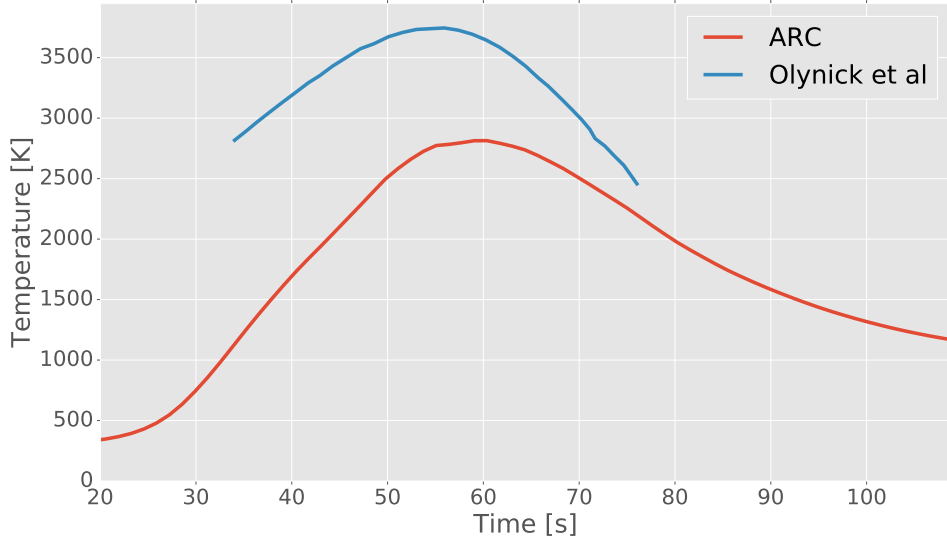


Figure 4.14: The external temperature at the stagnation point as a function of time generated by ARC utilizing FOSTRAD heat flux estimates.

this simulation starts at 0 s while the previous one started at 30 s. These differences should be minor because the heat flux in the first 30 s of the re-entry is so low that was considered negligible by both Olynick *et al* [55] and Chen and Milos [28]. Fig. 4.14 shows the external temperature trend at the stagnation point as a function of time; since FOSTRAD calculates a lower heat flux than HyFlow, the temperature also results lower than the previous simulation.

The heat flux on the forebody of the capsule and its trend on a section of the geometry at the time of peak heat flux (54 s) are represented respectively by Fig. 4.15 and Fig. 4.16. It is possible to see that, the distribution of heat flux on the surface differs from the HyFlow simulation and, in particular, it has a lower difference between the highest and lowest value on the forebody. The comparison with Olynick *et al* [55] results show that FOSTRAD evaluates the value of the heat flux for the capsule shoulder better than HyFlow. However, HyFlow produces better results for the stagnation point area. This heat flux distribution influences all the variables calculated by ARC such as temperatures or recession values as the following figures show.

Fig. 4.17 and Fig. 4.18 illustrate the distribution of external temperature at the

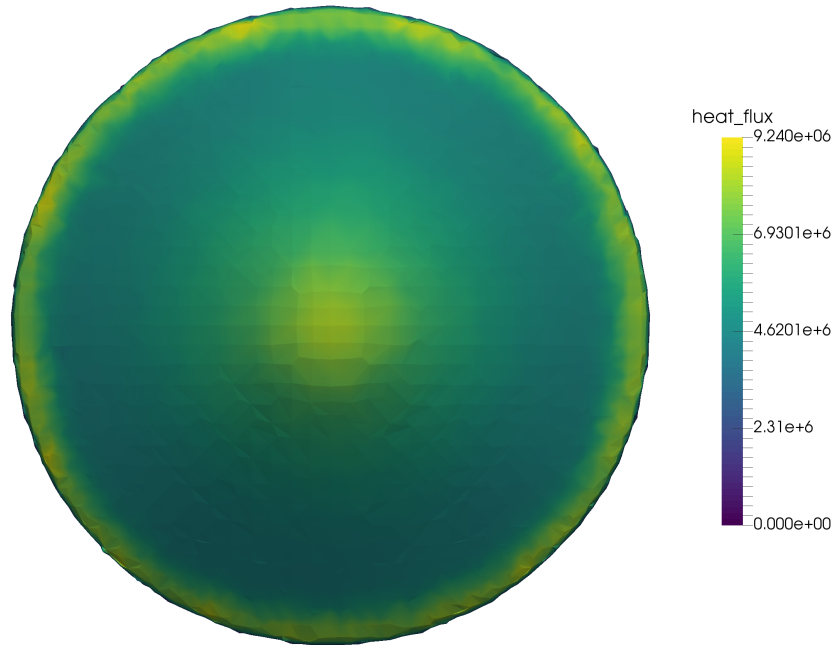


Figure 4.15: Heat flux [W/m^2] distribution on the windward surface of the Stardust capsule at the time of peak heat flux (54 s). Simulation performed utilizing FOSTRAD solver.

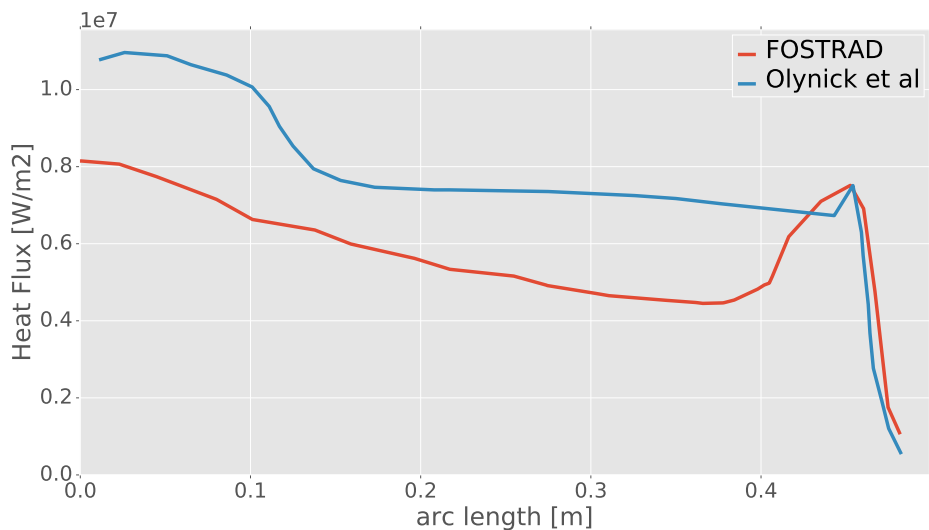


Figure 4.16: Heat flux trend at the time of peak heat flux (54 s) along a Stardust capsule section passing for the stagnation point. Simulation performed utilizing FOSTRAD solver.

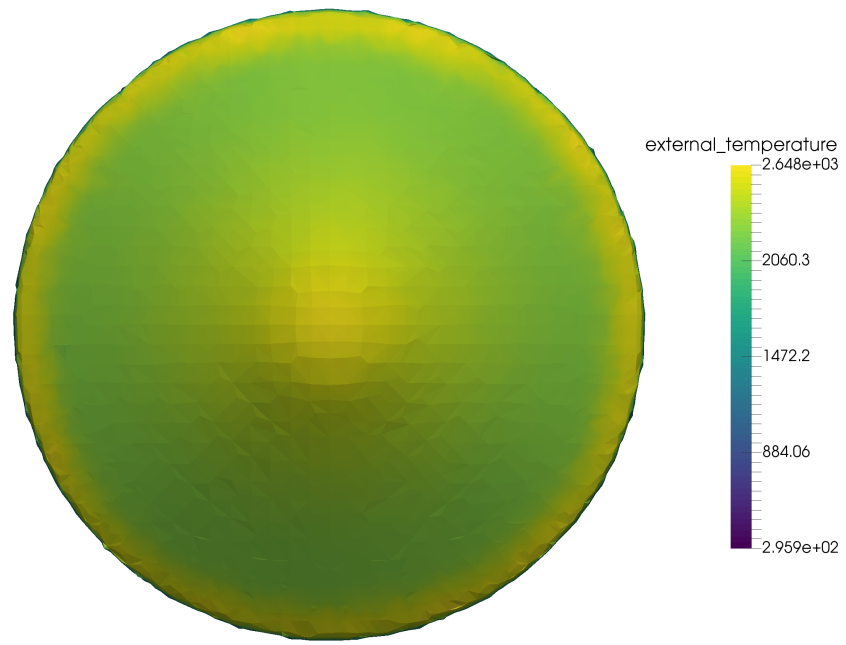


Figure 4.17: External temperature distribution [K] on the windward surface of the Stardust capsule at the time of peak heat flux (54 s). Simulation performed utilizing FOSTRAD solver.

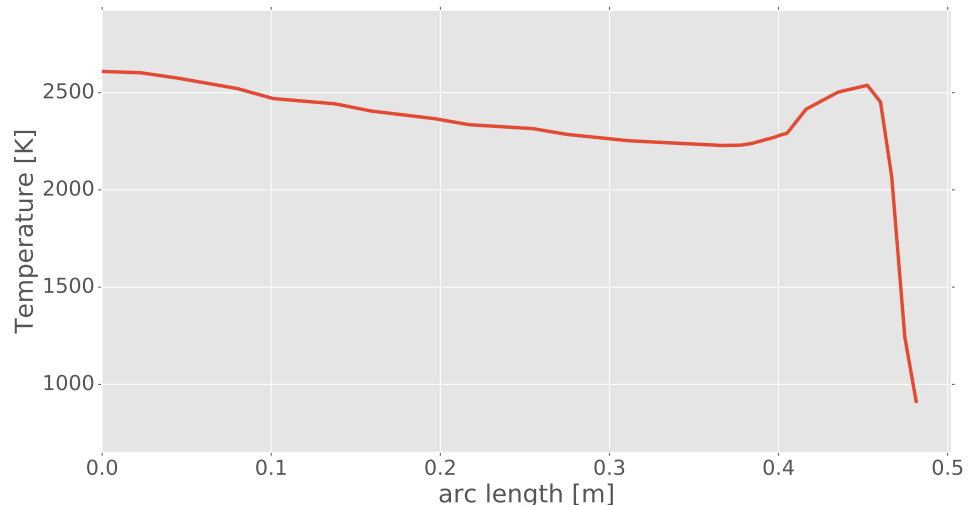
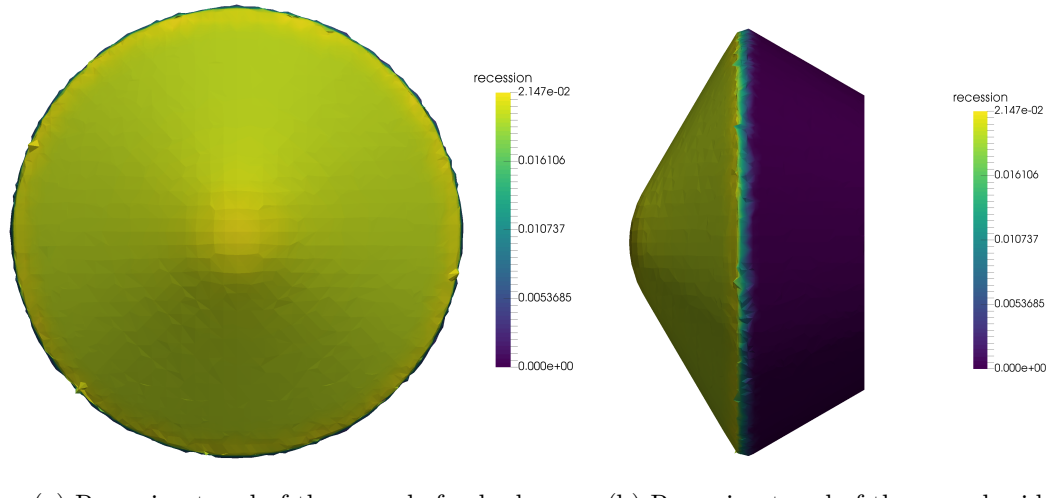


Figure 4.18: External temperature trend at the time of peak heat flux (54 s) along a Stardust capsule section passing for the stagnation point. Simulation performed utilizing FOSTRAD solver.



(a) Recession trend of the capsule forebody. (b) Recession trend of the capsule side.

Figure 4.19: Recession [m] of the capsule at 80 s. Stardust test case performed utilizing FOSTRAD solver.

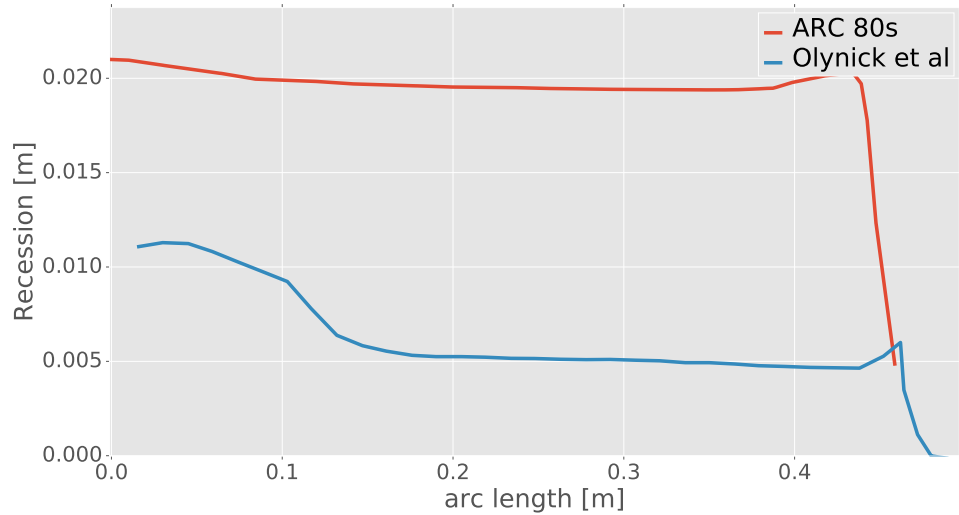


Figure 4.20: Recession of the Stardust capsule as a function of the distance from the stagnation point along the the capsule geometry at 80 s. Simulation performed utilizing FOSTRAD solver.

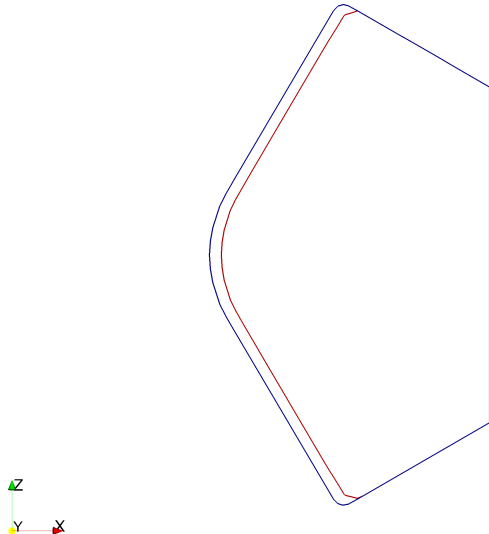


Figure 4.21: Comparison between a section of the Stardust geometry at the beginning of the analysis and a section of the geometry after 80 s. Simulation performed utilizing FOSTRAD solver.

time of peak heat flux (54 s) during the re-entry, for the entire forebody and for a section of that part of the geometry, respectively. While Fig. 4.19 and Fig. 4.20 represent the recession distribution on the capsule at 80 s. The recession on the leeward surface is equal to zero because FOSTRAD does not calculate the heat flux on the shadowed panels of the geometry. These figures highlight how a different heat flux distribution affects the calculation performed by ARC and show that the inaccuracies in the data evaluated by the thermodynamic model are carried out in the ARC calculations, even if the material program is capable of a higher precision as shown in chapter 2. Lastly, Fig. 4.21 shows the section of the capsule at the beginning of the re-entry and after 80 s, illustrating the recession of the TPS. The maximum value in this simulation is higher than the one evaluated in the previous simulation; this difference is due to the longer simulation time and a slight overestimation of the recession in ARC results as shown in chapter 2.

Table 4.2: Time instances of the re-entry trajectory for the Atmospheric Re-entry Demonstrator.

| Time [s] | Mach | Temperature [K] | Pressure [Pa] |
|----------|-------|-----------------|---------------|
| 4879 | 26.93 | 196.65 | 0.89 |
| 4885 | 26.66 | 200.65 | 1.25 |
| 4898 | 26.19 | 206.65 | 2.07 |
| 4911 | 25.63 | 212.65 | 3.37 |
| 4923 | 24.92 | 220.25 | 5.42 |
| 4939 | 23.94 | 228.65 | 8.55 |
| 4973 | 22.03 | 237.05 | 13.28 |
| 5013 | 19.49 | 245.45 | 20.31 |
| 5036 | 17.71 | 253.85 | 30.63 |
| 5051 | 16.28 | 262.25 | 45.56 |
| 5067 | 14.49 | 270.65 | 66.94 |
| 5087 | 12.41 | 270.65 | 97.75 |
| 5109 | 10.21 | 265.05 | 143.14 |
| 5130 | 8.25 | 256.65 | 212.03 |
| 5148 | 6.57 | 248.25 | 318.22 |
| 5165 | 5.13 | 239.85 | 484.32 |
| 5182 | 3.90 | 231.45 | 748.23 |
| 5198 | 2.89 | 226.65 | 1171.87 |
| 5212 | 2.14 | 223.65 | 1847.46 |
| 5226 | 1.54 | 220.65 | 2930.49 |
| 5241 | 1.01 | 217.65 | 4677.89 |
| 5257 | 0.65 | 216.65 | 7504.84 |
| 5275 | 0.61 | 216.65 | 12044.60 |

4.1.3 The Atmospheric Re-entry Demonstrator

The second test case is the re-entry of the Atmospheric Re-entry Demonstrator (ARD) which mission was successfully completed in 1998 [64]. This simulation differs from the previous one because, the paper used for the comparison did not contain a complete table of points describing the external environment characteristics for the trajectory. The standard atmosphere model (ISA) [65] was instead used to calculate the missing atmospheric data required by HyFlow. For this reason, higher errors in the heat flux calculation are to be expected. Table 4.2 contains the trajectory point characteristics used for the simulation; external air temperatures and pressures are part of the data calculated using the standard atmosphere model. Fig. 4.22 shows the geometry of the capsule and the mesh employed for the HyFlow calculation. The ablative material

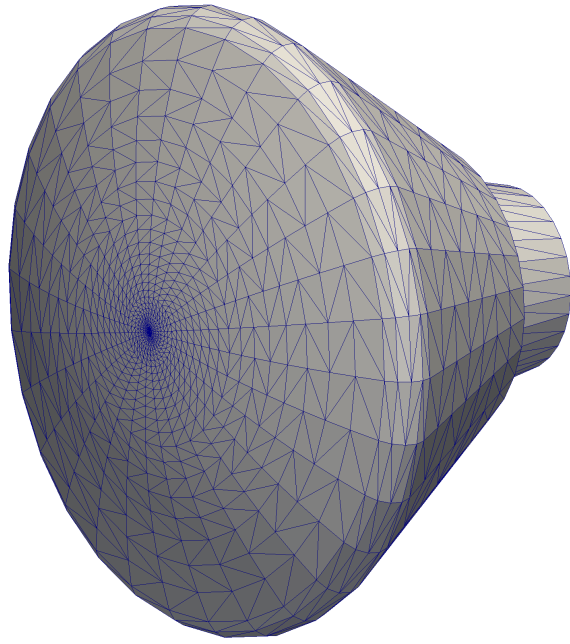


Figure 4.22: Illustration of the Atmospheric Re-entry Demonstrator Capsule geometry and of the mesh utilized in the HyFlow calculation.

was composed of Aleastrasil silica-phenolic tiles for the forebody of the capsule and of NORCOAT-LIEGE, a cork impregnated of a phenolic resin, tiles for the rest of the geometry [64]. Unfortunately, it was impossible to find enough data to produce an adequate model for NORCOAT-LIEGE material. Consequently, a single material TPS, made of Aleastrasil, with a thickness of 1.0 cm was utilized for the entire geometry. In addition, it was very difficult to find in literature precise and accurate information regarding the data necessary for its material model; thus, the Aleastrasil model is characterized by greater uncertainty than the other material models produced.

Another peculiarity of this test case is the presence of a large angle of attack during the entire trajectory. This angle experiences small variations during the trajectory however, it was considered to be constant and equal to 20 degree in this simulation. In the case of larger changes in this angle, a variable angle of attack simulation can be generated by the current version of the codes.

Fig. 4.23 shows the heat flux value at the stagnation point as a function of time. As for the previous Earth's re-entry, HyFlow overestimates the heat flux therefore, the

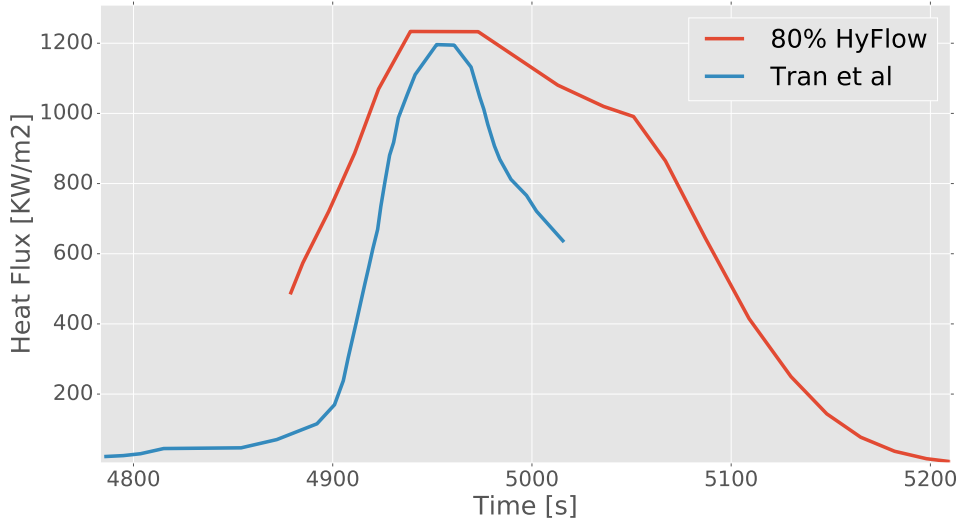


Figure 4.23: Comparison of the heat flux at stagnation point as function of time. The blue line is the heat flux evaluated by Tran *et al* [64] while the red line represents the heat flux used to perform the analyses which correspond to 80% of the value calculated by HyFlow. Atmospheric Re-entry Demonstrator test case.

corrective coefficient of 0.8 was also introduced. This figure shows that the maximum value is well evaluated, however, for the second part of the trajectory, the heat flux is overestimated. These discrepancies can be due to one of two different causes or by a combination of them. One cause can be the use of the standard atmosphere model instead of real data collected during the flight; this would create the higher errors in the lower part of the atmosphere, where the external conditions have higher variation from the standard model. Since the actual complete set of atmospheric data recorded during the re-entry is not present in literature, it is not possible to perform a simulation with the actual re-entry condition to compare with the simulation generated with the use of the standard atmosphere model. An uncertainty analysis performed on the standard atmosphere model is advisable when selecting the TPS design and, in particular, when sizing the ablator thickness. However, the study herein illustrated was presented to show the methodology ability to simulate different Earth re-entries, in particular lower heat fluxes than the Stardust case and the presence of an angle of attack. The result of such uncertainty analysis, even if essential in the TPS design phase, was not considered

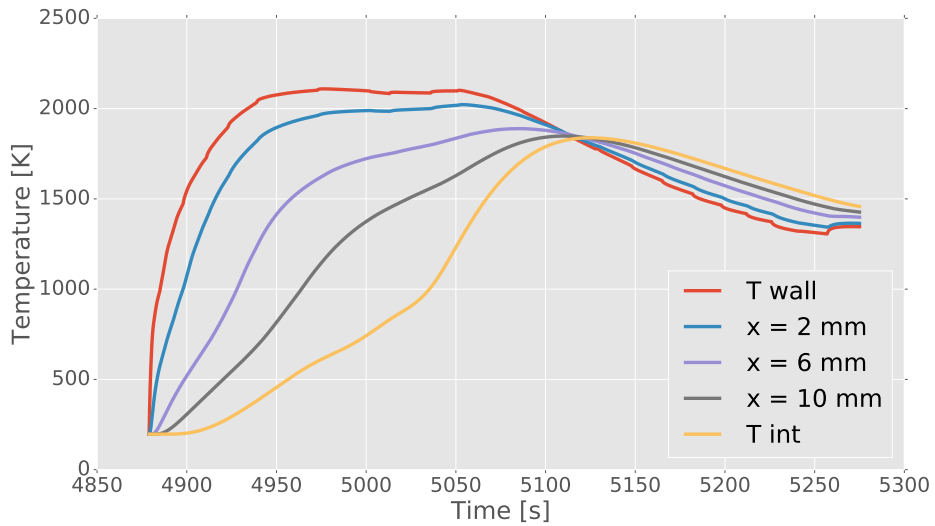


Figure 4.24: Temperature trends as a function of time at various thickness locations for the stagnation point; T_{wall} , equivalent to $x=0 \text{ mm}$, represents the wall temperature while T_{int} , equivalent to $x=10 \text{ mm}$, represents the temperature for the internal TPS surface. Atmospheric Re-entry Demonstrator test case simulated using HyFlow.

necessary in this case. Another cause can be in the inaccuracy of the measurements produced by the instrumentation utilized to extract the heat flux values used for the comparison. This data is also incomplete due to the failure of the thermocouple closer to the stagnation point [64].

Fig. 4.24 illustrates the TPS temperatures as a function of time at the stagnation point. The various trends depict the temperatures for the external surface, several points in the TPS thickness and the internal surface, which is the one representing the interface between the hot structure, TPS, and the cold structure, the internal shell of the capsule built for structural integrity. The x values in the figure caption refer to the initial location of the selected points; these values decrease during the simulation due to the material recession. This figure highlights how the external temperature trend is very similar to the heat flux one while the internal temperature has a different behaviour and it reaches its maximum with a consistent delay in comparison to the external temperature. This behaviour is typical of TPS and it is accentuated in this case by the high insulating properties of the Aleastrasil material.

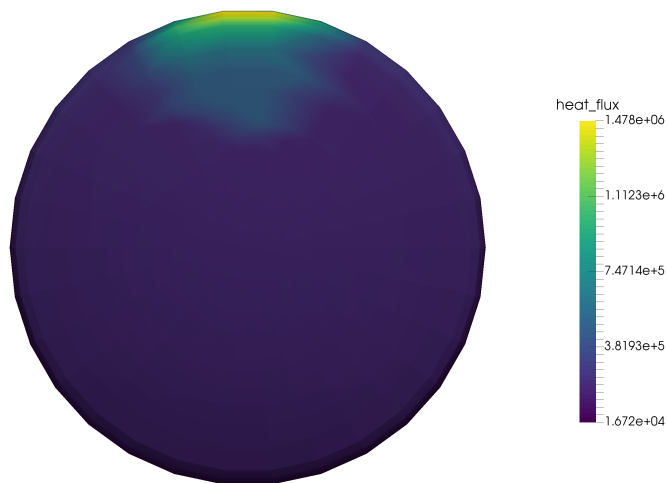


Figure 4.25: Heat flux distribution [W/m^2] on the windward surface of the capsule at the time of peak heat flux (4939 s). Atmospheric Re-entry Demonstrator test case simulated using HyFlow.

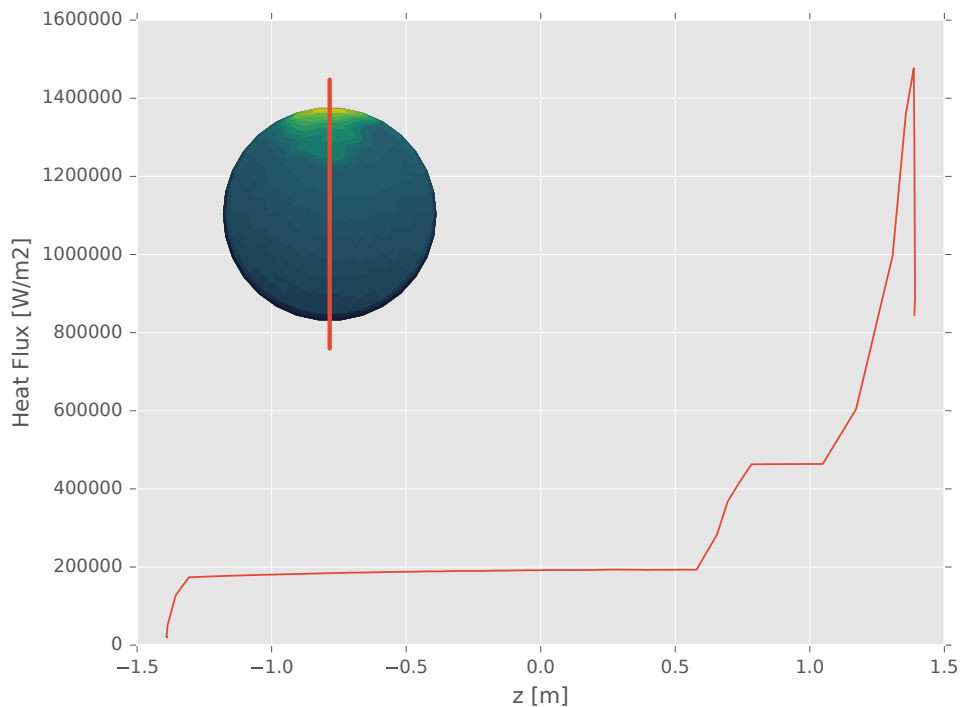


Figure 4.26: Heat flux trend at the time of peak heat flux (4939 s) along a capsule section passing for the stagnation point. Atmospheric Re-entry Demonstrator test case simulated using HyFlow.

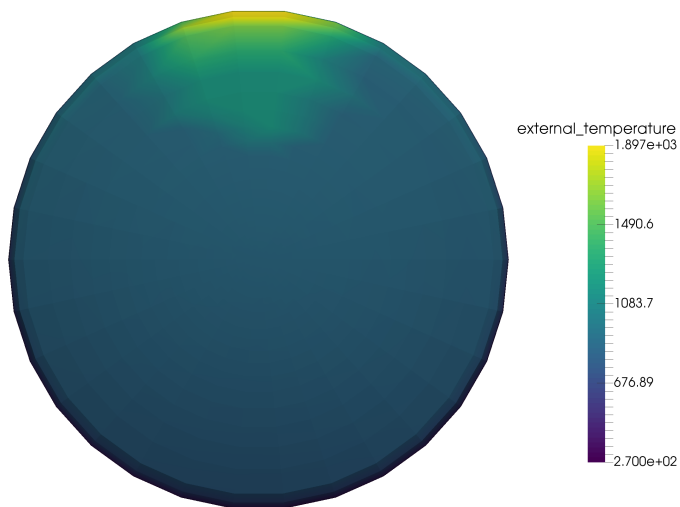


Figure 4.27: External temperature distribution [K] of windward surface of the capsule at the time of peak heat flux (4939 s). Atmospheric Re-entry Demonstrator test case simulated using HyFlow.

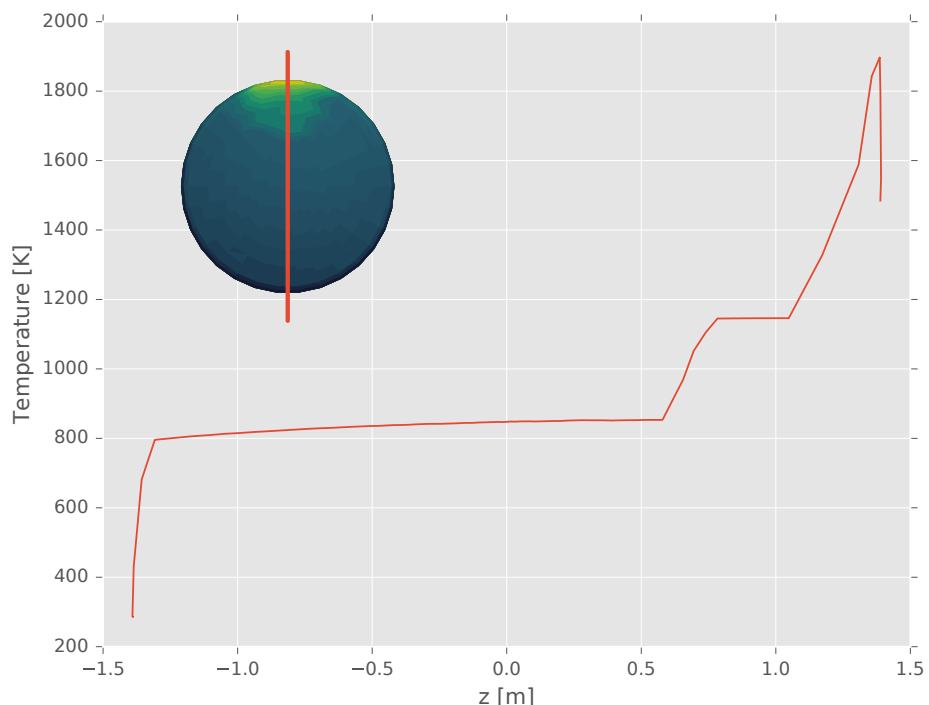


Figure 4.28: External temperature trend at the time of peak heat flux (4939 s) along a capsule section passing for the stagnation point. Atmospheric Re-entry Demonstrator test case simulated using HyFlow.

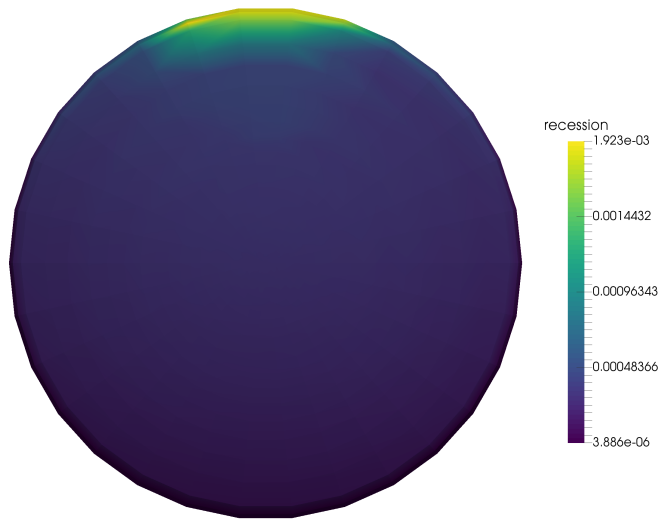


Figure 4.29: Recession distribution [m] on the windward surface of the capsule at the end of the simulation. Atmospheric Re-entry Demonstrator test case simulated using HyFlow.

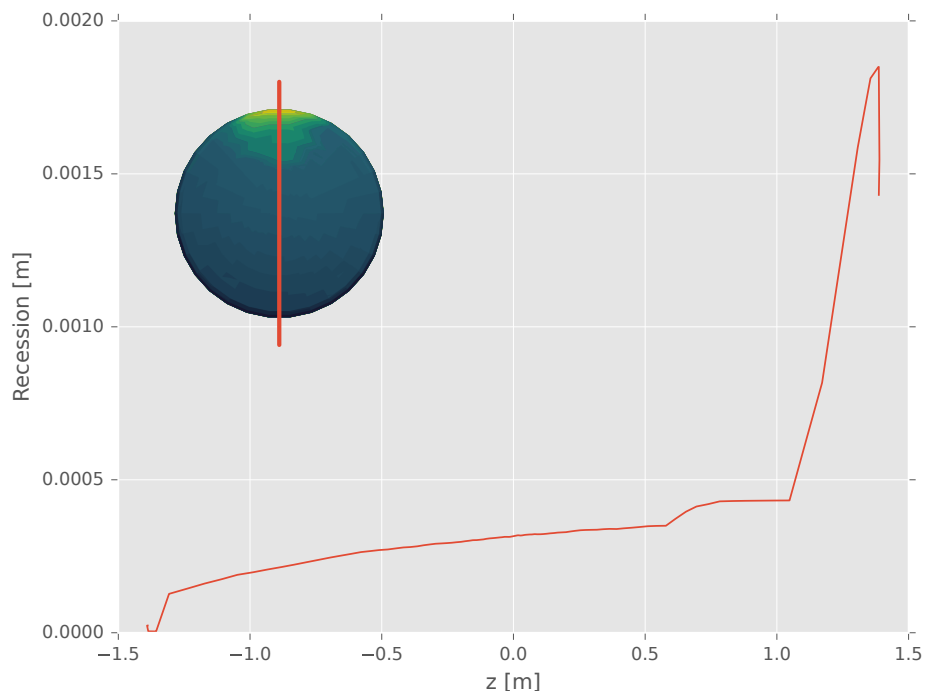


Figure 4.30: Recession of the capsule as a function of the distance from the stagnation point along the the capsule geometry at the end of the simulation. Atmospheric Re-entry Demonstrator test case simulated using HyFlow.

Fig. 4.25, Fig. 4.27 and Fig. 4.29 show the distribution of heat flux, external temperature and recession for the capsule fore-body. The first two figures show the heat flux and temperature distribution for the peak heat flux instance in the simulation; while the recession is showed at the end of the re-entry, representing therefore the maximum recession of the capsule. This value is very low, with respect to the previous case, because of the material composition and its low ablative characteristics. Aleastrasil has high insulating properties and higher density than usual ablators, making it more similar to re-usable materials.

Fig. 4.26, Fig. 4.28 and Fig. 4.30 represent heat flux, external temperature and recession trends on a section of the capsule passing through the forebody centre and the stagnation point. The small image on the top left of these figures show where the trend is plotted. As for the Stardust case studied with HyFlow, a coarser mesh was used in the simulation. No comparative trends are represented in these figures because this data was not present in literature. The first two figures show the values for the peak heat flux time in the trajectory while the last one represents the values at the end of the re-entry. These figures highlight the fact that the maximum values correspond to the stagnation point that, in the case of a consistent angle of attack, is moved from the centre of the capsule forebody to the shoulder. This variation of the maximum heat flux location is very important for the design of the TPS because it influences the TPS structure, changing the maximum thickness and the location of the different ablative materials forming it.

4.2 Planetary entry

To test the capability of the code to generate entries through an atmosphere characterized by a different composition and physical properties than that of the Earth, a Martian entry was selected. Since HyFlow only had Earth atmosphere aerodynamic data implemented, it was necessary to create and add a different aerodynamic model for the planet atmosphere.

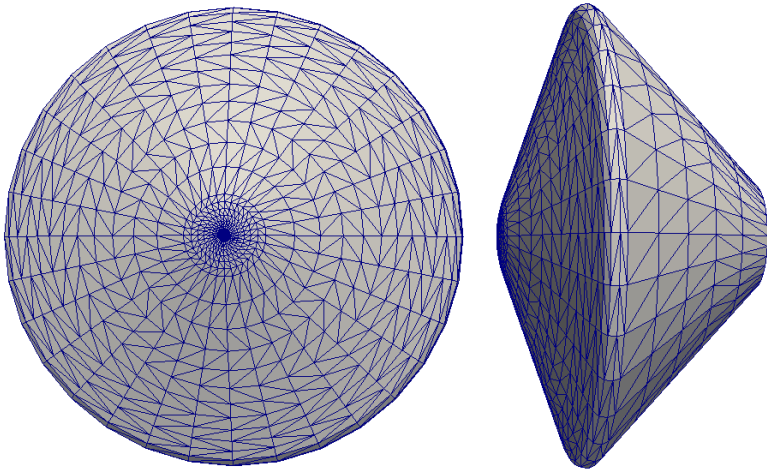


Figure 4.31: Front and side representation of the Pathfinder geometry as it is utilised for the simulations in HyFlow.

4.3 The Pathfinder Martian Entry

The Pathfinder probe performed a successful landing on Mars' surface in 1997. Mars' and Earth's atmospheres differ greatly from one another, both in their composition and in their physical characteristics. This simulation was performed using HyFlow as the aero-thermodynamic code. HyFlow has the ability to simulate any atmosphere given the right properties, Table 4.3 summarizes the characteristics employed by the code to perform the simulation and the values selected to describe the Martian atmosphere. Table 4.4 contains the external characteristics used by HyFlow to perform the simulation.

Table 4.3: Martian atmosphere properties used in HyFlow.

| γ | c_{pv} | R | P_r |
|----------|----------|-----|-------|
| 1.33 | 730 | 192 | 1 |

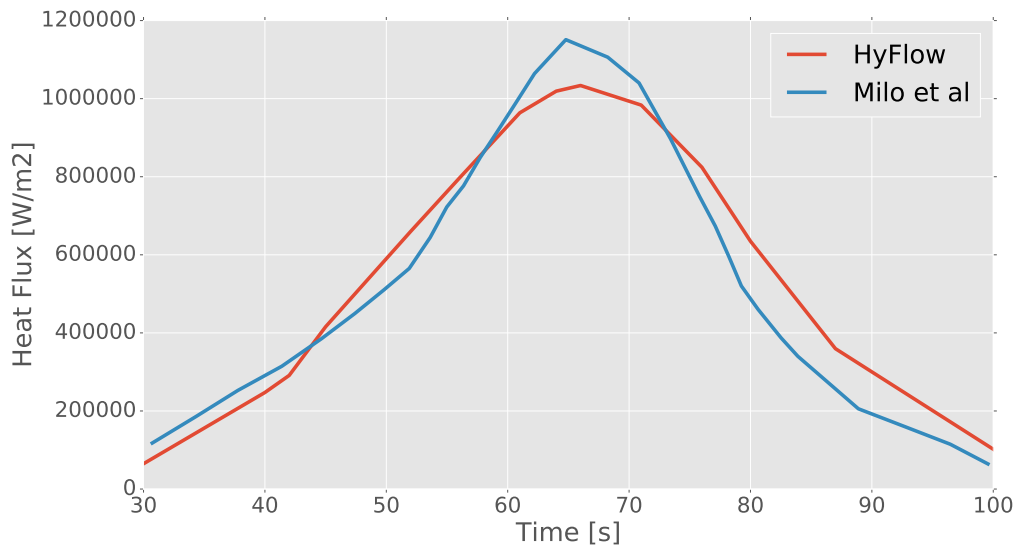


Figure 4.32: Comparison of the heat flux as a function of time at the stagnation point between the estimation presented by Milos *et al* [32] and the values calculated by the code herein presented.

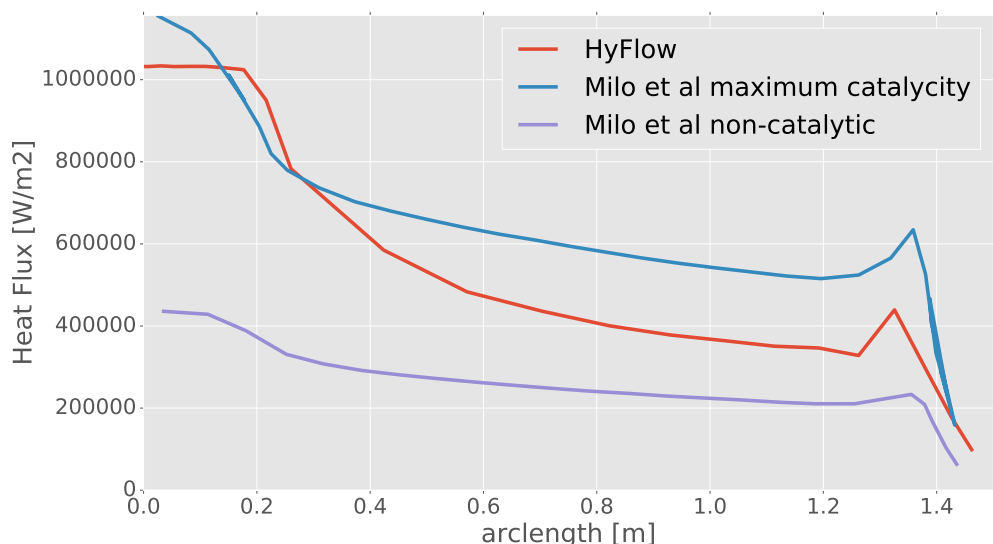


Figure 4.33: Heat flux profiles along the capsule as presented in Milos *et al* [32] and as evaluated during this study for the time of peak heat flux (66 s).

Table 4.4: Time instances for the Pathfinder Martian entry trajectory.

| Time [s] | Altitude [km] | Velocity [m/s] | Temperature [K] | Density [kg/m ³] |
|----------|---------------|----------------|-----------------|------------------------------|
| 30 | 85.000 | 7504 | 105 | 6.74E-07 |
| 40 | 71.109 | 7496 | 122 | 7.24E-06 |
| 42 | 68.469 | 7490 | 129 | 1.01E-05 |
| 45 | 64.599 | 7472 | 112 | 2.10E-05 |
| 52 | 56.026 | 7364 | 143 | 5.76E-05 |
| 56 | 51.445 | 7242 | 157 | 9.28E-05 |
| 61 | 46.089 | 6994 | 162 | 1.69E-04 |
| 64 | 43.097 | 6774 | 168 | 2.31E-04 |
| 66 | 41.204 | 6596 | 169 | 2.80E-04 |
| 71 | 36.854 | 6041 | 173 | 4.38E-04 |
| 76 | 33.082 | 5333 | 170 | 6.68E-04 |
| 80 | 30.489 | 4717 | 175 | 8.53E-04 |
| 87 | 26.760 | 3704 | 179 | 1.24E-03 |
| 100 | 21.848 | 2299 | 184 | 2.01E-03 |

The capsule geometry is illustrated in Fig. 4.31, the forebody heat shield is formed by the SLA-561V material and has a thickness of 1.9 cm. The rest of the heat shield is composed of different materials and thicknesses; considering that studies for the leeward surfaced were not found in literature, it was decided to use the more simplified case and utilize a single material model and the same TPS thickness for the entire geometry. Nevertheless, as stated before, ARC has the ability to handle different thicknesses and materials on different geometry positions. The SLA-561V thermo-ablative model was created utilizing the data presented by Strauss [66]; unfortunately, this is a single component model and it does not report in great detail the various thermal characteristics; for these reasons a small increment in the results error is to be expected. The evaluations used to compare against, were produced by Milos *et al* [32] using the GIANTS code, a CFD tool, for the external flux evaluations; while the thermal response of the heat shield was produced using different models, in particular these were developed at Applied Research Associates (ARA), NASA Ames Research Center(ARC), and Lockheed Martin Astro-nautics(LMA). The CMA code was used for the ARA model, both FIAT and CMA were employed for the ARC model and REKAP code was used for the LMA model [32].

Fig. 4.32 shows the heat flux for the stagnation point as a function of time, as it was

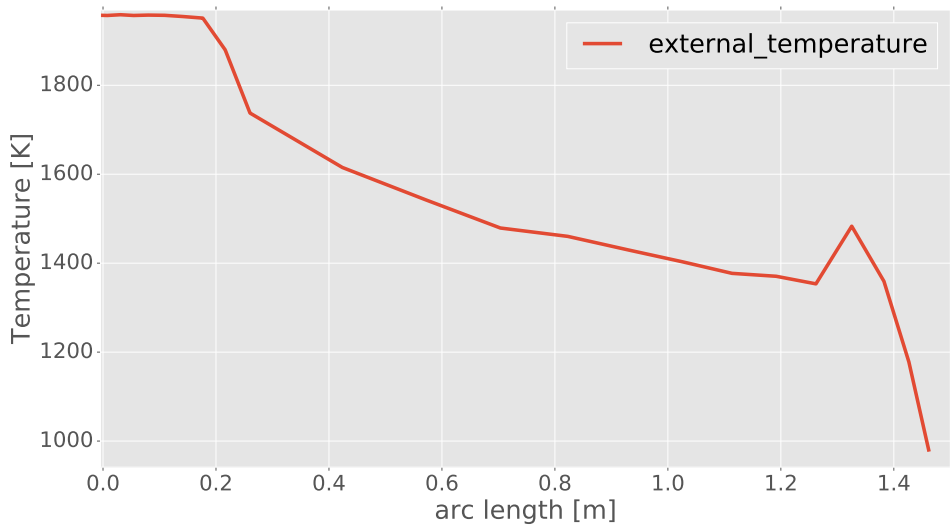


Figure 4.34: External temperature profiles along the capsule as evaluated during this study for the time of peak heat flux (66 s).

evaluated by HyFlow and by Milos *et al* [32]. The two curves are in good agreement even if HyFlow heat flux peak is slightly inferior than the GIANT one. This small discrepancy was expected due to the use of a reduced order code for the environmental simulation in contrast with a CFD tool. In the case of Earth re-entries, HyFlow overestimated the external heat flux while, in this case, it underestimates it. This is because Mars and Earth atmospheres differ greatly. In particular, Earth entries are characterized by very high fluxes and elevated temperatures; in these conditions the flux chemistry has an important effect and, neglecting it, brings to an overestimation of the flux. Mars' atmosphere has a lower density therefore, Martian entries are characterized by lower fluxes and external temperatures. In these conditions, the flux chemistry has a lower impact and neglecting it does not lead to an overestimation of the heat flux value. Although some small differences are present, the two trends are quite close and the approximated heat flux can be used to generate the thermal simulations calculated by ARC. If, for any reason, conservative results were to be preferred, it is possible to multiply the evaluated heat flux by a desired safety factor, similarly to the coefficient introduced in Earth's atmosphere simulations. Fig. 4.33 illustrates the heat flux profile at the time of peak heat flux, as evaluated by the current approach and as calculated by

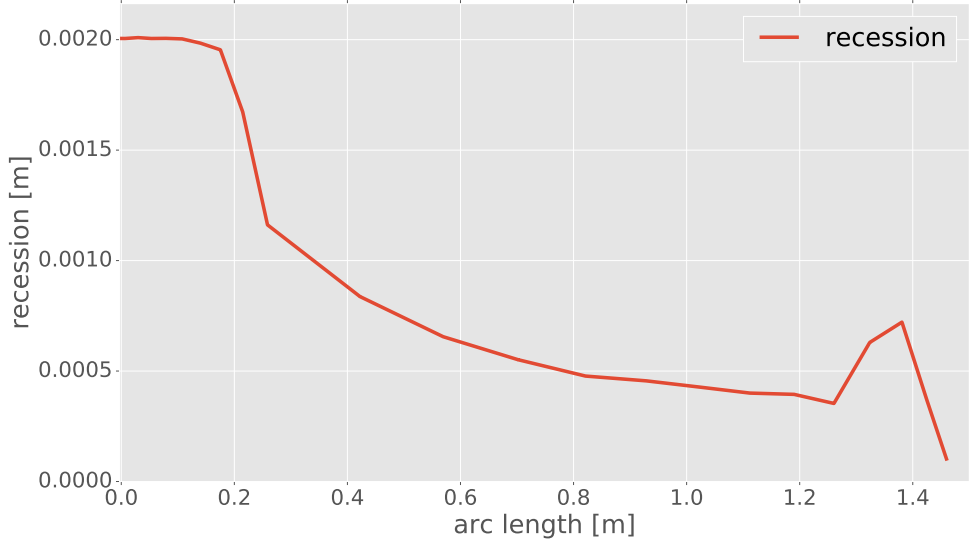


Figure 4.35: Recession profiles along the capsule as evaluated during this study at the end of the simulation.

the reference paper for the case of maximum catalycity and the non catalytic case. The methodology used presents results inside these two extreme cases. The differences in the location of maximum value for the shoulder portion of the capsule, can be attributed to the mesh. HyFlow is highly dependant on the mesh size and a more refined mesh could generate a more precise estimate of the shoulder heat flux; however, it was decided not to increase the number of mesh panels for two main reasons. Firstly, because the shoulder local maximum locations are less than 0.1 m apart on a forebody of diameter 2.8 m and secondly, to avoid an increase in the simulation time, since one of the aims of this study is to demonstrate that it is possible to produce sensible evaluations of a three-dimensional atmospheric entry without a great computational effort. Fig. 4.34 shows the external temperature values on the capsule at the time of peak heat flux during the trajectory. The temperature and the heat flux have a very similar trend for the reason that the former is influenced by the latter. Lastly, the total recession of the capsule is shown in Fig. 4.35. As expected, this property presents a very similar trend to the temperature and the heat flux because, it depends on both of those parameters. Three-dimensional representations of the graphs shown in this section are present in

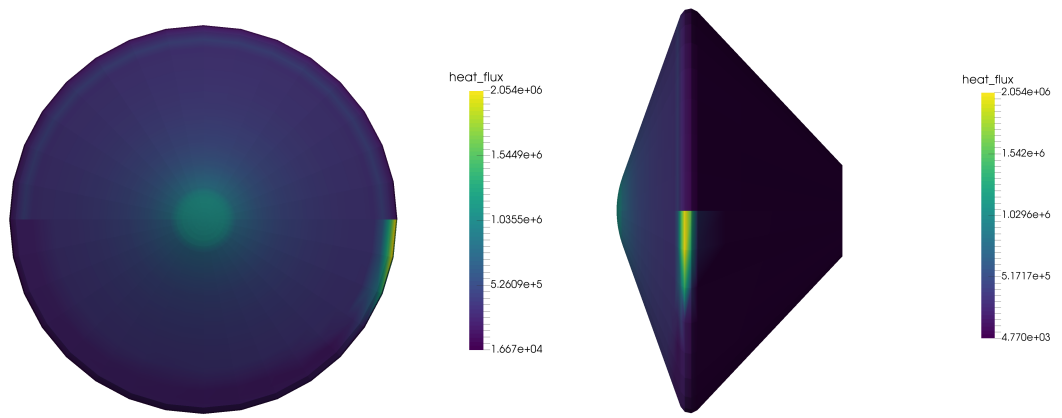


Figure 4.36: Three-dimensional representations of the heat flux [W/m^2] at the time of peak heat flux (66 s) for the geometry surface. The upper half of the image represents the axi-symmetrical case while the lower part illustrates the case with an angle of attack equal to 15 degrees.

the next section in comparison with a different test case.

The test case herein presented is axi-symmetrical thus, a simpler two-dimensional evaluation can produce the same knowledge regarding the TPS behaviour as a three-dimensional one; nevertheless, real atmospheric entries are not perfectly axi-symmetric. To the author's knowledge, fully coupled three-dimensional simulations of the external environment and the thermo-ablative internal material behaviour are extremely difficult to find in literature, due to the computation time required. A non axi-symmetrical case can be simulated by the presented approach with the same simplicity of an axi-symmetrical case. The following section illustrates the changes that the introduction of an angle of attack can produce in the heat flux and temperature trends and why it is important to be able to simulate it.

4.3.1 Non axi-symmetrical case

One of the strengths of the proposed approach is the ability to produce three-dimensional approximated results. Unfortunately, to the authors knowledge, there are no three-dimensional evaluations of the Pathfinder entry in literature. The results that have been used in the previous section to compare against, were generated simulating in two

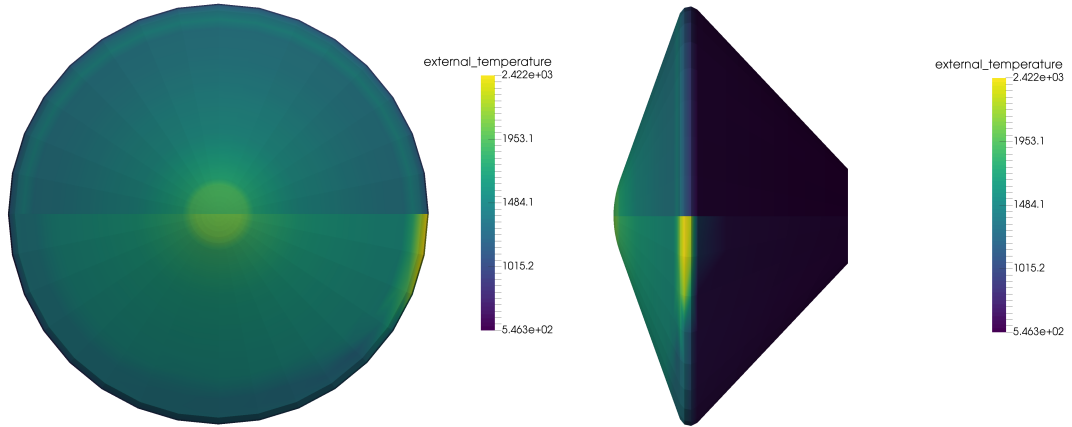


Figure 4.37: Three-dimensional representations of the external temperature [K] at the time of peak heat flux (66 s). The upper half of the image represents the axi-symmetric case while the lower part illustrates the case with an angle of attack equal to 15 degrees.

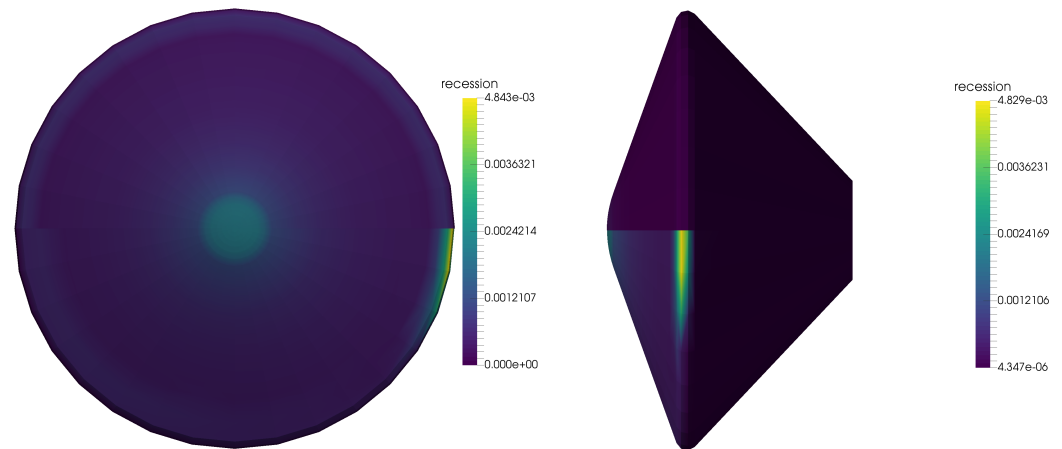


Figure 4.38: Three-dimensional representations of the suface recession [m] at end of the trajectory for the geometry surface. The upper half of the image represents the axi-symmetric case while the lower part illustrates the case with an angle of attack equal to 15 degrees.

Chapter 4. Three-dimensional test cases

dimensions an axi-symmetrical test case. However, most capsules entering a planetary atmosphere do not have their axis of symmetry perfectly parallel to the velocity vector for the entire duration of the trajectory. The difference of angle, in this case, could lead to some serious consequences if the leeward surface, which is shadowed in the axi-symmetric case, is exposed to more elevated heat fluxes than in the nominal case. To illustrate how small changes can influence the simulations, this section describes the results of a non axi-symmetric Pathfinder Martian entry and highlights the differences between this case and the one previously presented. To do so an angle of attack equal to 15 degrees was introduced.

Fig. 4.36 shows the comparison between the axi-symmetrical and the non axi-symmetrical case heat flux on the capsule surface, at the time of peak heat flux. It is highlighted how, in the second case, the shoulder has a consistent increase of heat flux with respect to the nominal case. In the Pathfinder capsule, the shoulder is still adequately protected by the SLA-561V material of large enough thickness. Fig. 4.37 and Fig. 4.38 illustrate that both external temperature and surface recession present the same increase in the shoulder as the heat flux. The capsule in study has a back heatshield quite different from the forebody one. In particular, it has an ablative material used for lower heat fluxes and a heatshield thickness inferior with respect to the forebody. If the heat flux values for this surface increase excessively, it is possible that the TPS becomes not able to properly protect the spacecraft. That is the reason why it is important to perform simulations able to evaluate what happens when a small angle of attack is present during the entry trajectory.

The approach herein presented always performs three-dimensional evaluations of the atmospheric entry; therefore, the symmetry of the flux or the lack of this symmetry does not influence the computational time. Consequently complex, non symmetric cases are just as easy to simulate as symmetric ones.

4.4 Discussion

The coupling methodology using ARC and different aero-thermodynamic models has been used to simulate both Earth’s and Martian atmosphere entries. The heat flux values along the trajectory have been evaluated and the ablative TPS behaviour has been computed.

The comparisons presented in this document show that the approach used produces results in good agreement with evaluations generated with more complex tools; especially for the evaluation of the heat flux and the external temperature as function of time for the stagnation point and its surrounding area. This part of the geometry is the most challenging one for the TPS because it must withstand the maximum heat load and the highest temperatures. The profiles of heat fluxes and temperatures on the entire geometry show non-negligible discrepancies between the methodology herein presented and commercial coupled methodologies for some of the simulations. This could be problematic if a higher accuracy is desired; however it was not considered troublesome in this case, because of the target phase of the design this methodology was thought for.

The strength of this procedure is, unequivocally, the ability to produce three-dimensional estimates of the entire TPS behaviour with a short running time (minutes instead of hours or days). The weakness is the inability to reach the accuracy of the more computationally expensive methodologies, used in this chapter to compare against.

Moreover, the discrepancies in the TPS behaviour are not caused by how the methodology was generated, *i.e.* the lack of thermal conduction among adjacent points and, more in general, of three-dimensional effects. Indeed, the discrepancies are also present in the heat fluxes profiles calculated by the aerodynamic models. The fact that the same discrepancies are present in the heat flux trend and in the temperature trends, shows that the error is introduced by the aerodynamic codes and just carried through in the ARC results. The use of a more accurate aero-thermodynamic program would increase the accuracy of the ARC generated results. In this case, the total time needed

Chapter 4. Three-dimensional test cases

for the whole simulation would increase, due to the use of a more computationally demanding aero-thermodynamic tool. However, if the coupled methodology explained in chapter 3 is implemented, it would still be less computationally demanding than the use of fully two and three-dimensional thermal response codes. Therefore still having a lower run time than commercial coupled methodologies.

In conclusion, it can be said that the method herein presented can be used in the preliminary phases of the TPS design, when a great number of different simulations are required and fast run time is preferred to higher accuracy. In addition, this chapter proves that ARC is a versatile tool that can be used with different aerodynamic models.

Chapter 5

Permeability

This chapter describes the part of the thesis focused on improving the characterization of ablative materials. As it is clear from the previous chapters, the data regarding the thermo-physical properties of the ablative material is of fundamental importance when simulating the TPS behaviour.

This set of properties is what constitute the material model used by ARC and other thermal response tools. The more precise this set of data is, the more accurate the results are likely to be. In particular, it is crucial to have an adequate knowledge of the influences that changes in the external environment have on the different thermal properties. During an atmospheric entry, the external flow characteristics experience great variations, passing from the high-altitude to the low altitude environment; specifically, external temperature and pressure vary considerably. Moreover, the changes inside the material may exceed the ones of the external environment: e.g. the temperature of the material can vary from lower than $200K$ to more than $3000K$ during a single entry trajectory. This generates variations in the material properties which are not negligible and which introduce notable errors in the results if not taken into account.

Of the thermo-chemical characteristics needed by ablative simulating tools, some, such as the thermal conductivity and the specific heat flux, are usually well investigated for a variety of temperature and pressure values; some others are, instead, considered to be temperature or pressure invariant. This chapter focuses on one of those properties which is less investigated during ablative material characterization campaigns: the

permeability. This property is critical when precisely simulating the TPS behaviour because it influences the pyrolysis gas behaviour and the time required by the gas to reach the external surface. The ultimate aim of this specific activity is to produce better and more accurate material models, to be used in ablative response programs like ARC. The study is based on the investigation of two ablative materials, one cork based and one carbon based [67]. The methodology used to generate the results is an extension of the commonly performed Direct Simulation Monte Carlo (DSMC) approach and was conceived by White *et al* [68] while taking part in the ABLAMOD project, an European funded project focused on the characterization and simulation of ablative materials. The novelty introduced by the author of this thesis is the fact that, the technique was applied outside its usual domains to produce evidence that the permeability should not be considered as a constant property. Instead, it presents large variations in its value due to changes in pressure and temperature.

5.1 Methodology

The average permeability of a porous medium in a compressible fluid is determined by:

$$K = \frac{\dot{\Omega} \mu L}{\Lambda} \frac{2P_{out}}{P_{in}^2 - P_{out}^2} \quad (5.1)$$

in which $\dot{\Omega}$ is the outlet volumetric flow rate of the fluid, μ is the fluid viscosity, L is the length of the sample in the flow direction, Λ is the cross-sectional area, P_{in} is the pressure at the inlet and P_{out} is the pressure at the outlet. The Knudsen number in a porous medium is given by:

$$Kn = \frac{l}{D} \quad (5.2)$$

where l is the mean free path of the flow, defined as the average length a molecule has to be in motion before experiencing a collision, and D is the representative physical length scale, which in this case is the mean diameter of the pores. The Knudsen number provides an indication of the degree of rarefaction of the flow field, which is essential to

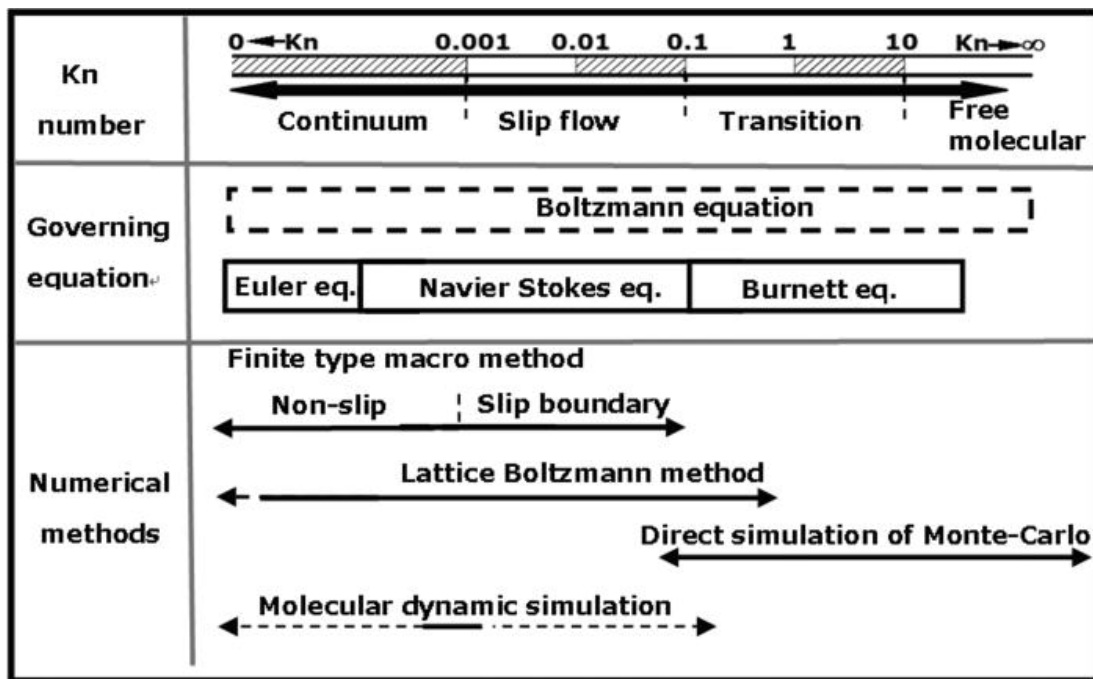


Figure 5.1: Representation of the governing equations and the numerical methods used to describe and simulate a flow depending on Knudsen number regime. Credit: heattransfer.asmedigitalcollection.asme.org.

accurately select the methodology to be applied to better describe the physical reality. The Knudsen number describes the likelihood of intermolecular collisions and therefore, it represents how the flow behaves. As this number increases, the number of collisions between particles decreases, therefore non-equilibrium effects become dominant. As illustrated by Fig. 5.1 the Knudsen regimes can be divided in:

- $Kn \leq 0.001$: continuum regime. Can be described using Navier-Stokes equations.
- $0.001 \leq Kn \leq 0.1$: slip flow regime. Can still be described using Navier-Stokes equations.
- $Kn \geq 0.1$: transition and free molecular regime. Cannot be simulated using Navier-Stokes equations. Other methods, such as Boltzmann equation, must be used.

During a re-entry, the spacecraft crosses all of the above described regimes, therefore, different equations and numerical methods are used to describe the entire trajec-

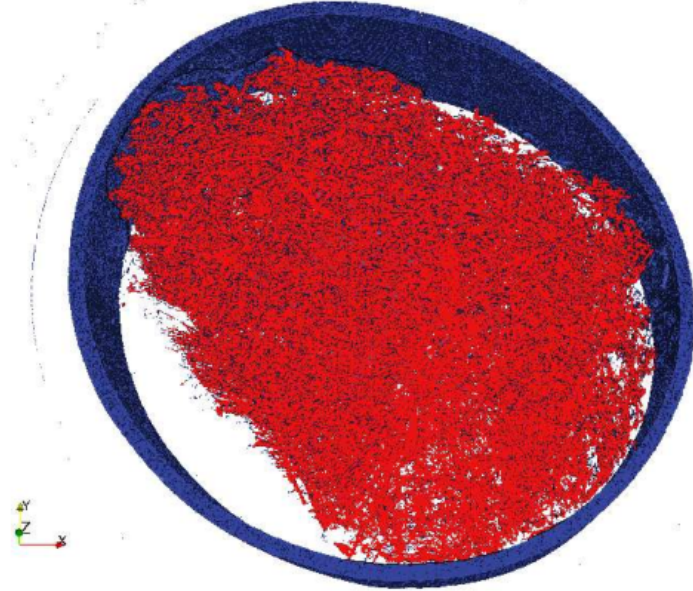


Figure 5.2: Image of the micro-computed tomography scans performed at the Austrian Foundry Research Institute on the ASTERM material after the removal of air [67]. The red cubes represent the ablative material while the blue part represents the straw used to contain the material during the scan.

tory [63]. The rarefied and transitional regimes, in those cases, are caused by the low atmosphere density and the high value of the mean free path. However, an elevated Knudsen number can be caused not only by a high mean free path, but also by a small representative physical length scale. In the case of the pores inside the materials in study, the representative physical length scale is extremely small; in fact, the pores diameters are measured in micrometers.

During significant parts of an atmospheric entry the mean free path has the same order of magnitude of the pores identified in the materials in this study, this means that the continuum-flow assumption is not valid and commonly used tools, such as CFD programs, cannot be employed to produce accurate evaluations. The transitional regime, where l and D are of similar magnitude, can be studied applying DSMC method [69] [70].

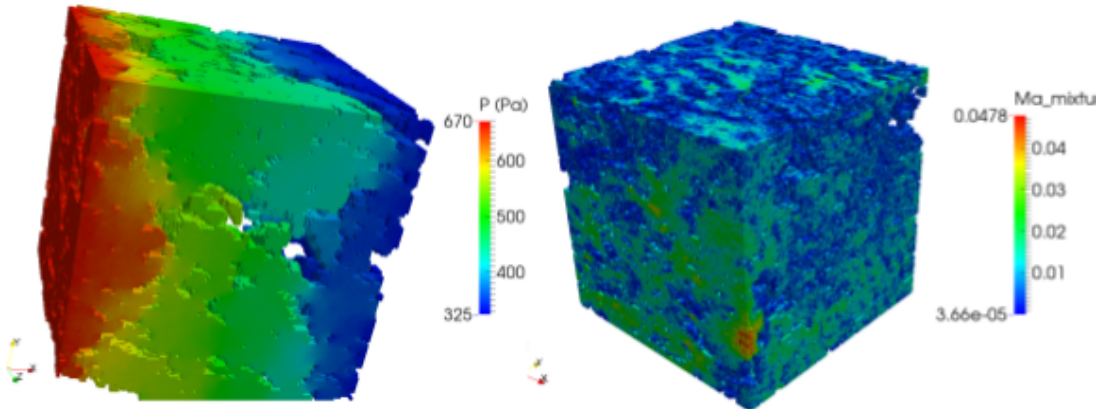


Figure 5.3: Representation of a 100^3 voxel section of the micro-computed tomography scans: the figure on the left shows the pressure contours while the image on the right shows the Mach contours.

The DSMC methodology is the pre-eminent technique to generate simulations in those flow fields where the Navier-Stokes-Fourier (NSF) equations cannot be used. In such cases, which are characterized by a high level of gas rarefaction ($Kn \geq 0.01$), the Boltzmann equation has to be utilized. Unfortunately, the Boltzmann equation in its full form is computationally impracticable and is also highly time consuming. Firstly formulated by Bird [70], the DSMC technique avoids solving the Boltzmann equation and opts for a representative statistical solution. In a DSMC simulation every particle represents a considerable number of atoms or molecules of the real gas. Mimicking the physics of the real gas and using a statistically representative number of particles in time and space, the method produces reliable results. In particular, the physics of the problem is described by decoupling the particle behaviour at the time of collision with another particle or with the simulation boundaries, from its motion. Specifically the motion is evaluated deterministically while the collisions are dealt with stochastically. The DSMC technique has the ability to calculate solutions of very complex flows involving chemical reactions, ionization and high degrees of molecular non-equilibrium [69]. It can be used in a great variety of space applications, in particular, flows in upper atmosphere, such as upper atmosphere studies of entry vehicles and analyses of satellites in LEO, and planetary science, such as studies of small bodies atmospheres. During the course of the ABLAMOD project, the DSMC approach was employed to study the

Chapter 5. Permeability

behaviour of gas inside a porous medium extending, therefore, its capability to simulate flows characterised by internal flow-paths that are highly complex, contorted and interconnected.

The main outcome of the simulations is the computation of the outlet volumetric mass flow rate of the fluid; from this parameter the volumetric flow rate is calculated and utilized in Eq. 5.1 for the permeability evaluation.

$$\dot{\Omega} = \frac{\dot{m}}{\rho_{out}} \quad (5.3)$$

The DSMC method has a high computational cost and, in some cases, it requires a high performance computer to complete the simulations in an acceptable time scale. Despite this inconvenience, it is still advantageous to use this method instead of performing the great number of empirical tests to evaluate the permeability values for the numerous external characteristics encountered by the TPS during an atmospheric entry or a plasma test.

At the beginning of a DSMC simulation the computational domain is divided into cells. The mesh is then populated with particles; each of these particles represents a number of real particles in the flow equal to a finite, pre-selected number. The cross section of the DSMC particles is equal to the one of the real particles multiplied by the pre-selected number; in this way the real and the simulated flow are equivalent. The particles are allowed to change position from one point of the mesh to another depending on their velocity.

For every time step, the basic calculations are divided in three different steps. In the first step, the movements of the molecules are computed. The second step consists in the collision sampling: a stochastic algorithm defines the collisions between the particles. In the third stage the interactions of the molecules with the simulation boundaries (surface, inflow and outflow of particles) are computed. At the end of every time step, new chemical properties, of any particle that took part in a collision, are calculated; the new positions and velocity of all of the particles are determined and the calculations for the next time step can start. This methodology gives a statistical representation

Chapter 5. Permeability

of the various physical phenomena that are taking place within the flow domain. All the numerical simulations in this study were performed employing a version of the `dsmcFoam` code [71], modified by researchers at the University of Strathclyde. In this program, the energetics of intermolecular collisions for polyatomic species are generated applying the variable hard sphere (VHS) model [69], and the Larsen-Borgnakke model is utilized to re-distribute energy between the translational and rotational modes of the particles after the collisions [69]. In good DSMC practice, the mesh cell size is imposed to be smaller than the local mean free path of the particles, in order to promote the nearest-neighbour collisions to accurately capture a stochastic representation of the reality and therefore to generate adequate estimates of the transport of mass, momentum, and energy within the flow. Given the computational burden that this rule imposes on the calculations, it has sometimes been the case that it has had to be relaxed in the work presented here. In these cases, additional studies were carried out to evaluate the errors that were introduced into the results by using a larger cell size than would have been ideal.

The simulations were performed on two materials: a cork-phenolic ablative material named TPS3L (produced by Amorim Cork Composites) and a carbon-phenolic material named ASTERM (produced by Airbus Defence and Space). A third material was selected for the analyses, however, after a few trials it was found that its inner pores were closed and lack the interconnects necessary to allow the gas to move from one part of the material to another; thus the permeability is zero for all external conditions and DSMC simulations are superfluous. The geometries utilized were created from the micro-computed tomography (μ CT) scans performed at the Austrian Foundry Research Institute (OGI). These scans consist of three-dimensional cubic voxels that contains both the material and the air surrounding it. The air is removed from the scan applying a density threshold: all cubes characterized by a density lower than the threshold value are considered to be air and are removed from the image. Fig. 5.2 illustrates the sample of one of the materials after the removal of air; the blue material surrounding the ablator is the drinking straw used to contain the sample while performing the μ CT scan. The geometry in Fig. 5.2 is too large to be used in a DSMC simulation therefore

portions of the scans were cut out and selected as the simulation geometries. Particular attention was paid in order to make sure that the selected portions were representative of the entire material, thus that they had the same porosity as the entire sample. Four different geometries, one for each material in both virgin and charred state, were selected at the end of this process. An example of these regions is shown in Fig. 5.3; the portions in this figure are made of 100^3 voxels while the majority of the geometries utilized for the simulations where formed by 50^3 voxels.

5.1.1 Novelty in the methodology used

In this study, the DSMC method was employed outside its normal boundaries in order to obtain results for a greater variety of external conditions without using excessive computational time. Because of this decision, particular attention is devoted to analyse the errors introduced by moving away from the conventional DSMC rules. Good DSMC practice says that the number of particles inside one grid cell should be around 20 and the mesh cell size should be smaller than the local mean free path. In the case of this study this rule has been applied whenever possible, however, in some of the cases it was impossible to complete the simulation in a reasonable amount of time without neglecting this guideline. It is clear that the cell size needed when the pressure is equal to 662 Pa is considerably bigger than the cell size for a simulation with a pressure of $1.5 \times 10^5\text{ Pa}$ when all other properties remain constant. The lower pressure case requires a couple of days to run on an HPC computer facility using 48 cores, the higher pressure case would easily require weeks if not months to complete the simulation. Since the study is considering almost a hundred different simulations, it is clear that it would have been impossible to precisely follow the guideline and still complete all of the simulations needed. Another option was to introduce a different computational tool for those simulations that are characterized by a lower value of Knudsen number. This option was discarded because using the same tool for the entire set of simulations would give continuity in the results and the ability to compare the results with each other. It is clear that the farther we move from DSMC good practice the higher the error introduced is. However this still remains a novel and useful study because it estimates the changes in permeability due

Table 5.1: Composition of the fluid utilized during the simulation in mole fraction.

| Species | Mole Fraction |
|----------|---------------|
| H_2 | 0.485 |
| CO | 0.276 |
| N_2 | 0.157 |
| NO | 0.0522 |
| C_2N_2 | 0.0293 |

to pressure and temperature variations, a physical property which is usually assumed constant for the entire re-entry trajectory. This study shows that this assumption is far from reality and, if not taken into account, can introduce non-negligible changes in the simulations results. In particular, the permeability value influences the blocking phenomenon in which the pyrolyses gas exits the material and partially blocks the incoming hot air. Precisely determining the blocking effect is essential to have an accurate evaluation of what portion of the heat flux actually reaches the material surface and influences the TPS behaviour. The fluid selected to perform the simulation is a gas mixture whose composition is shown in Table 5.1. Other information related to the gas such as the dissociation reaction of the pyrolysis gas, exchange reactions and Arrhenius parameters, the Hard Sphere parameters for the individual gas species are contained in the paper written by White *et al* [68].

5.2 Results: permeability dependence on external conditions

The changes in permeability value due to pressure and temperature variations were investigated separately one from another to better comprehend their effects on the materials.

5.2.1 Pressure dependency

During the latter stages of re-entry and during a ground-based plasma test the ablative material is exposed to much higher pressures than those at higher altitudes. In order to evaluate the effect of background pressure on the permeability of the materials, a large

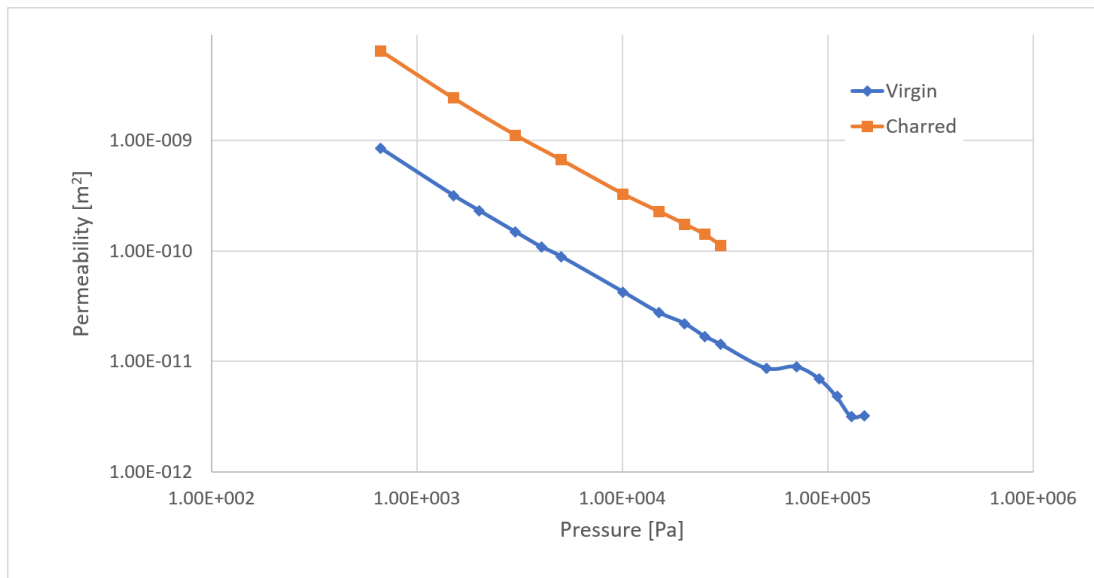


Figure 5.4: Permeability Pressure trend for the virgin and charred state of the carbon material.

Table 5.2: Permeability dependence upon pressure for the virgin state of the carbon material.

| Inlet Pressure [Pa] | Temperature [K] | Permeability [m^2] |
|---------------------|-----------------|------------------------|
| 662.33 | 1500 | 8.57×10^{-10} |
| 1500 | 1500 | 3.21×10^{-10} |
| 2000 | 1500 | 2.34×10^{-10} |
| 3000 | 1500 | 1.50×10^{-10} |
| 4000 | 1500 | 1.10×10^{-10} |
| 5000 | 1500 | 8.99×10^{-11} |
| 10000 | 1500 | 4.32×10^{-11} |
| 15000 | 1500 | 2.79×10^{-11} |
| 20000 | 1500 | 2.22×10^{-11} |
| 25000 | 1500 | 1.71×10^{-11} |
| 30000 | 1500 | 1.44×10^{-11} |
| 50000 | 1500 | 8.72×10^{-12} |
| 70000 | 1500 | 8.97×10^{-12} |
| 90000 | 1500 | 7.07×10^{-12} |
| 110000 | 1500 | 4.86×10^{-12} |
| 130000 | 1500 | 3.18×10^{-12} |
| 150000 | 1500 | 3.25×10^{-12} |

Chapter 5. Permeability

Table 5.3: Permeability dependence upon pressure for the charred state of the carbon material.

| Inlet Pressure [Pa] | Temperature [K] | Permeability [m^2] |
|---------------------|-----------------|------------------------|
| 662.33 | 1500 | 6.59×10^{-9} |
| 1500 | 1500 | 2.45×10^{-9} |
| 3000 | 1500 | 1.14×10^{-9} |
| 5000 | 1500 | 6.78×10^{-10} |
| 10000 | 1500 | 3.33×10^{-10} |
| 15000 | 1500 | 2.31×10^{-10} |
| 20000 | 1500 | 1.77×10^{-10} |
| 25000 | 1500 | 1.43×10^{-10} |
| 30000 | 1500 | 1.14×10^{-10} |

number of simulations were performed over a range of pressures. In these simulations, the inlet pressure was increased continuously up to the value of 150 kPa for the virgin state of the materials and 30 kPa for the charred state; in all cases the difference in pressure across the sample was kept constant in order to allow proper comparison among the entire set of results.

Table 5.2 and 5.3 and Fig. 5.4 show how the permeability of the carbon based material is influenced by the background pressure.

The results show that the permeability of the material decreases quite dramatically as the background pressure is increased; indeed, Table 5.2 and Table 5.3 suggest that, as expected, considering the permeability as constant property could lead to large errors when evaluating the performance of the ablative material under practical conditions. The pyrolysed state of the material has a higher permeability than its virgin state. After ablation the density of the material is decreased which results in an increase in porosity and a consequent increase in the material total void volume. In these circumstances it is expected that an increased flow rate would result due to the ability of the gas to more easily pass through the material.

The behaviour of the cork material mimics the carbon one, as it can be seen in Table 5.4 and 5.5, and in Fig. 5.5. A large influence of the background pressure on the permeability of the material in both its virgin and charred state is demonstrated by the DSMC simulations.

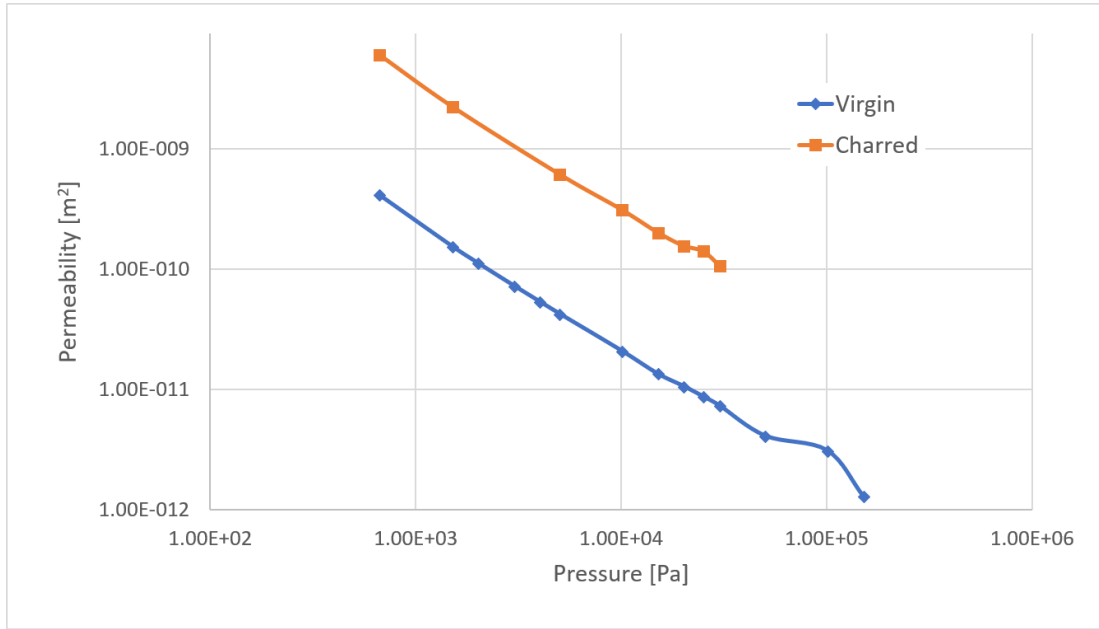


Figure 5.5: Permeability-Pressure trend for the virgin and charred state of the cork material.

Error Analysis

Estimating the influence of pressure on the permeability is a challenging task even for the DSMC approach. This is primarily because the pressure changes cause large variations in the mean free path of gas particles as they travel through the porous medium. When the background pressure is increased and all of the other characteristics of the simulations are kept constant, the mean free path of the flow decreases according to:

$$l = \frac{1}{\sqrt{2\eta\pi d^2}} \quad (5.4)$$

where

$$\eta = \frac{P}{k_B T} \quad (5.5)$$

Fig. 5.6 and Fig. 5.7 illustrate the significant decrease of the mean free path value caused by the pressure increase.

If good DSMC practice is observed, then the cell size within the computational mesh is usually set to be smaller than the mean free path of the gas particles. This

Chapter 5. Permeability

Table 5.4: Permeability dependence upon pressure for the virgin state of the cork material.

| Inlet Pressure [Pa] | Temperature [K] | Permeability [m^2] |
|---------------------|-----------------|------------------------|
| 662.33 | 1500 | 4.12×10^{-10} |
| 1500 | 1500 | 1.54×10^{-10} |
| 2000 | 1500 | 1.12×10^{-10} |
| 3000 | 1500 | 7.24×10^{-11} |
| 4000 | 1500 | 5.35×10^{-11} |
| 5000 | 1500 | 4.24×10^{-11} |
| 10000 | 1500 | 2.09×10^{-11} |
| 15000 | 1500 | 1.35×10^{-11} |
| 20000 | 1500 | 1.06×10^{-11} |
| 25000 | 1500 | 8.70×10^{-12} |
| 30000 | 1500 | 7.31×10^{-12} |
| 50000 | 1500 | 4.10×10^{-12} |
| 100000 | 1500 | 3.11×10^{-12} |
| 150000 | 1500 | 1.29×10^{-12} |

Table 5.5: Permeability dependence upon pressure for the charred state of the cork material.

| Inlet Pressure [Pa] | Temperature [K] | Permeability [m^2] |
|---------------------|-----------------|------------------------|
| 662.33 | 1500 | 6.01×10^{-09} |
| 1500 | 1500 | 2.23×10^{-09} |
| 5000 | 1500 | 6.13×10^{-10} |
| 10000 | 1500 | 3.13×10^{-10} |
| 15000 | 1500 | 2.02×10^{-10} |
| 20000 | 1500 | 1.57×10^{-10} |
| 25000 | 1500 | 1.41×10^{-10} |
| 30000 | 1500 | 1.08×10^{-10} |

allows nearest-neighbour collisions to be more accurately accounted for and hence better estimates of the various statistical properties of the gas to be obtained. As the mean free path decreases, so should the size of the computational cells. If the cells are made smaller, however, the number of cells that are needed to create the mesh becomes larger and the more onerous the computations is in terms of both memory and running time. The computational constraints on the simulations presented here were tight enough in practice that it was not possible to vary the cell size in conformity with good DSMC practice; indeed, the computational grid was kept the same throughout. To evaluate the sensitivity of the predicted permeability values, a limited series of

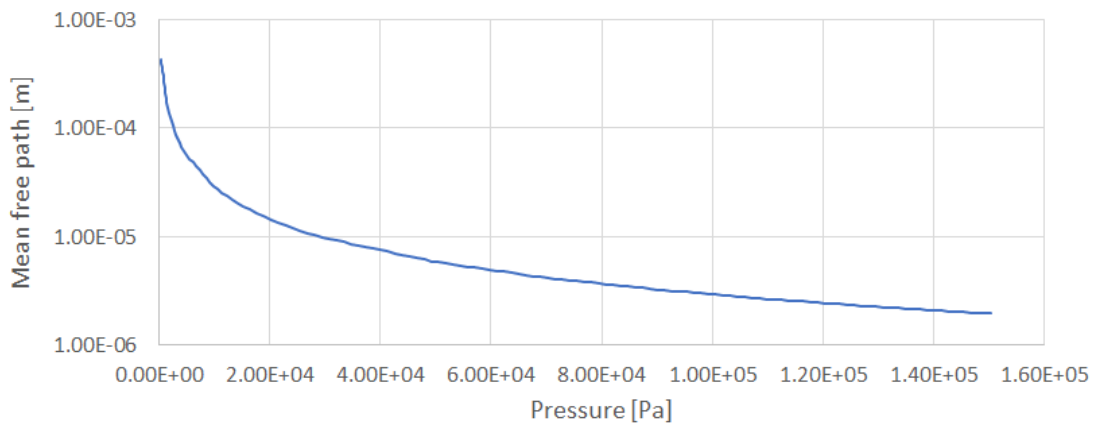


Figure 5.6: Relation between the flow mean free path and pressure.

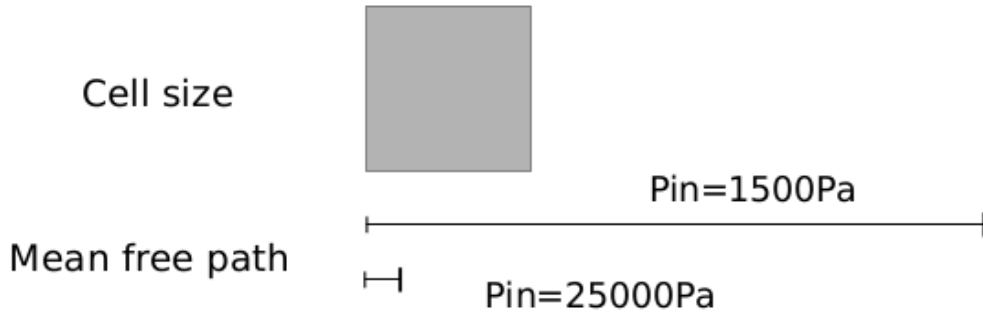


Figure 5.7: Representation of the mean free path changes due to pressure variations in comparison to the simulations cell size. P_{in} refers to the inlet pressure, which is the value used in Eq. 5.4. Figure scale 5000:1.

simulations with the same boundary conditions (pressure, temperature, mean free path) but with different cell size (equal to 1 voxel, 1/2 voxel or 1/3 voxel) were performed. These simulations allowed the error introduced by the discrepancy with good DSMC practice to be estimated by comparing the results of simulations where the cell size was bigger, smaller, or approximately equal to the mean free path. Table 5.6 shows the results obtained from this study. In the first three cases, results obtained using the 50^3 and 100^3 cell meshes are compared, while a 150^3 cell mesh was introduced for the last case (this simulation required a significantly large CPU time to run; this is the reason for only one simulation being conducted at this resolution).

Chapter 5. Permeability

Table 5.6: Absolute values of the error in the simulation results introduced by using a cell size larger than the mean free path.

| Inlet Pressure [Pa] | Cell size | Permeability [m^2] | Difference [%] |
|---------------------|-----------|-------------------------|----------------|
| 2.00E+003 | 1 voxel | 1.601×10^{-09} | |
| 2.00E+003 | 1/2 voxel | 1.601×10^{-09} | 0.04% |
| 3.00E+003 | 1 voxel | 1.028×10^{-09} | |
| 3.00E+003 | 1/2 voxel | 1.031×10^{-09} | 0.34% |
| 4.00E+003 | 1 voxel | 7.539×10^{-10} | |
| 4.00E+003 | voxel | 7.627×10^{-10} | 1.18% |
| 5.00E+003 | 1 voxel | 6.157×10^{-10} | |
| 5.00E+003 | 1/2 voxel | 5.984×10^{-10} | -2.80% |
| 5.00E+003 | 1/3 voxel | 6.026×10^{-10} | -2.12% |

The maximum difference between the cases is smaller than 3% but the error is seen to increase as the mean free path of the gas is allowed to decrease. The implication is that, the higher the background pressure, the greater the error introduced in the results can be. Given the practical impossibility of performing the simulations at the recommended cell size, especially for the larger background pressures, an extrapolation of the error trend shown in Fig. 5.8 may be applied to all the simulations performed in this study.

If the error continues to grow with the same trend for the higher pressures, the one showed in Fig. 5.8, then it will be 30% for the case run at 30 kPa and 100% for the case run at a background pressure of 150 kPa . These estimates of the error yield an important confirmation of the validity of the approach adopted here, revealing as they do that the correct order of magnitude, if not the exact value of the permeability, can be evaluated properly even in those cases where the background pressure is relatively high. These are significant results taking into account that the variations of the permeability are larger than the higher estimated error, that the permeability is usually considered constant, when simulating porous ablative material, and that few resources are employed to investigate this property, when generating the material model for new ablators.

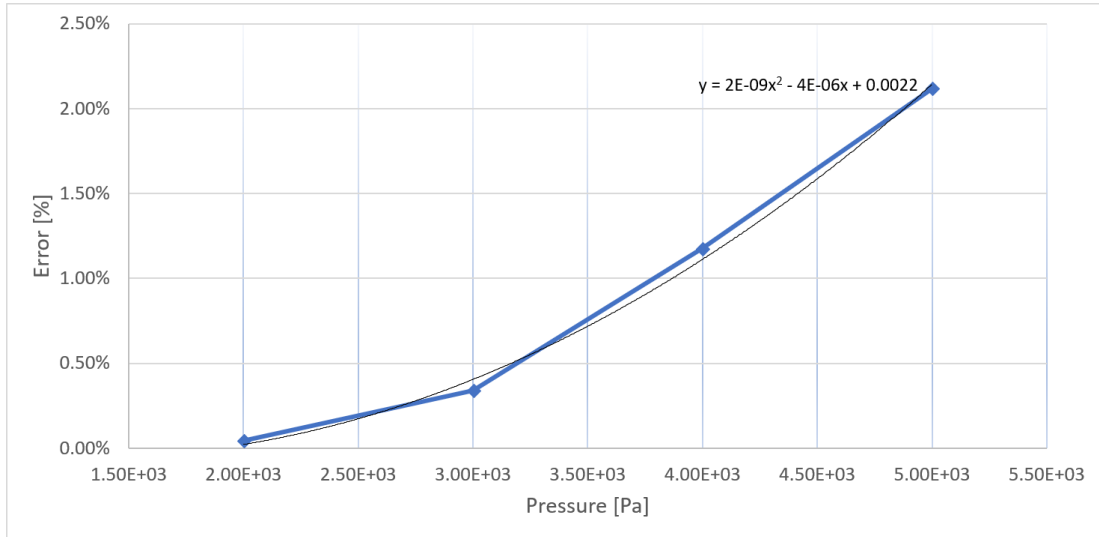


Figure 5.8: Error introduced by using a cell size larger than the mean free path and the trend line used to extrapolate the error value for different higher pressure value.

5.2.2 Temperature dependency

The variation of the material permeability with temperature is an important characteristic to be determined, if the behaviour of the system has to be properly characterised, whether it be during re-entry or in a laboratory-based plasma test. The dependency of the permeability of the carbon- and cork-based ablative materials on temperature was assessed using a similar methodology that was employed to determine the dependency of the permeability on the background pressure. In this study, the inlet and outlet pressure was kept constant for all simulations, while the temperature of the gas entering the simulation, and indeed of the material itself, was varied through a representative range. The following tables and graphs show the variation of permeability due to temperature for both materials.

Table 5.7 and 5.8 present the permeability values variations due to the changes in temperature for the virgin and the charred state of the carbon material. Fig. 5.9 illustrates the permeability trends for both states of the carbon material. In both cases the permeability values increases while the temperature increases. Table 5.9 and 5.10 with Fig. 5.10 illustrate that the permeability behaviour for the cork material show the same increase in permeability with temperature as seen for both states of the carbon

Chapter 5. Permeability

Table 5.7: Permeability dependence upon temperature for the virgin state of the carbon material.

| Inlet Pressure [Pa] | Temperature [K] | Permeability [m^2] |
|---------------------|-----------------|------------------------|
| 662.33 | 300 | 1.73×10^{-10} |
| 662.33 | 500 | 2.91×10^{-10} |
| 662.33 | 750 | 4.33×10^{-10} |
| 662.33 | 1000 | 5.76×10^{-10} |
| 662.33 | 1500 | 8.57×10^{-10} |
| 662.33 | 1250 | 7.20×10^{-10} |
| 662.33 | 1750 | 1.01×10^{-09} |
| 662.33 | 2000 | 1.15×10^{-09} |
| 662.33 | 2250 | 1.31×10^{-09} |
| 662.33 | 2500 | 1.43×10^{-09} |

Table 5.8: Permeability dependence upon temperature for the pyrolysed state of the carbon material.

| Inlet Pressure [Pa] | Temperature [K] | Permeability [m^2] |
|---------------------|-----------------|------------------------|
| 662.33 | 300 | 1.41×10^{-09} |
| 662.33 | 500 | 2.26×10^{-09} |
| 662.33 | 750 | 3.37×10^{-09} |
| 662.33 | 1000 | 4.05×10^{-09} |
| 662.33 | 1250 | 5.47×10^{-09} |
| 662.33 | 1500 | 6.59×10^{-09} |
| 662.33 | 1750 | 7.75×10^{-09} |
| 662.33 | 2000 | 8.84×10^{-09} |
| 662.33 | 2250 | 9.94×10^{-09} |

Table 5.9: Permeability dependence upon temperature for the virgin state of the cork material.

| Inlet Pressure [Pa] | Temperature [K] | Permeability [m^2] |
|---------------------|-----------------|------------------------|
| 662.33 | 300 | 8.34×10^{-11} |
| 662.33 | 500 | 1.39×10^{-10} |
| 662.33 | 750 | 2.08×10^{-10} |
| 662.33 | 1000 | 2.75×10^{-10} |
| 662.33 | 1250 | 3.44×10^{-10} |
| 662.33 | 1500 | 4.12×10^{-10} |
| 662.33 | 1750 | 8.33×10^{-11} |
| 662.33 | 2000 | 5.51×10^{-10} |
| 662.33 | 2250 | 6.19×10^{-10} |
| 662.33 | 2500 | 6.88×10^{-10} |

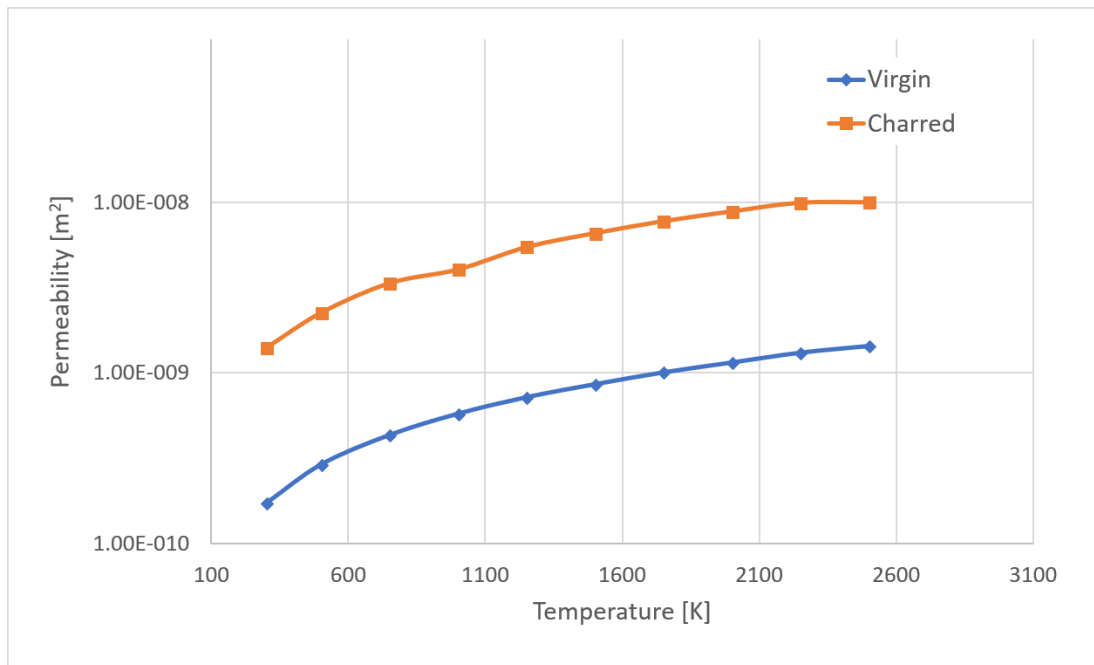


Figure 5.9: Permeability Temperature trend for the virgin and charred state of the carbon material.

Table 5.10: Permeability dependence upon temperature for the pyrolysed state of the cork material.

| Inlet Pressure [Pa] | Temperature [K] | Permeability [m²] |
|---------------------|-----------------|-----------------------|
| 662.33 | 300 | 1.26×10^{-9} |
| 662.33 | 500 | 2.06×10^{-9} |
| 662.33 | 750 | 3.04×10^{-9} |
| 662.33 | 1000 | 4.04×10^{-9} |
| 662.33 | 1250 | 5.03×10^{-9} |
| 662.33 | 1500 | 6.01×10^{-9} |
| 662.33 | 1750 | 7.00×10^{-9} |
| 662.33 | 2000 | 8.00×10^{-9} |
| 662.33 | 2250 | 8.99×10^{-9} |
| 662.33 | 2500 | 9.98×10^{-9} |

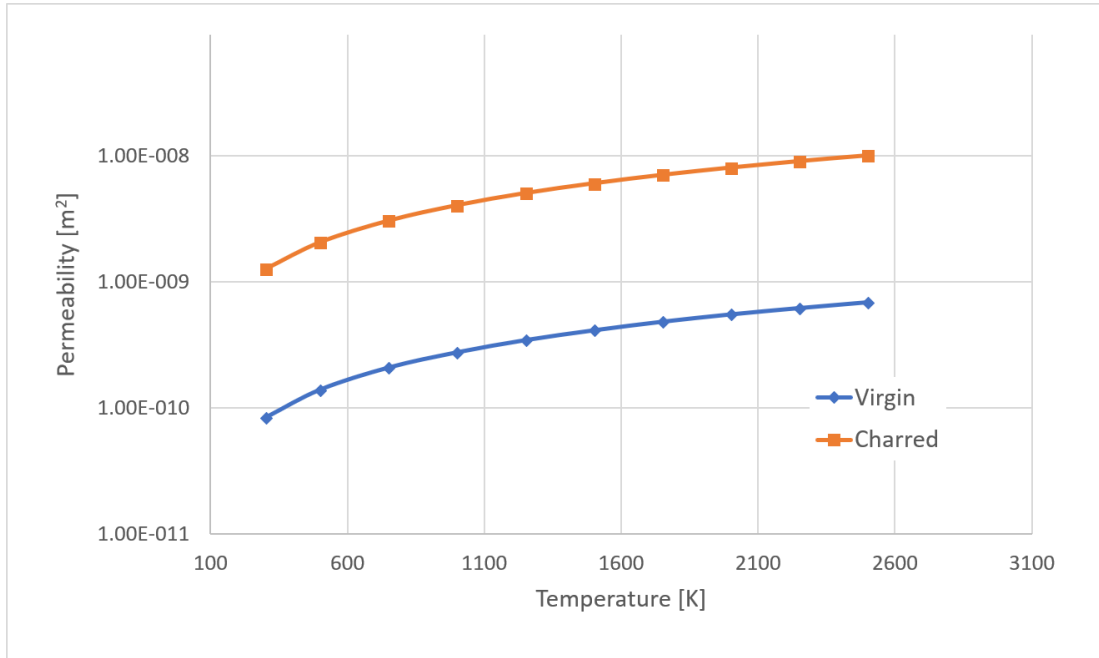


Figure 5.10: Permeability Temperature trend for the virgin and charred state of the cork material.

Table 5.11: Run time for the study of pressure dependency in the virgin carbon material.

| Time | CPU hours | Hours on 48 cores |
|---------|-----------|-------------------|
| Maximum | 15216 | 317 |
| Minimum | 2728 | 57 |
| Total | 66717 | 1390 |

material.

This dependency is significant and the data presented here is in a form that could be readily included in any simulation of the overall performance of the ablative materials in practical applications.

Since the increase of temperature increase the flux mean free path, no error analysis was performed on the temperature simulations.

5.2.3 Simulation time

The DSMC approach allows a very detailed representation of the internal gas flow through the pores of the ablative material to be simulated, however it requires significant and expensive computational resources to run. Some data regarding the simulation

Chapter 5. Permeability

Table 5.12: Run time for the study of pressure dependency in the pyrolysed carbon material study.

| Time | CPU hours | Hours on 48 cores |
|---------|-----------|-------------------|
| Maximum | 15661 | 326 |
| Minimum | 1803 | 38 |
| Total | 59228 | 1234 |

Table 5.13: Run time for the study of pressure dependency in the virgin cork material.

| Time | CPU hours | Hours on 48 cores |
|---------|-----------|-------------------|
| Maximum | 3262 | 68 |
| Minimum | 1293 | 27 |
| Total | 28303 | 590 |

Table 5.14: Run time for the study of pressure dependency in the pyrolysed cork material.

| Time | CPU hours | Hours on 48 cores |
|---------|-----------|-------------------|
| Maximum | 2583 | 54 |
| Minimum | 1268 | 26 |
| Total | 11881 | 248 |

Table 5.15: Run time for the study of temperature dependency in the virgin carbon material.

| Time | CPU hours | Hours on 48 cores |
|---------|-----------|-------------------|
| Maximum | 5948 | 124 |
| Minimum | 1368 | 29 |
| Total | 26856 | 559 |

Table 5.16: Run time for the study of temperature dependency in the pyrolysed carbon material.

| Time | CPU hours | Hours on 48 cores |
|---------|-----------|-------------------|
| Maximum | 4756 | 99 |
| Minimum | 626 | 13 |
| Total | 19162 | 399 |

Table 5.17: Run time for the study of temperature dependency in the virgin cork material.

| Time | CPU hours | Hours on 48 cores |
|---------|-----------|-------------------|
| Maximum | 7482 | 156 |
| Minimum | 996 | 21 |
| Total | 26635 | 555 |

Table 5.18: Run time for the study of temperature dependency in the pyrolysed cork material.

| Time | CPU hours | Hours on 48 cores |
|---------|-----------|-------------------|
| Maximum | 2899 | 60 |
| Minimum | 960 | 20 |
| Total | 9785 | 204 |

time required to run the various cases is presented in this section to give a better insight of the computational requirements of the methodology used. All results were obtained using the EPSRC funded ARCHIE-WeSt High Performance Computer (www.archie-west.ac.uk) which was established in the West of Scotland under EPSRC grant no. EP/K000586/1. The HPC has dual Intel Xeon X5650 2.66 GHz CPUs (6 cores each) and 48 GB RAM per node. The run times for the temperature and pressure dependency studies are contained from Table 5.11 to Table 5.18. In total the study consumed more than 5178 hours of core hours. This means that the equivalent of 216 days of computational time was involved in characterising of the material permeability.

5.3 Discussion

The aim of this work was to develop a technique that could be used a priori to characterise the internal gas flow within a given ablator material, and, in particular, to determine the permeability of the material and its dependence on the thermodynamic characteristics of the material and the gas flowing through it. An extension of the Direct Simulation Monte Carlo (DSMC) method that was capable of calculating the gas flow through the highly contorted and interconnected system of passages that are representative of the interior of many ablative materials, was able to achieve this aim. The results shown in this document provide such a characterisation for two representative ablative materials, one carbon fibre-based and the other a cork composite. The data produced can be readily implemented into any ablative simulation tool. Pressure and temperature dependence of the permeability should increase the predictive capability of these models and allow them to achieve a more precise characterization of the real material behaviour; especially if compared with the single-point characterisations that

have conventionally been used up to now.

5.4 Acknowledgements

This work was supported by the EU/FP7 ABLAMOD program, grant no. FP7-SPACE-2012-312987. The CT scans of the materials were performed by the Austrian Foundry Research Institute (GI) as part of the ABLAMOD program.

Chapter 6

Conclusions

The main aim of the study presented in this document was the improvement of ablative material simulation capabilities for a number of mission design phases and for new materials development. In order to achieve this goal, two different main activities were performed. The first activity was the creation of a low computationally demanding tool with the ability to simulate the three-dimensional coupled behaviour of ablative TPS and the external environment. The second activity was the investigation of the changes that pressure and temperature produce in a porous material permeability. The first activity was achieved through three different steps; the first step was the implementation of a one-dimensional ablative response code (ARC). The second step was the construction of the methodology employed to obtain three-dimensional results from ARC. The last step was the coupling of this methodology with two different aero-thermodynamic reduced order models. The second activity was achieved through DSMC simulations and produced look-up tables to be used by thermal response codes. Together, these activities can be used throughout the entire mission design of an ablative TPS.

The methodology created in the first activity is intended to be used in the preliminary phases of the missions design, when fast but reliable results are needed. This novel tool produces not just one-dimensional evaluations of particular places of interests on the spacecraft surface but, it is also able to generate three-dimensional evaluations of the TPS behaviour on the entire capsule geometries in minutes. The time required to complete these simulations is significantly lower than what could be expected from an

Chapter 6. Conclusions

equivalent coupled program using a CFD code. The run times depend on the number of panels of the spacecraft geometry and the entry duration; in the case of the Stardust simulation, coupled with HyFlow, the run time was about 20 minutes. Nowadays, conventional CFD analysis cannot generate results with the same speed and it would take longer to simulate just one time instance of the whole trajectory. Certainly, higher fidelity tools produce more accurate results, however, that level of accuracy is considered not to be required in the target design phases of the methodology herein presented. In any phase of the mission design, a trade off between the minimum running time and the maximum results accuracy must be performed. During the preliminary phases of most studies, fast running and less accurate tools are usually employed. This is because in those phases, a great number of simulations are required to select the right materials; therefore higher error for the temperature values or recession assessments are considered acceptable for the task to be performed. The coupled procedure presents lower than 15% absolute error, compared to commercial high fidelity codes, for those properties on the stagnation point area, which is the most demanding of the entire geometry. Depending on the study aims and goal, such error can be considered low enough thanks to the low computational requirement of the methodology.

On the other hand, the tables of permeability values generated in the second activity are intended to be used in the final phases of the mission design when the maximum precision is required and all phenomena must be taken into consideration. The permeability is considered pressure and temperature constant in most commercial programs in use. This would not be problematic if the changes introduced were small and therefore negligible; however, the investigations carried out during this study show that the variations can be of orders of magnitude which are definitely not negligible.

When possible, the proposed tools have been verified through the comparisons with more computationally demanding commercial codes which have shown that both ARC in its one-dimensional configuration and the coupled three-dimensional methodology produce results, which are comparable to the results generated by those commercial programs.

In particular, section 2.4 illustrates the verification performed on ARC and shows

Chapter 6. Conclusions

that this code produces calculations in very good agreement with commercial programs for temperatures, pyrolysis gas production and recession. External temperatures are particularly well calculated and the computation of internal temperatures shows a conservative behaviour. These are exactly the type of results that are of critical interest in the preliminary phases of a TPS design.

Chapter 4 establishes that the good agreement with commercial codes that characterizes the one-dimensional version of ARC is also present in the three-dimensional methodology. It shows that the methodology implemented, and in particular the decision to neglect the three-dimensional effects of thermal conduction inside the material, is reasonable and can generate results that are similar to empirical evidence in the phase of active heating during an atmospheric entry. The results presented show that, even if some of the physics is neglected, the outcomes are comparable to more precise tools. Moreover, larger errors are introduced by aero-thermodynamic models. This means that the three-dimensional methodology is able to produce even better results if coupled with more precise aero-thermodynamic models.

Chapter 5 demonstrates that the permeability of a porous material is pressure and temperature dependent and that considering this property as constant is unrealistic. It also shows that the new methodology can be used to produce valuable results even if applied outside its usual boundaries. The most important results of this particular activity are the tables containing the permeability values as a function of temperature and pressure that can be easily implemented in any ablative simulation tool which contains the momentum conservation equation.

Novel ideas and methods have been used in both main activities. The main novelty of the first activity is the use of a one-dimensional code to produce three-dimensional results. To the author's knowledge a similar approach has never been used for ablative material simulation tools before. The second novelty in this activity consist of using reduced order aero-thermodynamic models instead of a CFD tool. To the author's knowledge, these kind of models have never being used for ablative simulation coupling. Therefore, the aim of the study was achieved in a novel way, different from anything present in literature.

Chapter 6. Conclusions

The novelty of the second activity consists of the use of a new DSMC method outside of its usual limitations. The boundaries that describe good DSMC practice are introduced to assure the precision of the calculated results and should not be neglected without studying the consequences of this decision. For this reason, an error analysis was performed and it was concluded that the expected errors would not invalidate the results of the study. Moreover, even if the results for the most extreme simulations (elevated temperature or pressure values) do present a lower precision, they can still be used to confirm the variation trends since the calculated changes are elevated enough (orders of magnitude).

Both activities were essential to achieve the goal set for this study. Each one alone would not have been sufficient. Moreover, the outcomes of the two activities were thought and generated to be used together, to maximise the improvement to the entire design process. The three-dimensional methodology alone can only partially improve the ablative design and the same effect is given by the use of the look-up tables. It is only when used together, throughout the entire design process, from the selection of the TPS shape and material to the final definition of the last details, that the entire study fulfils its purpose.

It can be concluded that the initial aim has been satisfied with the generation of reliable and novel methods which can be used both in the next generation mission designs and in the development and modelling of new ablative materials able to meet these new missions requirements. In particular, the main contributions of this study are:

- the unequivocal proof that the permeability is far from being pressure or temperature constant.
- the thermal conduction of adjacent point on the capsule surface can be neglected during the simulation of the active heating phase of an atmospheric entry. This was proven to be right even for atmospheres characterized by lower density than Earth's one, like Mars'.

Both notions can be extremely helpful in improving the TPS design process, if properly

introduced in this process by those who produce the thermo-ablative analyses for entry missions.

6.1 Future work

The work presented in this document can certainly be expanded. In the author's opinion, this are the most important and useful additions to the study that can be done in the future:

- Further validation of the methodology through the comparison to real entries data and plasma chamber test. In particular, the use of plasma test data can really help to quantify the errors introduced in the methodology by neglecting the three dimensional effects of thermal conduction. Moreover, if used in combination with plasma test results, the three dimensional methodology can be an efficient tool used to better determine the material characteristics.
- Better three-dimensional verification of the methodology. It was very difficult to find in literature any data regarding the behaviour of the back shield during entries. A better verification and validation must, therefore, be carried out for the results generated for the back part of the geometries. Especially because the strength of this methodology is the ability to simulate the capsule in its entirety instead of just a portion of it.
- Coupling of the methodology with CFD tool. This activity would be used to better evaluate the influence of the assumption made to generate the three dimensional version of ARC, which is neglecting the adjacent points thermal conduction. Using CFD tool, will help quantify the error introduced in the methodology by this assumption.
- Validation of the permeability tables through the comparison with empirical test data. This data doesn't exist yet. However, since both the cork and the carbon material are being used for different missions, new funding cold be invested in the future for tests to better characterize them.

Chapter 6. Conclusions

- Implementation of the momentum equilibrium equation (Darcy's law) in ARC. Once this equation is implemented, it is possible to use the permeability tables directly in ARC and to evaluate the influence of the changing permeability on the overall ablator behaviour.

Bibliography

- [1] B. Laub, M. J. Wright, and E. Venkatapathy. Thermal protection system (tps) design and the relationship to atmospheric entry environments. In *6th International Planetary Probe Workshop. Atlanta, Georgia.* NASA Ames Research Center, 2008.
- [2] F. S. Milos, Y. K. Chen, T. H. Squire, and R. A. Brewer. Analysis of Galileo Probe Heatshield Ablation and Temperature Data. *Journal of Spacecraft and Rockets*, 36(3):298–306, May 1999.
- [3] F. S. Milos. Galileo Probe Heat Shield Ablation Experiment. *Journal of Spacecraft and Rockets*, 34(6):705–713, November 1997.
- [4] J. A. Cutts, J. Arnold, E. Venkatapathy, E. Kolawa, M. Munk, P. Wercinsky, and B. Laub. Thecnology for entry probes, 2004.
- [5] R. D. Braun and R. M. Manning. Mars Exploration Entry, Descent, and Landing Challenges. *Journal of Spacecraft and Rockets*, 44(2):310–323, March 2007.
- [6] W. H. Willcockson. Mars Pathfinder Heatshield Design and Flight Experience. *Journal of Spacecraft and Rockets*, 36(3):374–379, May 1999.
- [7] B. Laub, Y. K. Chen, and J. Dec. Development of a high fidelity thermal ablation response model for sla-561v. In *American Institute of Aeronautics and Astronautics*, June 2009.
- [8] M. J. Wright, C. Y. Tang, K. T. Edquist, B. R. Hollis, P. Krasa, and C. A. Campbell. A review of aerothermal modeling for mars entry missions. *48th AIAA*

Bibliography

- Aerospace Sciences Meeting Including the New Horizons Forum and Aerospace Exposition*, 2010.
- [9] R. A. S. Beck, D. M. Driver, M. J. Wright, H. H. Hwang, K. T. Edquist, and S. A. Sepka. Development of the Mars Science Laboratory Heatshield Thermal Protection System. *Journal of Spacecraft and Rockets*, 51(4):1139–1150, July 2014.
 - [10] H. K. Tran, C. Johnson, D. Rasky, F. Hui, M. T. Hsu, T. Chen, Y. K. Chen, D. Paragas, and L. Kobayashi. Phenolic Impregnated Carbon Ablators PICA as Thermal Protection System for Discovery Missions. *NASA TM-110440*, NASA, Washington, DC, 1997.
 - [11] K. Edquist, A. Dyakonov, M. Wright, and C. Tang. Aerothermodynamic design of the mars science laboratory heatshield. *41st AIAA Thermophysics Conference, Fluid Dynamics and Co-located Conferences*, 2009.
 - [12] J. L. Conley and K. H. Peterson. What are the Origins of Thermal Protection Systems? *NASA, Ames Research center*, 2011.
 - [13] D. M. Curry. Thermal protection systems manned spacecraft flight experience. *NASA Lyndon B. Johnson Space Center*, 1992.
 - [14] M. J. Wright, F. S. Milos, and P. Tran. Afterbody Aeroheating Flight Data for Planetary Probe Thermal Protection System Design. *Journal of Spacecraft and Rockets*, 43(5):929–943, September 2006.
 - [15] J. M. Bouilly, L. Dariol, and F. Leleu. Ablative thermal protections for atmospheric entry. an overview of past missions and needs for future programmes. In *Thermal Protection Systems and Hot Structures, 5th European Workshop*. ESTEC, Noordwijk, The Netherlands., 08/2006.
 - [16] M. Gottero, V. Perotto, and C. Alary. In-flight verification of the thermal control system of exomars edm. In *47th International Conference on Environmental Systems*, 2017.

Bibliography

- [17] A. Gulhan, T. Thiele, F. Siebe, and R. Kronen. Combined Instrumentation Package COMARS+ for the ExoMars Schiaparelli Lander. *Space Science Reviews*, 214(1), February 2018.
- [18] C. B. Moyer and M. R. Wool. Exomars 2016 schiaparelli anomaly inquiry. Technical report, ESA, May 2017.
- [19] O. Drescher, M. Hrschgen-Eggers, G. Pinaud, and M. Podeur. Cork based thermal protection system for sounding rocket application, development and flight testing.,, 2017.
- [20] K. C. Clausen, H. Hassan, M. Verdant, P. Couzin, G. Huttin, M. Brisson, C. Sol-lazzo, and J. P. Lebreton. The Huygens probe system design. In *The Cassini-Huygens Mission*, pages 155–189. Springer, 2003.
- [21] B. R. Hollis, S. A. Striepe, M. J. Wright, D. Bose, K. Sutton, N. Takashima, and M. Schoenenberger. Prediction of the aerothermodynamic environment of the Huygens probe. *AIAA Paper*, 4816, 2005.
- [22] E. Venkatapathy, C. E. Szalai, B. Laub, H. H. Hwang, J. L. Conley, and J. Arnold. Thermal protection system technologies for enabling future sample return missions. *Planetary Science Decadal Survey, National Research Council, Washington, DC*, 2009.
- [23] B. Laub and E. Venkatapathy. Thermal protection system technology and facility needs for demanding future planetary missions. In *International Workshop Planetary Probe Atmospheric Entry and Descent Trajectory Analysis and Science.*, ESA SP-544, Noordwijk, Netherlands: ESA Publications Division, ISBN, 2004.
- [24] International Workshop Planetary Probe Atmospheric Entry and Descent Trajectory Analysis and Science, 6-9 October 2003, Lisbon, Portugal. *Summary of the Boulder Entry Probe Workshop, International Workshop Planetary Probe Atmospheric Entry and Descent Trajectory Analysis and Science, 6-9 October 2003, Lisbon, Portugal.* ESA Publications, 2003.

Bibliography

- [25] R. M. Kendall, E. P. Bartlett, R. A. Rindal, and C. B. Moyer. An analysis of the coupled chemically reacting boundary layer and charring ablator: Part I. Technical report, NASA CR, 1968.
- [26] J. Lachaud, T. E. Magin, I. Cozmuta, and N. N. Mansour. A short review of ablative-material response models and simulation tools. In *7th Aerothermodynamics Symposium, European Space Agency, Brugge, Belgium*, 2011.
- [27] R. J. Schoner. User's manual aerotherm charring material thermal response and ablation computer program. Version 3. Technical report, Air Force Rocket Propulsion Laboratory Director of Laboratories, 1970.
- [28] Y. K. Chen and F. S. Milos. Ablation and Thermal Response Program for Spacecraft Heatshield Analysis. *Journal of Spacecraft and Rockets*, 36(3):475–483, May 1999.
- [29] F. K. Milos, Y. K. Chen, and T. H. Squire. Updated Ablation and Thermal Response Program for Spacecraft Heatshiel Analysis. *17th Thermal and Fluids Analysis Workshop, University of Maryland*, 2006.
- [30] Y. K. Chen, W. D. Henline, D. A. Stewart, and G. V. Candler. Navier-Stokes solutions with surface catalysis for Martian atmospheric entry. *Journal of Spacecraft and Rockets*, 30(1):32–42, January 1993.
- [31] R. W. Walters, P. Cinnella, D. C. Slack, and D. Halt. Characteristic-based algorithms for flows in thermochemical nonequilibrium. *AIAA Journal*, 30(5):1304–1313, May 1992.
- [32] F. S. Milos, Y. K. Chen, W. M. Congdon, and J. M. Thornton. Mars Pathfinder Entry Temperature Data, Aerothermal Heating, and Heatshield Material Response. *Journal of Spacecraft and Rockets*, 36(3):380–391, May 1999.
- [33] Y. K. Chen, F. Milos, and T. Gokcen. Validation of a three-dimensional ablation and thermal response simulation code. In *10th AIAA/ASME Joint Thermophysics and Heat Transfer Conference*, page 4645, 2010.

Bibliography

- [34] Y. K. Chen and F. S. Milos. Two-Dimensional Implicit Thermal Response and Ablation Program for Charring Materials. *Journal of Spacecraft and Rockets*, 38(4):473–481, July 2001.
- [35] N. N. Mansour, J. R. Lachaud, T. E. Magin, J. Muelenaere, and Y. K. Chen. High-Fidelity Charring Ablator Thermal Response Model. *42nd AIAA Thermophysics Conference, Honolulu, Hawai*, 2011.
- [36] J. Lachaud, T. van Eekelen, J. B. Scoggins, T. E. Magin, and N. N. Mansour. Detailed chemical equilibrium model for porous ablative materials. *International Journal of Heat and Mass Transfer*, 90:1034–1045, November 2015.
- [37] J. Lachaud and N. N. Mansour. Porous Material Analysis Toolbox Based on Open-FOAM and Applications. *Journal of Thermophysics and Heat Transfer*, 28(2):191–202, April 2014.
- [38] J. Scoggins and T. E. Magin. Development of Mutation++: Multicomponent Thermodynamic and Transport Properties for Ionized Plasmas written in C++. *11th AIAA/ASME Joint Thermophysics and Heat Transfer Conference*, June 2014.
- [39] A. Martin and I. D. Boyd. Non-Darcian Behavior of Pyrolysis Gas in a Thermal Protection System. *Journal of Thermophysics and Heat Transfer*, 24(1):60–68, January 2010.
- [40] A. Martin and I. Boyd. Implicit implementation of material response and moving meshes for hypersonic re-entry ablation. In *47th AIAA Aerospace Sciences Meeting including The New Horizons Forum and Aerospace Exposition*, page 670, 2009.
- [41] A. Martin and I. D. Boyd. Strongly Coupled Computation of Material Response and Nonequilibrium Flow for Hypersonic Ablation. *Journal of Spacecraft and Rockets*, 52(1):89–104, January 2015.
- [42] L. Paglia, J. Tirill, F. Marra, C. Bartuli, A. Simone, T. Valente, and G. Pulci. Carbon-phenolic ablative materials for re-entry space vehicles: plasma wind tunnel test and finite element modeling. *Materials & Design*, 90:1170 – 1180, 2016.

Bibliography

- [43] G. Pinaud. Thermo-chemical and mechanical coupled analysis of swelling charring and ablative materials for re-entry application. In *ASTRIUM SPACE TRANSPORTATION*, 2012.
- [44] J. de Muelenaere, J. Lachaud, N. N. Mansour, and T. E. Magin. Stagnation line approximation for ablation thermochemistry. *42nd AIAA Thermophysics Conference, Honolulu, Hawai*, 2011.
- [45] B. J. McBride and S. Gordon. Computer program for calculation of complex chemical equilibrium compositions and applications. *National Aeronautics and Space Administration*, June 1996.
- [46] C. B. Moyer and M. R. Wool. Aerotherm Charring Material Thermal Response and Ablation Program, Version 3. Volume 1. Program Description and Sample Problems. Technical report, AEROTHERM CORP MOUNTAIN VIEW CA, 1970.
- [47] Eric Jones, Travis Oliphant, Pearu Peterson, et al. SciPy: Open source scientific tools for Python, 2001.
- [48] P. N. Brown, G. D. Byrne, and A. C. Hindmarsh. Vode, a variable-coefficient ode solver. *SIAM Journal on Scientific and Statistical Computing*, 1988.
- [49] L. Torre, J. Kenny, and A. Maffezzoli. *Degradation behaviour of a composite material for thermal protection systems Part IExperimental characterization*, volume 33. , January 1998.
- [50] J. Lachaud, A. Martin, I. Cozmuta, and B. Laub. Ablation test-case series 2. In *5th AFOSR/SNL/NASA Ablation Workshop* -, 2011.
- [51] T. van Eekelen and J. M. Bouilly. Inter-code calibration exercise. Technical report, ASTRIUM, 2012.
- [52] T. van Eekelen, J. M. Bouilly, S. Hudrisier, J. M. Dupillier, and Y. Aspa. Design and numerical modelling of charring material ablators for re-entry applications. In *Sixth European Workshop on Thermal Protection Systems and Hot Structures, University Stuttgart, Germany*. European Space Agency, 21-25 November, 2009.

Bibliography

- [53] T. Risch and C. Kostyk. Test case baseline results. Technical report, NASA Dryden Flight Research Center, 2012.
- [54] F. Chen, Y. K. Milos and D. J. Rasky. Fully implicit ablation and thermal response program for spacecraft heatshield analysis. In 36th AIAA Aerospace Sciences Meeting and NV; United States Exhibit; 12-15 Jan. 1998; Reno, editors, *American Inst. of Aeronautics and Astronautics; United States*. NASA Ames Research Center; Moffett Field, CA United States, 1998.
- [55] D. Olynick, Y. K. Chen, and Michael E. Tauber. Aerothermodynamics of the Stardust Sample Return Capsule. *Journal of Spacecraft and Rockets*, 36(3):442–462, May 1999.
- [56] Romain Wuilbercq. *Multi-Disciplinary Modelling of Future Space-Access Vehicles*. PhD thesis, University of Strathclyde, 2015.
- [57] W. L. Hankey. Re-entry aerodynamics. *American Instituteof Aeronautics and Astronautics,,* Washington, DC, 1988.
- [58] H. H. Hamilton and others. Approximate Method of Calculating Heating Rates at General Three-Dimensional Stagnation Points During Atmospheric Entry. *NASA Technical Memorandum*, 1982.
- [59] P. Mehta, E. Minisci, M. Vasile, Andrew C. Walker, and M. Brown. An open source hypersonic aerodynamic and aerothermodynamic modelling tool. In *8th European Symposium on Aerothermodynamics for Space Vehicles*, 2015.
- [60] P. M. Mehta, A. Walker, M. Brown, E. Minisci, and M. L. Vasile. Sensitivity Analysis towards Probabilistic Re-Entry Modeling of Spacecraft and Space Debris. In *American Institute of Aeronautics and Astronautics*, June 2015.
- [61] A. Falchi, E. Minisci, M. Vasile, D. Rastelli, and N. Bellini. DSMC-based correction factor for low-fidelity hypersonic aerodynamics of re-entering objects and space debris. In *7th European Conference for Aeronautics and Space Sciences*, pages 1–15, 2017.

Bibliography

- [62] A. Falchi, E. Minisci, M. Vasile, and M. Kubicek. Aero-thermal re-entry sensitivity analysis using DSMC and a high dimensional model representation-based approach. In *7th European Conference on Space Debris*, 2017.
- [63] R. Cassineli Palharini. *Atmospheric reentry modelling using an open source DSMC code*. PhD thesis, University of Strathclyde, 2014.
- [64] P. Tran, J. C. Paulat, and P. Boukhobza. Re-entry flight experiments lessons learned-the atmospheric reentry demonstrator ARD. Technical report, DTIC Document, 2007.
- [65] NOAA NASA and USAF. U.S. standard atmosphere. Technical report, U.S. Government Printing Office, 1976.
- [66] S. D. Williams and D. M. Curry. Thermal protection materials: thermophysical property data. *Thermal protection materials*, 1992.
- [67] C. Pinaud and A. Guelhan. Ablamod, advanced ablation characterization and modelling european project description. *6th Ablation Workshop, Urbana Champaign, IL*, 2014.
- [68] C. White, T. J. Scanlon, and R. E. Brown. Permeability of ablative materials under rarefied gas conditions. *Journal of Spacecraft and Rockets*, Vol. 53, No. 1, pages 134–142, 2016.
- [69] G. Bird. *Molecular gas dynamics and the direct simulation of gas flows*. Clarendon, 1994.
- [70] G. Bird. Monte carlo simulation of gas flows. *Annual Review of Fluid Mechanics*, pages 10, 11–31, 1978.
- [71] T. J. Scanlon, E. Roohi, C. White, M. Darbandi, and J. M. Reese. An open source, parallel dsmc code for rarefied gas flows in arbitrary geometries. *Computers and Fluids*, 39 (10), pages 2078–2089, 2010.